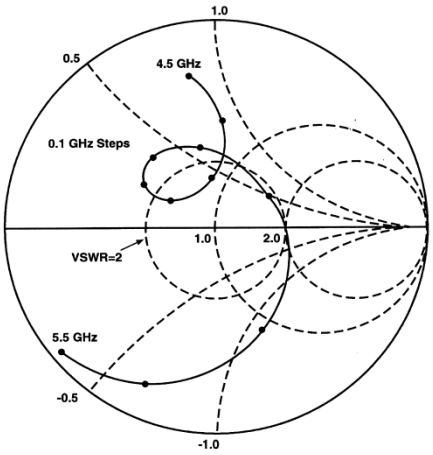

Applied Computational Electromagnetics Society Journal

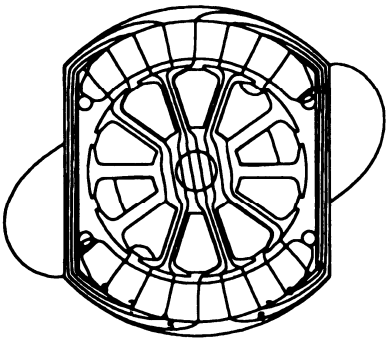

Editor-in-Chief
Atef Z. Elsherbeni

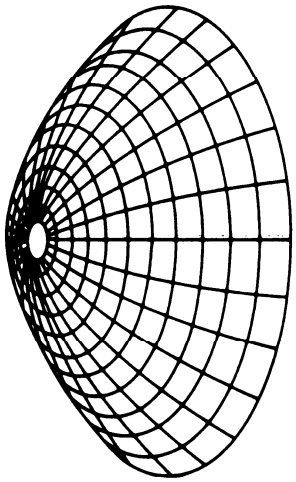

July 2010
Vol. 25 No. 7
ISSN 1054-4887

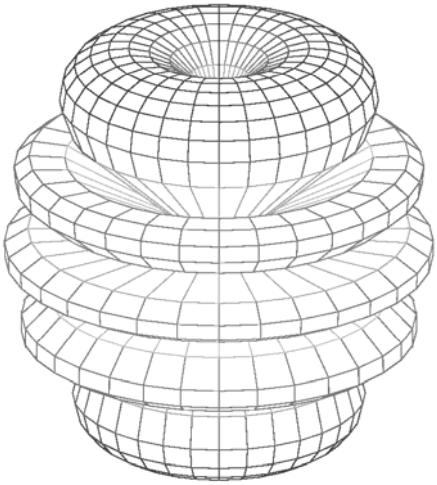

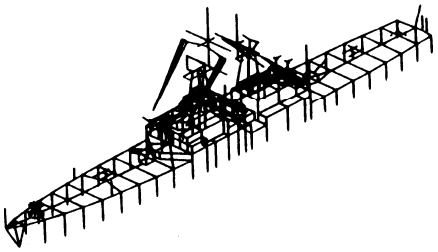

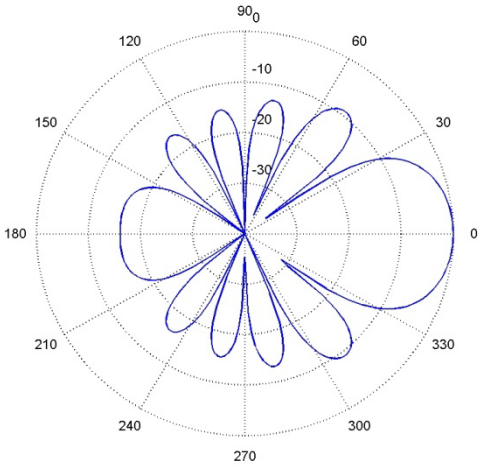

GENERAL PURPOSE AND SCOPE: The Applied Computational Electromagnetics Society ***(ACES)*** Journal hereinafter known as the ***ACES Journal*** is devoted to the exchange of information in computational electromagnetics, to the advancement of the state-of-the art, and the promotion of related technical activities. A primary objective of the information exchange is the elimination of the need to "re-invent the wheel" to solve a previously-solved computational problem in electrical engineering, physics, or related fields of study. The technical activities promoted by this publication include code validation, performance analysis, and input/output standardization; code or technique optimization and error minimization; innovations in solution technique or in data input/output; identification of new applications for electromagnetics modeling codes and techniques; integration of computational electromagnetics techniques with new computer architectures; and correlation of computational parameters with physical mechanisms.

SUBMISSIONS: The ***ACES Journal*** welcomes original, previously unpublished papers, relating to applied computational electromagnetics. Typical papers will represent the computational electromagnetics aspects of research in electrical engineering, physics, or related disciplines. However, papers which represent research in applied computational electromagnetics itself are equally acceptable.

Manuscripts are to be submitted through the upload system of ***ACES*** web site http://aces.ee.olemiss.edu See "Information for Authors" on inside of back cover and at ***ACES*** web site. For additional information contact the Editor-in-Chief:

Dr. Atef Elsherbeni
Department of Electrical Engineering
The University of Mississippi
University, MS 386377 USA
Phone: 662-915-5382 Fax: 662-915-7231
Email: atef@olemiss.edu

SUBSCRIPTIONS: All members of the Applied Computational Electromagnetics Society who have paid their subscription fees are entitled to receive the ***ACES Journal*** with a minimum of three issues per calendar year and are entitled to download any published journal article available at http://aces.ee.olemiss.edu.

Back issues, when available, are $15 each. Subscriptions to ***ACES*** is through the web site. Orders for back issues of the ***ACES Journal*** and changes of addresses should be sent directly to ***ACES***:

Dr. Allen W. Glisson
302 Anderson Hall
Dept. of Electrical Engineering
Fax: 662-915-7231
Email: aglisson@olemiss.edu

Allow four week's advance notice for change of address. Claims for missing issues will not be honored because of insufficient notice or address change or loss in mail unless the Executive Officer is notified within 60 days for USA and Canadian subscribers or 90 days for subscribers in other countries, from the last day of the month of publication. For information regarding reprints of individual papers or other materials, see "Information for Authors".

LIABILITY. Neither ***ACES***, nor the ***ACES Journal*** editors, are responsible for any consequence of misinformation or claims, express or implied, in any published material in an ***ACES Journal*** issue. This also applies to advertising, for which only camera-ready copies are accepted. Authors are responsible for information contained in their papers. If any material submitted for publication includes material which has already been published elsewhere, it is the author's responsibility to obtain written permission to reproduce such material.

APPLIED COMPUTATIONAL ELECTROMAGNETICS SOCIETY JOURNAL

Editor-in-Chief
Atef Z. Elsherbeni

July 2010
Vol. 25 No. 7
ISSN 1054-4887

The ACES Journal is abstracted in INSPEC, in Engineering Index, DTIC, Science Citation Index Expanded, the Research Alert, and to Current Contents/Engineering, Computing & Technology.

The first, fourth, and sixth illustrations on the front cover have been obtained from the Department of Electrical Engineering at the University of Mississippi.

The third and fifth illustrations on the front cover have been obtained from Lawrence Livermore National Laboratory.

The second illustration on the front cover has been obtained from FLUX2D software, CEDRAT S.S. France, MAGSOFT Corporation, New York.

THE APPLIED COMPUTATIONAL ELECTROMAGNETICS SOCIETY

JOURNAL

Vol. 25 No. 7 July 2010

TABLE OF CONTENTS

Improvement of Compactness of Lowpass/Bandpass Filter Using a New Electromagnetic Coupled Crescent Defected Ground Structure Resonators

Mohamed Al Sharkawy [1], Ahmed Boutejdar [2], Fatma Alhefnawi [3], Omar Luxor [1]

[1] Department of Electronics and Communication Engineering,
Arab Academy for Science, Technology & Maritime Transport, Alexandria, Egypt
mohamed_sharko1@hotmail.com

[2] Chair of Microwave and Communication Engineering University of Magdeburg
Universitätsplatz 02 39106 Magdeburg, Germany

[3] Microwave Engineering Department,
Electronic Research Institute, Cairo, Egypt

Abstract- This paper introduces a new compact defected ground structure (DGS) low pass filter (LPF) using a crescent shape structure etched in the ground plane. The filter response has improved dramatically by employing coupling of two DGS structures. Furthermore, the transformation to bandpass filter (BPF) is also investigated. The proposed configuration improved the lowpass response by widening the rejection band while significantly reducing the size. The behaviour of the filter has been investigated using HFSS as well as lumped element equivalent circuit model simulations using parallel L-C resonator. The proposed filter has been optimized.

Index Terms- Crescent, defected ground structure (DGS), low pass filter (LPF), band pass filter (BPF), frequency response.

I. INTRODUCTION

Defected ground structure technique is now applied in the design of microstrip filters. This helps to improve the filter performance and causes a size reduction, which is considered a major benefit. This technique is currently employed to meet the increasing demand for compact structure high performance [1] filters. Accordingly, numerous research has been done in order to achieve such goals. Lowpass and bandpass filters are enhanced by the use of such techniques [2-4].

The slots introduced at the backed ground plane layer (i.e, DGS) mainly improve the transition sharpness and widens the rejection band. This is due to the fact that the waves penetrating the structure are disturbed, causing equalization in the model phase velocity with respect to one another. This can also help in developing a more compact structure without the need to implement higher order filters with the same performance. In this paper, a new design for an LPF is investigated. The filter has a cutoff frequency of 1.9 GHz.

The filter performance has been improved by introducing two coupled elements as a defected structure in the ground plane. Furthermore, we have studied the effect of changing several parameters on the filter performance such as the coupling distance and the DGS area. Moreover, the implementation of a simple technique to transform the LPF into BPF is presented.

II. PROPOSED DGS STRUCTURE

The new proposed DGS structure, which is etched on the ground plane and shown in Fig. 1, has overall dimensions smaller than the predecessor H-DGS [5]. The crescent shape has the structure of a semi circle connected to a slot with a width g = 0.6mm, r = 5mm, t = 1mm and L=1.96mm. An RO4003 dielectric substrate of relative permittivity equals to 3.38 and thickness 0.813mm is used. The microstrip line on the upper

layer in Fig. 2 has a width of 1.9mm which guarantees a 50 Ω matching impedance.

The presence of the DGS in the ground plane introduces an additional equivalent inductance, which in turn increases the characteristic impedance of the 50 Ω line on the top layer. This leads to a broader width of the 50 Ω line relative to that of the standard microstrip line [7-10].

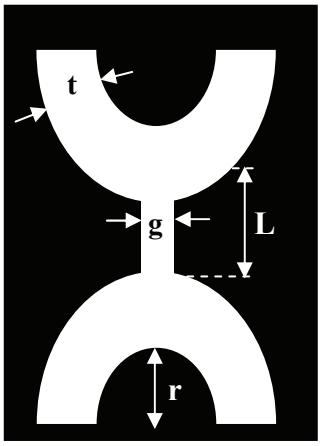

Fig. 1. Proposed single crescent DGS element.

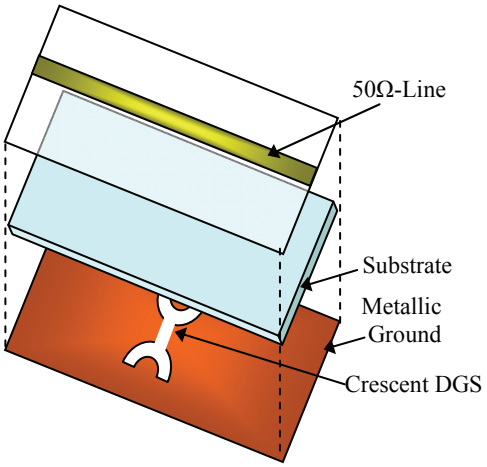

Fig. 2. 3-D view of the DGS resonator.

An equivalent circuit model for the crescent DGS element is shown in Fig. 3, which consists of simple L-C circuit [11,12]. The single crescent DGS LPF has been simulated using HFSS. The computed results were compared to that generated using the L-C circuit model. Good agreement between the equivalent circuit results and that of the simulated crescent element is shown in Fig. 4. As for the lumped elements used in the equivalent circuit, the capacitance (picofarads) and the inductance (nanohenrys) values are computed as using:

$$C_p = \frac{5 f_c}{\pi\left(f_0^2 - f_c^2\right)}\ pF \ and\ L_p = \frac{250}{C_p\left(\pi f_0\right)^2}\ nH \quad (1)$$

where f_c, is the cutoff frequency of the band reject response of the DGS at 3 dB and f_0, is the pole frequency [12].

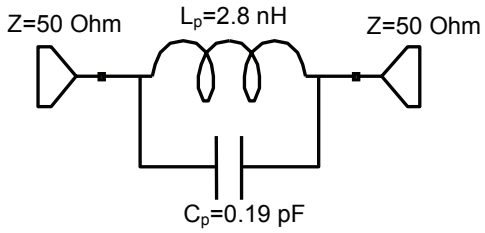

Fig. 3. Equivalent circuit of single DGS element.

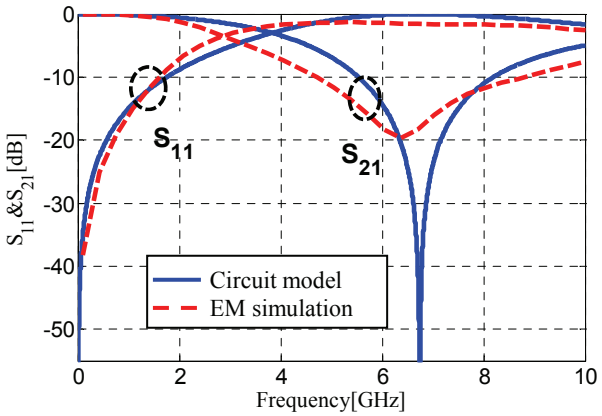

Fig. 4. Comparison between the S-parameters of the simulated crescent element and its equivalent circuit model.

III. COUPLED CRESCENT DGS FILTER

This section investigates the effect of etching two crescent DGS structures on the ground plane of the filter as shown in Fig. 5. The equivalent circuit model for the configuration of Fig. 5 is shown in Fig. 6. The proposed DGS shape has smooth edges and consequently less losses, which enhances its performance especially in the microwave range of frequencies where the filter is operating.

Moreover, the filter size is reduced dramatically, achieving a size saving of about 30%. This leads to a total filter size of $0.45\lambda_g \times 0.27\lambda_g$ having $\lambda_g = 58.3$ mm. The crescent LPF is

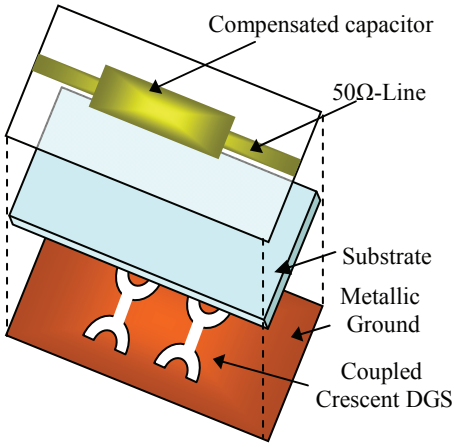

Fig. 5. 3-D view of coupled crescent DGS LPF.

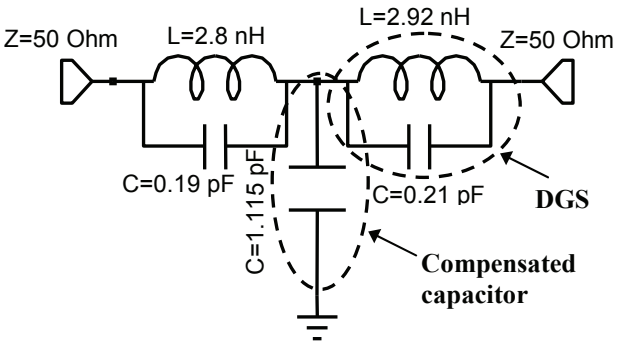

Fig. 6. Equivalent circuit of single DGS LPF.

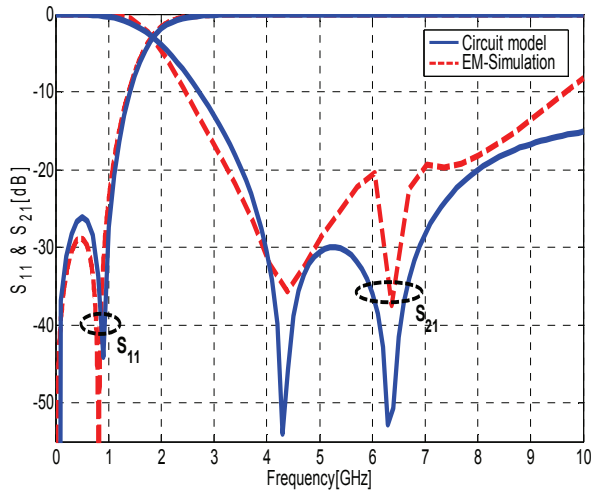

Fig. 7. Comparison between EM-simulation and circuit simulation results of the proposed filter structure.

simulated using microwave office. Figure 7 shows a comparison between the equivalent circuit model simulation and the microwave office simulation. The results show good agreement. The coupled crescent DGS filter shows a rejection band of about 6 GHz for an attenuation level less than 15dB providing an increase in the rejection band of about 50 % when compared to the H-DGS LPF [5].

A. Effect of Changing Coupling Distance on Filter Performance and Size at Crescent Radius of 5.0 mm

The coupling distance has a direct influence on the rejection band and also the filter size as shown in Table 1. Accordingly, there must be a trade off between performance and size to choose which suits best the application.

Table 1. Coupling distance versus rejection band and filter size.

Coupling distance(mm)	Rejection band < 20dB(GHz)		Filter size (mm^2)
	Top Layer		
	50 Ohm line	Comp. capacitor	
3	3.6-5.8	3.2-5.4	23 x 16
4	3.6-5.9	3.25-5.7	25 x 16
5	3.6-8.1	3.2-7	26 x 16
6	3.6-8.1	3.2-7	27 x 16
7	3.8-8.1	3.2-7	28 x 16

Coupling distance(mm)	Sharpness Factor(fo/fc)		Filter size (mm^2)
	Top Layer		
	50 Ohm Line	Comp. capacitor	
3	1.79	2.04	23 x 16
4	1.82	2.33	25 x 16
5	2	2.27	26 x 16
6	2.12	2.44	27 x 16
7	2.12	2.56	28 x 16

B. Effect of Changing Crescent Area at 5mm Coupling Distance

The crescent radius controls the inductance of its equivalent lumped circuit element model. Thus, increasing the radius value leads to an increase in the inductance value, which in turn decreases the cutoff frequency. This relation is clearly shown in Table 2.

A further investigation is conducted to study the effect of increasing the number of crescent elements in the DGS. Three coupled crescent elements are etched in the ground plane. The filter response in the presence of the 3 coupling crescent

Table 2. Crescent radius versus rejection band and cutoff frequency.

Crescent radius(mm)	Rejection band < 20dB(GHz)		f_c (GHz)	
	Top Layer		Top Layer	
	50 Ohm Line	Comp. capacitor	50 Ohm line	Comp. capacitor
3	9-14	8.6-11.4	4.1	2.8
4	5.4-7	4.7-7.6	3.19	2.44
5	3.6-8.1	3.2-7.7	2.4	1.9
6	3.8-8.2	3.2-7.7	2.25	1.75
Crescent radius(mm)	**Sharpness Factor(fo/fc)**		**f_c (GHz)**	
	Top Layer		Top Layer	
	50 Ohm Line	Comp. capacitor	50 Ohm line	Comp. capacitor
3	2.44	3.57	4.1	2.8
4	2.5	2.78	3.19	2.44
5	2	2.27	2.4	1.9
6	2.08	2.5	2.25	1.75

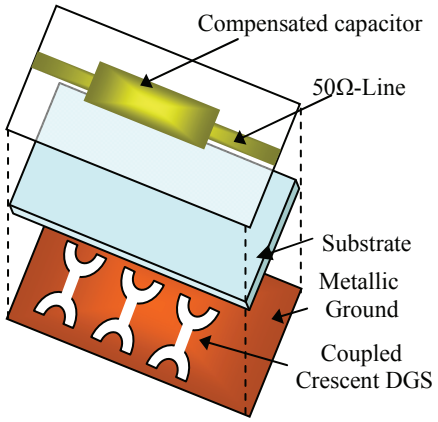

Fig. 8. 3-D view of coupled 3 crescents DGS LPF.

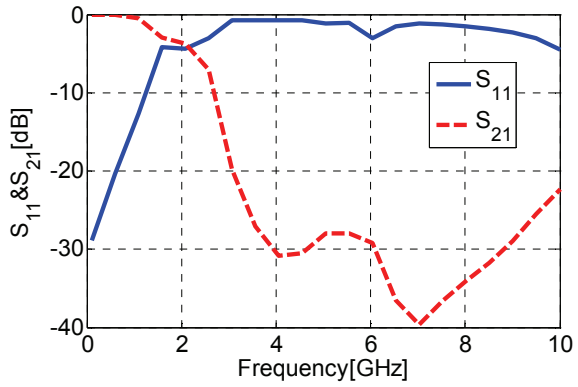

Fig. 9. Simulated S-parameters for the coupled 3 crescents DGS LPF.

elements is shown in Fig. 8. The relevant EM simulation is shown in Fig. 9. It can be noticed that the rejection band has increased dramatically due to the extended coupling. However, undesired effects have appeared in the pass band region. The equivalent filter size for the 3 crescent DGS LPF has increased to 41 × 16 mm^2.

IV. DISTRIBUTION OF ELECTRIC FIELD AT 4.4 GHz AND 1.0 GHz

The objective of this study is to prove the dependence of the equivalent circuit elements (capacitance and inductance) on the surface current distribution. This can be shown in Figs. 10, 11, and 12.

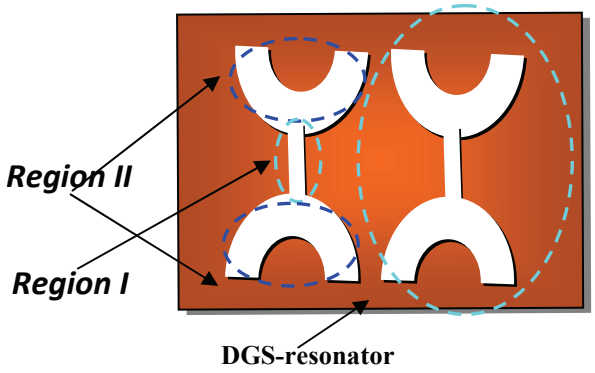

Fig. 10. Two-dimensional view of the proposed LPF.

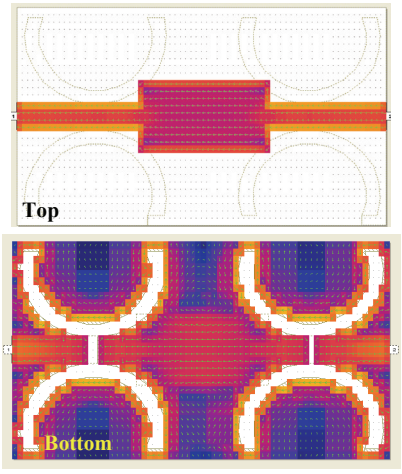

Fig. 11. Electric field distribution at f_0 = 1 GHz.

The structure is divided into two regions: region I, where the electric field is highly concentrated in the gap. Hence any change in the dimensions of the gap affects the effective capacitance of the

structure. In region II, the electric field nearly vanishes [1-2]. This means that the length of the arcs does not affect the effective capacitance of the filter structure. The current is distributed throughout the whole structure. Therefore any change in the length of the arcs strongly affects the magnetic field distribution and hence the surface current, which in turn leads to a change in the effective inductance of the structure. Based on the previous illustration, region I corresponds to a capacitance, while region II corresponds to an inductance. Thus, the full structure corresponds to a parallel LC-resonator, which supports the circuit model shown in Fig. 6.

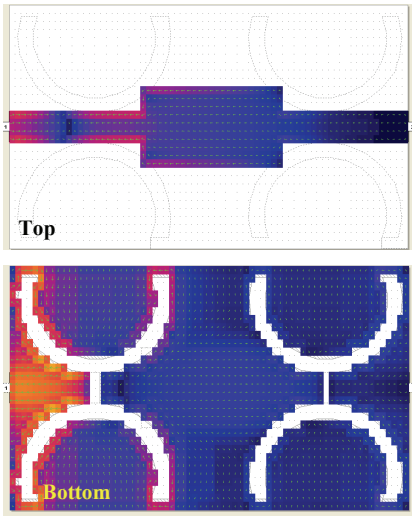

Fig. 12. Electric field distribution at $f_0 = 4.4$GHz.

V. THE TRANSFORMATION OF LPF TO BPF USING J-INVERTER-METHOD

It is well known that the transmission characteristics of microstrip low-pass filters have a periodic behavior. The periodicity is approximately four times the cutoff frequency f_c. This property of microstrip lowpass filters can be used to carry out a new and simple transformation from LPF to BPF [13]. Figure 13 shows the 3-D schematic view of the new compact BPF. The proposed BPF has a discontinuity in the feed microstrip line J-inverter as compared to continuous feed line of the LPF. In this case, the transmission characteristics is inverted, causing the structure to act as a bandpass filter with passband between f_c and 3 f_c and a stop-bands in DC- and [3 f_c - 4 f_c] intervals. The frequency response of the bandpass filter is shown in Fig. 14.

Figure 13 shows the microstrip BPF using end-coupled λ/2-microstrip resonators. Equivalent circuit of the gap-microstrip is shown in Fig. 13. The effect of the gap is equivalent to π-shunt (C_{IO}) and series (C_k) capacitances. The remaining capacitances and inductances are obtained from EM simulations of the single DGS element and the optimization method. The capacitances CIO and C_k are determined by:

$$for \quad 2.5 \le \varepsilon_r = 3.38 \le 15.0$$

$$\frac{C_{even}}{w} = \left(\frac{\varepsilon_r}{9.6}\right)^{0.9} \left(\frac{s}{w}\right)^{m_e} e^{k_e}\left(\frac{pF}{m}\right) \tag{2}$$

$$\frac{C_{odd}}{w} = \left(\frac{\varepsilon_r}{9.6}\right)^{0.8} \left(\frac{s}{w}\right)^{m_o} e^{k_o}\left(\frac{pF}{m}\right) \tag{3}$$

$$for \quad 0.1 \le \frac{s}{w} = 0.6 \le 1.0 \;\&\; \left(\frac{w}{h}\right) = \eta$$

$$\Rightarrow \mathrm{m_0} = \left(\frac{w}{h}\right)\left[0.92\log\eta - 0.38\right] \tag{4}$$

$$\Rightarrow \mathrm{k_0} = \left[4.26 - 1.45\log\eta\right] \tag{5}$$

$$\Rightarrow \mathrm{m_e} = \left[\left(\frac{1.565}{\eta^{0.16}}\right) - 1.0\right]$$

$$\& \; \mathrm{k_e} = \left[1.97 - \left(\frac{0.03}{\eta^{1}}\right)\right] \tag{6}$$

$$\Rightarrow \mathrm{C_{IO}} = \left(\frac{C_{even}}{2.0}\right) \;\&\; \mathrm{C_k} = \left(\frac{C_{odd}}{2.0} - \frac{C_{even}}{2.0}\right) \tag{7}$$

In order to improve the BPF behaviour, it is necessary to find the optimal distance between both DGS resonators. Through which the electromagnetic energy can be optimally utilized. Accordingly, the losses will be minimised in the pass-band, which leads to a better response. The coupling method and the coupling matrix will be used in order to calculate the gap distance (p = 0.2 λ_g),

$$\lambda_g = \left(2\pi \frac{c_0}{\omega_c \sqrt{\varepsilon_r}}\right) \qquad (c_0 \approx 3.10^8 ms^{-1}). \tag{8}$$

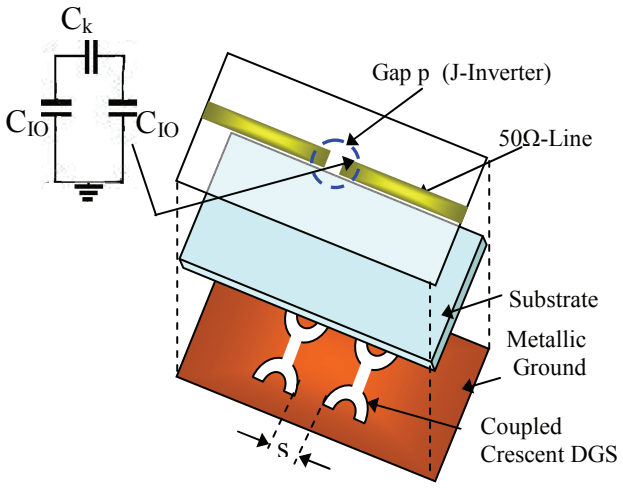

Fig. 13. Three-dimensional view of the proposed band-pass filter.

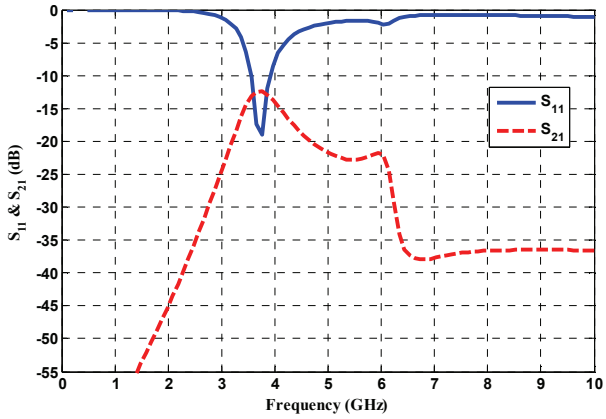

Fig. 14. Simulated S-parameters for the proposed crescent -DGS BPF.

VI. CONCLUSION

A new crescent DGS design has been implemented and its equivalent circuit was developed. The crescent DGS, when employed using coupling method, achieved very good results in terms of a rejection band of 6 GHz at an attenuation level less than 15 GHz. Furthermore, a size reduction of about 30 % was achieved relative to a predecessor design. Parametric studies were conducted to investigate the effect of coupling distance between crescent DGS elements and the crescent DGS area size on the filter performance. Moreover, an electric field analysis was performed on the proposed LPF. Transformation of the LPF to BPF was studied and employed using the technique of J-inverter.

REFERENCES

[1] A. Boutejdar, A. Batmanov, A. Omar, and E. P. Burte, "A miniature 3.1 GHz microstrip bandpass filter with suppression of spurious harmonics using multilayer technique and defected ground structure open-loop ring," *Ultra-wideband, short-pulse electromagnetics 9,*. Springer, pp. 191-200, 2010.

[2] A. Boutejdar, A. Batmanov, E. Burte, and A. Omar, "Design of a new bandpass filter with sharp transition band using multilayer-technique and U-defected ground structure (DGS)," *IET Microwaves, Antennas and Propagations*, vol. 4, no. 3, pp. 377-384, 2010.

[3] A. Boutejdar, A. Sherbini, and A. Omar, "A novel technique to transform a fractal LPF to BPF using a simple combination of defected ground structure (DGS) and a narrow gap capacitive," *Proc. APMC,* pp. 2385-2388, 2007.

[4] S. Amari, "Synthesis of cross-coupled resonator filters using an analytical gradiant-based optimization technique," *IEEE Trans. Microwave Theory Tech.*, vol. 48, no. 9, pp. 1559-1564, Sep. 2000.

[5] A. Boutejdar, A. Elsherbeni, and A. Omar, "Design of a novel ultra-wide stopband lowpass filter using H-defected ground structure," *Microwave and Optical Technology Lett.*, Wiley, pp. 771-775, 2008.

[6] Q. Xue, K. M. Shum, and C. H. Chan, "Novel 1-D microstrip PBG Cells," *IEEE microwave and Wireless Components Lett.*, vol. 10, no. 10, pp. 403-405, October 2000.

[7] C. Kim, J. S. Park, A. Dal, and J. Kim, "A novel 1-D periodic defected ground structure for planar circuits," *IEEE Microwave Guided Wave Lett.*, vol. 10, pp. 131–133, Apr. 2000.

[8] J. S. Hong and M. J. Lancaster, *Microstrip Filters for RF/Microwave Applications*, Wiley, 2001.

[9] A. Boutejdar, S. Amari, and A. Omar, "A novel compact J-admittance inverter-coupled microstrip bandpass filter using arrowhead-shape as defected ground structure," *Microwave and Optical Technology Lett.*, vol. 52. no. 1, pp. 34-38, 2010.

[10] C. -F. Chen, T. -Y. Huang, C. -H. Tseng, R.-B. Wu, and T. -W. Chen, "A miniaturized

multilayer quasi-elliptic bandpass filter with aperture-coupled microstrip resonators," *IEEE Transactions on Microwave Theory and Techniques*, vol. 53, no. 9, September 2005.

[11] A. B. Abdel-Rahman, A. K. Verma, A. Boutejdar, and A. S. Omar, "Control of bandstop response of Hi-Lo microstrip low-pass filter using slot in ground plane," *IEEE Transactions on Microwave Theory and Techniques*, vol. 52, no. 3, March 2004.

[12] D. Ahn, J. Park, C. Kim, Y. Qian, and T. Itoh, "A design of the lowpass filter using the novel microstrip defected ground structure," *IEEE Transactions on microwave Theory and Techniques*, vol. 49, pp. 86-93, Jan. 2001.

[13] A. Boutejdar and A. Omar, "Lowpass-to-bandpass transformation using J-inverter and defected ground structure (DGS) technique," *International Workshop on Microwave Filters CNES,* November 2009.

Mohamed Al Sharkawy was born in Alexandria, Egypt, in 1978. He graduated from the Department of Electrical Engineering, Arab Academy for Science and Technology (AAST), Alexandria, Egypt, in June 2000, and received both, the M.Sc. and the Ph.D. degrees in Electrical Engineering from the University of Mississippi, USA, in October 2003, and December 2006, respectively. From 2002 to 2006, he worked as a research assistant then as a visiting scholar at the Department of Electrical Engineering at the University of Mississippi till June 2007. Currently, he is an Assistant Professor at the Electronics and Communications Department at the Arab Academy for Science and Technology, Egypt, where he is currently teaching graduate and undergraduate courses. His research interests include electromagnetic scattering from parallel chiral and metamaterial cylinders and the application of finite difference time and frequency domain techniques for the analysis and design of compact and ultra wideband antennas and microwave devices for wireless communications, radar applications, and breast cancer detection. He has more than 45 papers in international journals and proceedings of international and national symposia, and one book by Morgan & Claypool.

Ahmed Boutejdar was born in Souk El-Arbaa Gharb, Marocco, in 1969. He received the Diplom (Licence) in Mathematics and Physics from Ibn Tofeil University, Kénitra, Morocco in 1993. From 1994 to 1995 Preparatory Year of Engineering High School in Köthen. B.Sc. in and Diplom-Eng degrees in Electrical Engineering, Communication, and Microwave Engineering from Otto-von-Guericke University, Magdeburg, Germany in 1999 and 2004 respectively, and the Ph.D. degree in Communication and High Frequency -technique from the University of Magdeburg in 2009. His research interests include the design and analysis of microstrip filters, Defected Ground Structures and microstrip antennas. Mr. Boutejdar has authored over 90 papers in international journals and proceedings of international and national symposia and a boock-chapter in "Ultra-Wideband, Short Pulse Electromagnetics 9" Springer 2010. He is a member and reviewer of the IEEE region 8 Conference 07. He is reviewer of the Mediterranean Microwave Conference (MMS). He is reviewer of the Hindawi Publishing Corporation/ International Journal of Microwave science and Technology (IJMST). He is reviewer of Electronics Letters. He is reviewer of The 5th international conference SETIT 2009: Sciences of Electronic, Technologies of Information and Telecommunications, Hammamet, Tunisia. He is reviewer of Knowledge Generation, Communication and Management: KGCM 2008 Multi-Conference on Systemics, Cybernetics and Informatics: WMSCI 2008. He is reviewer of the Progress in Electromagnetics Research Symposium (PIERS), he is reviewer of the International Conference on Communications and Electronics (ICCE).

Fatma M. Elhefnawi (B.Sc.67, M.Sc. 74, Ph.D.79) is at the Electronic Research institute and with NARSS at the Egyptian Space Program and head of the Antenna Department. Her interests include antenna analysis and synthesis, numerical methods in antenna and arrays, also effects of microwave on dispersive media, in addition to some engineering biomedical applications.

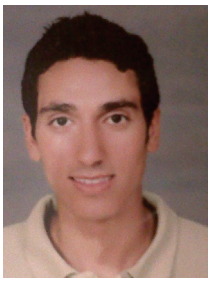

Omar Luxor was born in Alexandria, Egypt in 1984. He received the B.Sc. in Electronics and Communication Engineering from the Arab Academy for Science and Technology, Alexandria, Egypt. He is currently working towards his M.Sc. Degrees at the AAST. His research interests include design and analysis of microstrip antennas and filters.

Computationally Efficient Multi-Fidelity Multi-Grid Design Optimization of Microwave Structures

Slawomir Koziel

Engineering Optimization & Modeling Center, School of Science and Engineering,
Reykjavik University, 101 Reykjavik, Iceland
koziel@ru.is

***Abstract*—** A simple and reliable algorithm for design optimization of microwave structures is introduced. The presented methodology exploits coarse-discretization models of the structure of interest, starting from a very coarse mesh, and gradually increases the discretization density. Each model is optimized using a simple grid-search routine. The optimal design of the current model is used as an initial design for the finer-discretization one. The proposed methodology is computationally efficient as most of the operations are performed on coarse-discretization models. Three examples of microstrip filter designs are given.

***Index Terms*—** Computer-aided design (CAD), electromagnetic simulation, derivative-free optimization, grid search, microwave design.

I. INTRODUCTION

Due to the complexity of microwave structures and a growing demand for accuracy, theoretical models can only be used to yield initial designs that need to be further tuned to meet given performance specifications. Therefore, EM-simulation-based design closure becomes increasingly important. A serious bottleneck of simulation-driven optimization is its high computational cost, which makes straightforward approaches such as employing EM solvers directly in an optimization loop impractical. Co-simulation [1-3] is only a partial solution because the circuit models with embedded EM components are still directly optimized.

Efficient simulation-driven design can be realized using a surrogate-based optimization (SBO) principle [4], [5], where the optimization burden is shifted to a surrogate model, computationally cheap representation of the structure being optimized (referred to as the fine model). The successful SBO approaches used in microwave area include space mapping (SM) [6-12] and various forms of tuning [13-15] and tuning SM [16], [17]. Unfortunately, their implementation is not always straightforward: substantial modification of the optimized structure may be required (tuning), or additional mapping and more or less complicated interaction between auxiliary models is necessary (SM). Also, space mapping performance heavily depends on the proper selection of the surrogate model and its parameters [18].

Here, a simple yet efficient design optimization methodology is introduced. Our technique is based on iterative optimization of coarse-discretization models using a simple grid-search algorithm. The optimal design of the current model is used as an initial design for the finer-discretization one. The final design can be refined using a second-order polynomial approximation of the available EM-simulation data.

The proposed methodology is very simple to implement. Unlike space mapping or other surrogate-based approaches, it does not require a circuit-equivalent coarse model or any modification of the structure being optimized. It is also computationally efficient because the optimization burden is shifted to the coarsely-discretized models. As our technique is based on a grid-search routine, it allows design optimization of structures simulated with solvers using structured grids such as Sonnet ***em*** [19].

II. MULTI-FIDELITY MULTI-GRID DESIGN OPTIMIZATION

In this section, we formulate the optimization problem (Section II.A), describe the building blocks of the proposed optimization procedure (Sections II.B-II.E), formulate the procedure (Section II.F), and discuss some practical issues (Section II.G).

A. Design Optimization Problem

The design optimization problem is formulated as follows:

$$\boldsymbol{x}_f^* = \arg\min_{\boldsymbol{x}} U\left(\boldsymbol{R}_f(\boldsymbol{x})\right) \quad (1)$$

where $\boldsymbol{R}_f \in R^m$ denotes the response vector of a fine model of the device of interest, e.g., the modulus of the reflection coefficient $|S_{21}|$ evaluated at m different frequencies; $\boldsymbol{x} \in R^n$ is a vector of design variables, and U is a given scalar merit function, e.g., a minimax function with upper and lower specifications. Vector $\boldsymbol{x}_f^*$ is the optimal design to be determined.

As mentioned in the introduction, the fine model is assumed to be computationally expensive so that its straightforward optimization (e.g., using gradient-based search) is prohibitive because of high computational cost.

Here, the fine model is evaluated on a simulation grid $d_{1.f} \times d_{2.f} \times \ldots \times d_{n.f}$ that determines the resolution of the design optimization process (see Fig. 3 for illustration). In case of Sonnet ***em***, $d_{k.f}$ is equal to either $g_{h.f}$ or $g_{v.f}$ (the horizontal or vertical cell size used by the EM solver).

$\boldsymbol{x}^{(j)} = s(\boldsymbol{x}^{(j-1)})$; // Snap $\boldsymbol{x}^{(j)}$ to the nearest grid point
$U_{min} = U(\boldsymbol{R}_{c.f}(\boldsymbol{x}^{(j)}))$; // Evaluate objective function
do
  $U_0 = U_{min}$; // Update the reference objective function value
  for $k = 1$ to n // Evaluating objective function at perturbed designs
    $U_k = U(\boldsymbol{R}_{c.f}([x_1^{(j)} \ldots x_k^{(j)} + d_{k.j} \ldots x_n^{(j)}]^T))$; // (here, $d_k = g_{h.j}$ or $g_{v.j}$ (depends on orientation of $x_k^{(j)}$))
  end
  $\boldsymbol{h} = -[(U_1 - U_0)/d_{1.j} \ldots [(U_n - U_0)/d_{n.j}]^T$; // Search direction estimation
  $\boldsymbol{h} = \boldsymbol{h} \cdot (\|[d_{1.j} \ldots d_{n.j}]^T\|/\|\boldsymbol{h}\|)$; // Search direction normalization
  do // Line search:
    $\boldsymbol{x}_{tmp} = s(\boldsymbol{x}^{(j)} + \boldsymbol{h})$; // Set the trial design and "snap" it to the grid
    $U_{tmp} = U(\boldsymbol{R}_{c.f}(\boldsymbol{x}_{tmp}))$; // Evaluate objective function at the trial design
    if $U_{tmp} < U_{min}$ // If the trial is successful:
      $\boldsymbol{x}^{(j)} = \boldsymbol{x}_{tmp}$; // 1. Update the design
      $U_{min} = U_{tmp}$; // 2. Store the best result
      $\boldsymbol{h} = 2 \cdot \boldsymbol{h}$; // 3. Increase the search step
    else
      break; // Otherwise, exit the line search algorithm
    end
  while 1
  if $U_{min} \geq U_0$ // Line search failed => perform local search
    for $k = 1$ to n
      $U_{-k} = U(\boldsymbol{R}_{c.f}([x_1^{(j)} \ldots x_k^{(j)} - d_{k.j} \ldots x_n^{(j)}]^T))$; // Evaluate the remaining neighbours of $\boldsymbol{x}^{(j)}$
    end
    $U_{tmp} = \min\{U_{-k}, U_{-k+1}, \ldots, U_{k-1}, U_k\}$; // Find the best design
    $k_{tmp} = \text{argmin}\{-n \leq k \leq n : U_k\}$; // Fine the corresponding perturbation index
    if $U_{min} < U_0$ // If local search is successful:
      $\boldsymbol{x}^{(j)} = [x_1^{(j)} \ldots x_k^{(j)} + \text{sign}(k_{tmp}) \cdot d_{k.j} \ldots x_n^{(j)}]^T$; // 1. Update the design
      $U_{min} = U_{k_{tmp}}$; // 2. Store the best value
    end
  end
while $U_{min} < U_0$ // Continue if further improvement was possible
return $\boldsymbol{x}^{(j)}$; // Otherwise, return $\boldsymbol{x}^{(j)}$ as the optimal design of $\boldsymbol{R}_{c.j}$

Fig. 1. Pseudo-code of the grid-search algorithm.

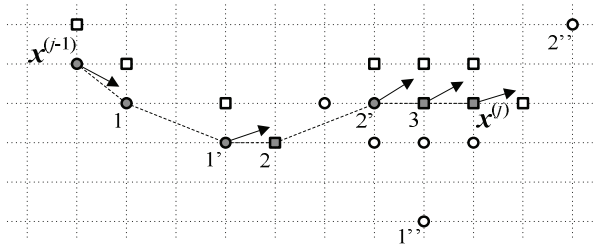

Fig. 2. Illustration of the grid-search algorithm for two design variables (n = 2). The search direction ($\rightarrow$) at the initial design $\boldsymbol{x}^{(j-1)}$ is obtained using two perturbed designs marked as squares. The trial points for the line search are denoted as 1, 1' and 1''. The last successful trial design is 1'. At this design, a new search direction is found, and a new line search is launched with designs 2, 2' and 2'' (the last of which is unsuccessful). The next line search starting from 2' is unsuccessful and the new design 3 is obtained using a local search, similarly as the final design $\boldsymbol{x}^{(j)}$ that cannot be further improved even by a local search, which terminates the algorithm.

B. Coarse-Discretization Models

The optimization technique introduced here exploits a family of coarse-discretization models $\{\boldsymbol{R}_{c.j}\}$, $j = 1, \ldots, K$, all evaluated using the same EM solver. The model $\boldsymbol{R}_{c.j}$ exploits a simulation grid $d_{1.j} \times d_{2.j} \times \ldots \times d_{n.j}$. It is assumed that $d_{k.j} > d_{k.j+1}$ and for $k = 1, \ldots, n$ and $j = 1, \ldots, K-1$, and $d_{k.K} > d_{k.f}$ for all k. In other words, discretization of $\boldsymbol{R}_{c.j+1}$ is finer than that of $\boldsymbol{R}_{c.j}$. It is recommended that $d_{k.j}/d_{k.j+1}$ is an integer (typically 2 or 3). In practice, the number K of coarse-discretization models is two or three.

C. Grid-Search Algorithm

To optimize the coarse-discretization model $\boldsymbol{R}_{c.j}$ we use the grid-search procedure shown in Fig. 1. Here, $\boldsymbol{x}^{(j-1)} = [x_1^{(j-1)} \ \ldots \ x_n^{(j-1)}]^T$ is the initial design, i.e., the optimal design of $\boldsymbol{R}_{c.j-1}$, s is a function that "rounds" $\boldsymbol{x}$ to the nearest grid point $s(\boldsymbol{x})$).

For simplicity, only the unconstrained version of the grid-search algorithm is described here. The generalization for constrained optimization is straightforward. The operation of the algorithm is illustrated in Fig. 2.

D. Design Refinement

Having optimized the finest of the coarse-discretization models, $\boldsymbol{R}_{c.K}$, we also have its evaluations at $\boldsymbol{x}^{(K)}$ and at all perturbed designs around it $\boldsymbol{x}_k^{(K)} = [x_1^{(K)} \ \ldots \ x_k^{(K)} + \text{sign}(k)\cdot d_{k.K} \ \ldots \ x_n^{(K)}]^T$, i.e., $\boldsymbol{R}^{(k)} = \boldsymbol{R}_{c.K}(\boldsymbol{x}_k^{(K)})$, $k = -n, -n+1, \ldots, n-1, n$. This data can be used to refine the final design without directly optimizing $\boldsymbol{R}_f$. Instead, one can set up an approximation model involving $\boldsymbol{R}^{(k)}$ and optimize it in the neighbourhood of $\boldsymbol{x}^{(K)}$ defined as $[\boldsymbol{x}^{(K)} - \boldsymbol{d}, \boldsymbol{x}^{(K)} + \boldsymbol{d}]$, where $\boldsymbol{d} = [d_{1.K} \ d_{2.K} \ \ldots \ d_{n.K}]^T$. In this work, we use a reduced quadratic model $\boldsymbol{q}(\boldsymbol{x}) = [q_1 \ q_2 \ \ldots \ q_m]^T$, defined as

$$q_j(\boldsymbol{x}) = q_j([x_1 \ldots x_n]^T) = \lambda_{j.0} + \lambda_{j.1}x_1 + \ldots + \ldots + \lambda_{j.n}x_n + \lambda_{j.n+1}x_1^2 + \ldots + \lambda_{j.2n}x_n^2 \quad (2)$$

Coefficients $\lambda_{j.r}$, $j = 1, \ldots, m$, $r = 0, 1, \ldots, 2n$, can be uniquely obtained by solving the linear regression problems $q_j(\boldsymbol{x}_k^{(K)}) = R_j^{(k)}$, $k = -n, -n+1, \ldots, n-1, n$, where $R_j^{(k)}$ is a jth component of the vector $\boldsymbol{R}^{(k)}$.

In order to account for possible misalignment between $\boldsymbol{R}_{c.K}$ and $\boldsymbol{R}_f$, it is recommended—instead of optimizing the quadratic model $\boldsymbol{q}$—to optimize a corrected model $\boldsymbol{q}(\boldsymbol{x}) + [\boldsymbol{R}_f(\boldsymbol{x}^{(K)}) - \boldsymbol{R}_{c.K}(\boldsymbol{x}^{(K)})]$ that ensures a zero-order consistency [20] between $\boldsymbol{R}_{c.K}$ and $\boldsymbol{R}_f$. The refined design can be then found as

$$\boldsymbol{x}^* = \arg\min\{\boldsymbol{x}^{(K)} - \boldsymbol{d} \le \boldsymbol{x} \le \boldsymbol{x}^{(K)} + \boldsymbol{d} : U(\boldsymbol{q}(\boldsymbol{x}) + [\boldsymbol{R}_f(\boldsymbol{x}^{(K)}) - \boldsymbol{R}_{c.K}(\boldsymbol{x}^{(K)})])\} \quad (3)$$

If necessary, the step (3) can be performed a few times starting from a refined design, i.e., $\boldsymbol{x}^* = \text{argmin}\{\boldsymbol{x}^{(K)} - \boldsymbol{d} \le \boldsymbol{x} \le \boldsymbol{x}^{(K)} + \boldsymbol{d} : U(\boldsymbol{q}(\boldsymbol{x}) + [\boldsymbol{R}_f(\boldsymbol{x}^*) - \boldsymbol{R}_{c.K}(\boldsymbol{x}^*)])\}$ (each iteration requires only one evaluation of $\boldsymbol{R}_f$).

E. Optional Design Specifications Adjustments

Typically, the major difference between the responses of $\boldsymbol{R}_f$ and coarse-discretization models $\boldsymbol{R}_{c.j}$ is that they are shifted in frequency. This difference can be easily absorbed by frequency-shifting the design specifications while optimizing a model $\boldsymbol{R}_{c.j}$. More specifically, suppose that the design specifications are described as $\{\omega_{k.L}, \omega_{k.H}; s_k\}$, $k = 1, \ldots, n_s$, (e.g., specifications $|S_{21}| \ge -3$ dB for 3 GHz $\le \omega \le 4$ GHz, $|S_{21}| \le -20$ dB for 1 GHz $\le \omega \le 2$ GHz and $|S_{21}| \le -20$ dB for 5 GHz $\le \omega \le 7$ GHz would be described as {3, 4; –3}, {1, 2; –20}, and {5, 7; –20}). If the average frequency shift between responses of $\boldsymbol{R}_{c.j}$ and $\boldsymbol{R}_{c.j+1}$ is $\Delta\omega$, this difference can be absorbed by modifying the design specifications to $\{\omega_{k.L} - \Delta\omega, \omega_{k.H} - \Delta\omega, s_k\}$, $k = 1, \ldots, n_s$.

F. Optimization Algorithm

The optimization procedure proposed in this work can be summarized as follows (input arguments are: initial design $\boldsymbol{x}^{(0)}$ and the number of coarse-discretization models K):

1. Set $j = 1$;
2. Optimize $\boldsymbol{R}_{c.j}$ using the algorithm of Section 2.*B* to obtain a new design $\boldsymbol{x}^{(j)}$;
3. Set $j = j + 1$; if $j < K$ go to 2;
4. Set up a quadratic model $\boldsymbol{q}$ as in (2) and find a refined design $\boldsymbol{x}^*$ using (3).

Note that the original model $\boldsymbol{R}_f$ is only evaluated at the final stage (step 4) of the optimization process. Operation of our optimization procedure is illustrated in Fig. 3.

G. Selection of the Coarse-Discretization Models

As mentioned in Section II.*B*, the number K of coarse-discretization models is typically two or three. The first coarse-discretization model $\boldsymbol{R}_{c.1}$ should be set up so that its evaluation time is at least 30 to 100 times shorter than the evaluation time of the fine model. The reason is that the initial design may be quite poor so that the expected number of evaluations of $\boldsymbol{R}_{c.1}$ is usually large. By keeping $\boldsymbol{R}_{c.1}$ fast, one can control the computational overhead related to its optimization. Accuracy of $\boldsymbol{R}_{c.1}$ is not critical because its optimal design is only supposed to give a rough estimate of the fine model optimum.

The second (and, possibly third) coarse-discretization model should be more accurate but still at least about 10 times faster than the fine model. This can be achieved by proper manipulation of the EM solver mesh density.

III. EXAMPLES

A. Compact Stacked Slotted Resonators Microstrip Bandpass Filter [21]

Consider the stacked slotted resonators bandpass filter [21] shown in Fig. 4. The design parameters are $\boldsymbol{x} = [L_1\ L_2\ W_1\ S_1\ S_2\ d]^T$ mm. The filter is simulated in Sonnet ***em*** [19] using a cell size of 0.05 mm × 0.05 mm (model $\boldsymbol{R}_f$), which corresponds to a simulation grid $d_{1.f} \times d_{2.f} \times \ldots \times d_{n.f}$ of 0.05 × 0.05 × … × 0.05 mm. The design specifications are $|S_{21}| \geq -3$ dB for 2.35 GHz ≤ ω ≤ 2.45 GHz, and $|S_{21}| \leq -20$ dB for 1.9 GHz ≤ ω ≤ 2.3GHz and 2.6 GHz ≤ ω ≤ 2.9 GHz. The initial design is $\boldsymbol{x}^{(0)} = [7\ 10\ 0.6\ 1\ 2\ 1]^T$ mm.

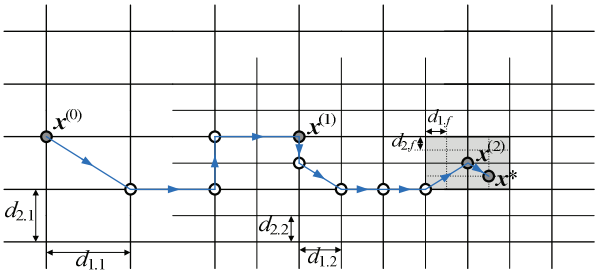

Fig. 3. Operation of the proposed optimization procedure for $n = 2$ and $K = 2$: Optimized design $\boldsymbol{x}^{(1)}$ of the model $\boldsymbol{R}_{c.1}$ is found on the grid $d_{1.1} \times d_{2.1}$ starting from the initial design $\boldsymbol{x}^{(0)}$. Then, the optimized design $\boldsymbol{x}^{(2)}$ of $\boldsymbol{R}_{c.2}$ is searched for on the grid $d_{2.2} \times d_{2.2}$ using $\boldsymbol{x}^{(1)}$ as the initial design. Finally, the design $\boldsymbol{x}^{(2)}$ is refined (cf. (3)) on the fine grid $d_{1.f} \times d_{2.f}$ using a second-order polynomial model (2) that is set up in the shaded area around $\boldsymbol{x}^{(2)}$.

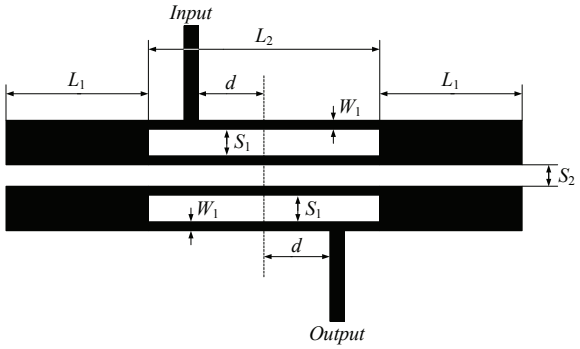

Fig. 4. Stacked slotted resonators filter: geometry [21].

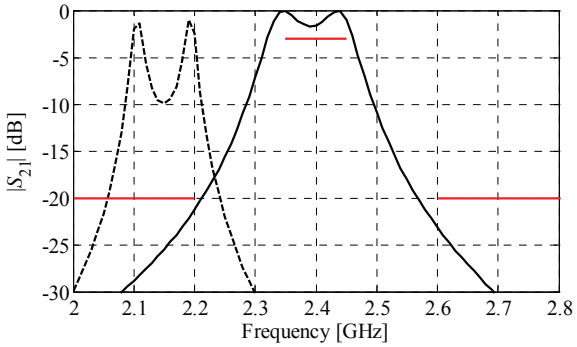

Fig. 5. Stacked slotted resonators filter: responses of the coarse-discretization model $\boldsymbol{R}_{c.1}$ (0.2 mm × 0.2 mm grid) at the initial design $\boldsymbol{x}^{(0)}$ (dashed line) and at the optimized design of $\boldsymbol{R}_{c.1}$, $\boldsymbol{x}^{(1)}$, (solid line).

Table 1: Optimization cost of the stacked slotted resonators bandpass filter.

Algorithm Component	Number of Model Evaluations	Evaluation Time	
		Absolute [min]	Relative to $\boldsymbol{R}_f$
Optimization of the coarse-discretization model $\boldsymbol{R}_{c.1}$	41	49	3.1
Optimization of the coarse-discretization model $\boldsymbol{R}_{c.2}$	26	130	8.1
Evaluation of the original (fine-discretization) model $\boldsymbol{R}_f$	2	32	2.0
Total optimization time	N/A	211	13.2

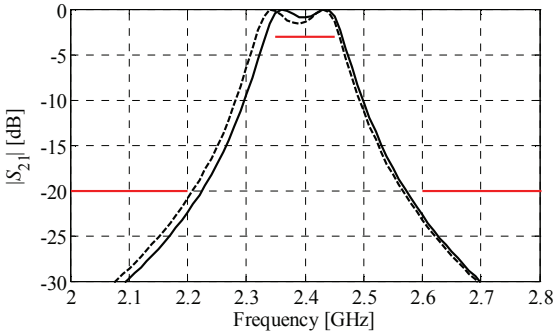

Fig. 6. Stacked slotted resonators filter: responses of the coarse-discretization model $\boldsymbol{R}_{c.2}$ (0.05 mm × 0.2 mm grid) at $\boldsymbol{x}^{(1)}$ (dashed line) and at $\boldsymbol{x}^{(2)}$ (solid line), the optimized design of $\boldsymbol{R}_{c.2}$ found using a grid search.

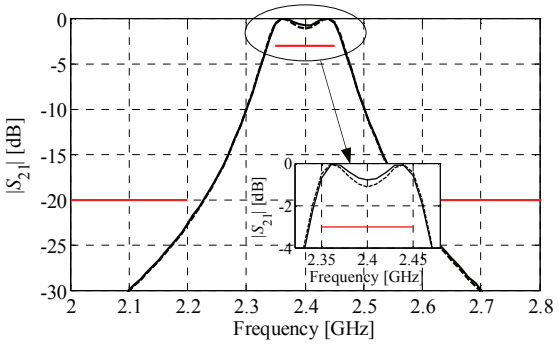

Fig. 7. Stacked slotted resonators filter: responses of the original fine-discretization model $\boldsymbol{R}_f$ at $\boldsymbol{x}^{(2)}$ (dashed line) and at the refined final design $\boldsymbol{x}^*$ (solid line).

The proposed multi-fidelity multi-grid design optimization procedure is realized here using two coarse-discretization models: $\boldsymbol{R}_{c.1}$ (cell size 0.2 mm × 0.2 mm, simulation grid $0.2 \times 0.2 \times \ldots \times 0.2$ mm) and $\boldsymbol{R}_{c.2}$ (cell size 0.05 mm × 0.2 mm, simulation grid 0.05 × 0.05 × 0.2 × 0.2 × 0.2 × 0.05 mm). The evaluation times for $\boldsymbol{R}_{c.1}$, $\boldsymbol{R}_{c.2}$ and $\boldsymbol{R}_f$ are 72 s, 5 min and 16 min, respectively.

Figure 5 shows the responses of $\boldsymbol{R}_{c.1}$ at $\boldsymbol{x}^{(0)}$ and at $\boldsymbol{x}^{(1)} = [6.4\ 9.6\ 0.6\ 0.6\ 2\ 1.8]^T$ mm, its optimal design found using a grid search. Figure 6 shows the responses of $\boldsymbol{R}_{c.2}$ at $\boldsymbol{x}^{(1)}$ and at its optimized design $\boldsymbol{x}^{(2)} = [6.35\ 9.6\ 0.6\ 0.6\ 2.2\ 1.8]^T$ mm. Figure 7 shows the responses of $\boldsymbol{R}_f$ at $\boldsymbol{x}^{(2)}$ (specification error –1.7 dB) and the refined design $\boldsymbol{x}^* = [6.35\ 9.6\ 0.6\ 0.6\ 2.25\ 1.85]^T$ mm (specification error –2.1 dB). The total optimization cost (Table 1) is quite low and corresponds to only 13 evaluations of the original, fine-discretization model. Most of this cost is due to the optimization of the coarse-discretization model $\boldsymbol{R}_{c.2}$.

B. High-Temperature Superconducting Filter [22]

As the second example, consider the high-temperature superconducting (HTS) filter shown in Fig. 8 [22]. The design parameters are $\boldsymbol{x} = [L_1\ L_2\ L_3\ S_1\ S_2\ S_3]^T$. The width of all the sections is $W = 8$ mil. A substrate of lanthanum aluminate is used with $\varepsilon_r = 23.425$ $H = 20$ mil. The filter is simulated in Sonnet ***em*** [19] using a grid of 0.5 mil × 0.5 mil (the $\boldsymbol{R}_f$ model). The design specifications are $|S_{21}| \leq 0.05$ for $\omega \leq 3.966$ GHz, $|S_{21}| \geq 0.95$ for 4.008 GHz $\leq \omega \leq 4.058$ GHz, and $|S_{21}| \leq 0.05$ for $\omega \geq 4.100$ GHz. The initial design is $\boldsymbol{x}^{(0)} = [196\ 196\ 190\ 20\ 92\ 100]^T$ mil.

Again, we use two coarsely discretized models: $\boldsymbol{R}_{c.1}$ (grid of 2 mil × 4 mil) and $\boldsymbol{R}_{c.2}$ (grid of 1 mil × 2 mil). The evaluation times for $\boldsymbol{R}_{c.1}$, $\boldsymbol{R}_{c.2}$ and $\boldsymbol{R}_f$ are about 2 min, 6 min and 51 min, respectively. Figure 9 shows the responses of $\boldsymbol{R}_{c.1}$ at $\boldsymbol{x}^{(0)}$ and at $\boldsymbol{x}^{(1)} = [188\ 190\ 188\ 20\ 76\ 84]^T$ mil, its optimal design found using a grid search, as well as the response of $\boldsymbol{R}_{c.2}$ at $\boldsymbol{x}^{(0)}$. Because of noticeable frequency shift between $\boldsymbol{R}_{c.1}(\boldsymbol{x}^{(0)})$ and $\boldsymbol{R}_{c.2}(\boldsymbol{x}^{(0)})$ (7 MHz on average) the design specifications were adjusted as described in Section II.*E* while optimizing $\boldsymbol{R}_{c.1}$. Figure 10 shows the responses of $\boldsymbol{R}_{c.2}$ at $\boldsymbol{x}^{(1)}$ and at its optimized design $\boldsymbol{x}^{(2)} = [188\ 189\ 188\ 20\ 76\ 86]^T$ mil, as well as the response of $\boldsymbol{R}_f$ at $\boldsymbol{x}^{(2)}$. Here, the average frequency shift between $\boldsymbol{R}_{c.2}(\boldsymbol{x}^{(1)})$ and $\boldsymbol{R}_f(\boldsymbol{x}^{(1)})$ is about 5 MHz

Table 2: Optimization cost of the HTS filter.

Algorithm Component	Number of Model Evaluations	Evaluation Time	
		Absolute [min]	Relative to $\boldsymbol{R}_f$
Optimization of the coarse-discretization model $\boldsymbol{R}_{c.1}$	104	195	3.8
Optimization of the coarse-discretization model $\boldsymbol{R}_{c.2}$	26	152	3.0
Evaluation of the original (fine-discretization) model $\boldsymbol{R}_f$	3	153	3.0
Total optimization time	N/A	500	9.8

Table 3: Optimization cost of the coupled-line bandpass filter.

Algorithm Component	Number of Model Evaluations	Evaluation Time	
		Absolute [min]	Relative to $\boldsymbol{R}_f$
Optimization of the coarse-discretization model $\boldsymbol{R}_{c.1}$	82	42	1.0
Optimization of the coarse-discretization model $\boldsymbol{R}_{c.2}$	55	276	6.4
Evaluation of the original (fine-discretization) model $\boldsymbol{R}_f$	2	86	2.0
Total optimization time	N/A	404	9.4

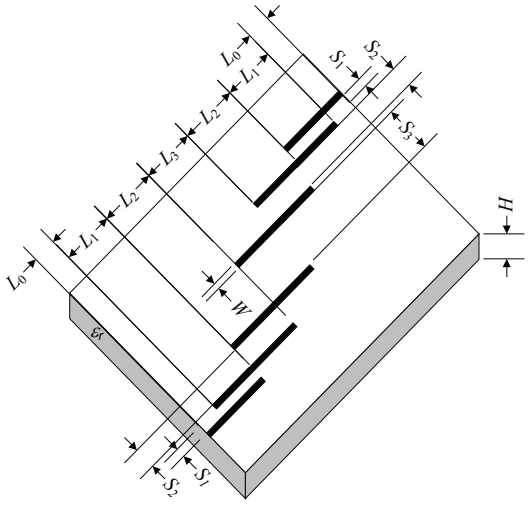

Fig. 8. HTS filter: geometry [22].

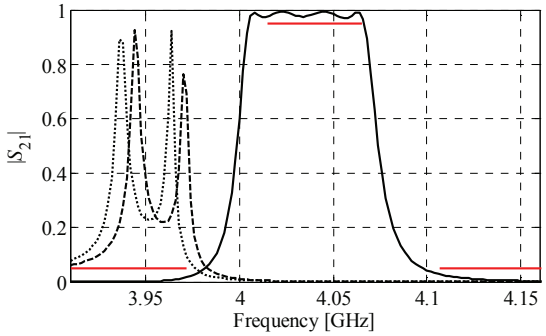

Fig. 9. HTS filter: responses of the coarse-discretization model $\boldsymbol{R}_{c.1}$ at the initial design $\boldsymbol{x}^{(0)}$ (dashed line) and at its optimized design $\boldsymbol{x}^{(1)}$ (solid line), as well as the response of $\boldsymbol{R}_{c.2}$ at $\boldsymbol{x}^{(0)}$ (dotted line); design specifications are shifted by 7 MHz towards higher frequencies to absorb the frequency shift between $\boldsymbol{R}_{c.1}(\boldsymbol{x}^{(0)})$ and $\boldsymbol{R}_{c.2}(\boldsymbol{x}^{(0)})$.

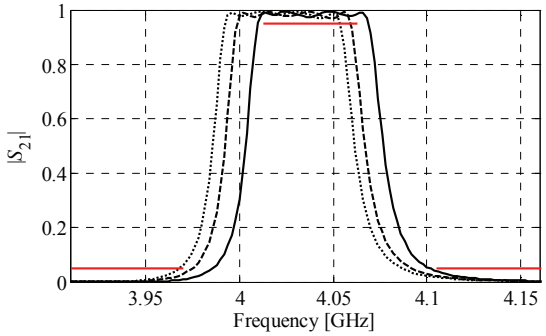

Fig. 10. HTS filter: responses of the coarse-discretization model $\boldsymbol{R}_{c.2}$ at $\boldsymbol{x}^{(1)}$ (dashed line) and at its optimized design $\boldsymbol{x}^{(2)}$ (solid line), as well as the response of $\boldsymbol{R}_f$ at $\boldsymbol{x}^{(2)}$ (dotted line); design specifications are shifted by 5 MHz toward higher frequencies to absorb the frequency shift between $\boldsymbol{R}_{c.2}(\boldsymbol{x}^{(1)})$ and $\boldsymbol{R}_f(\boldsymbol{x}^{(1)})$.

and the design specifications are modified accordingly. Figure 11 shows the responses of $\boldsymbol{R}_f$ at $\boldsymbol{x}^{(2)}$ (specification error –0.01) and the refined design $\boldsymbol{x}^* = [188\ 189\ 188\ 20.5\ 78\ 88]^T$ mm (specification error –0.02). Total optimization cost (Table 2) corresponds to only 10 evaluations of the fine-discretization model.

C. Coupled-Line Microstrip Bandpass Filter [23]

Consider the coupled-line bandpass filter [23] shown in Fig. 12. The design parameters are $\boldsymbol{x} = [L_1\ L_2\ L_3\ L_4\ S_1\ S_2]^T$ mm. The fine model $\boldsymbol{R}_f$ is simulated in FEKO [24]. The initial design is $\boldsymbol{x}^{(0)} = [18.0\ 7.0\ 15.0\ 10.0\ 0.2\ 0.2]^T$ mm. The total mesh number for $\boldsymbol{R}_f$ at the initial design is 1422.

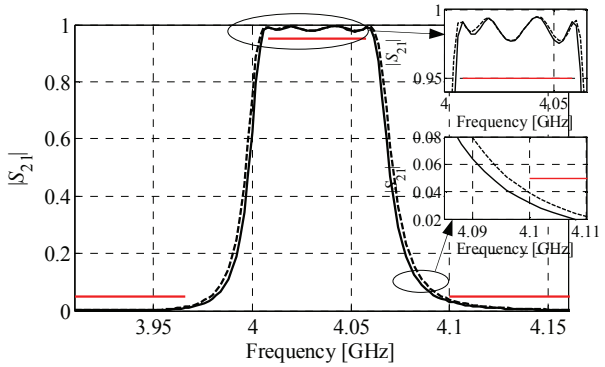

Fig. 11. HTS filter: responses of the fine-discretization model $\boldsymbol{R}_f$ at $\boldsymbol{x}^{(2)}$ (dashed line) and at the refined final design $\boldsymbol{x}^*$ (solid line); here the original design specifications are shown.

The design specifications are $|S_{21}| \geq -1$ dB for 2.35 GHz $\leq \omega \leq$ 2.45 GHz, and $|S_{21}| \leq -20$ dB for 1.5 GHz $\leq \omega \leq$ 2.25GHz and 2.55 GHz $\leq \omega \leq$ 3.3 GHz.

We are using two coarse models: $\boldsymbol{R}_{c.1}$ (total mesh number 160 at $\boldsymbol{x}^{(0)}$, simulation grid 0.1 × 0.1 × 0.1 × 0.1 × 0.02 × 0.02 mm) and $\boldsymbol{R}_{c.2}$ (total mesh number 678 at $\boldsymbol{x}^{(0)}$, simulation grid 0.05 × 0.05 × 0.05 × 0.05 × 0.01 × 0.01 mm). The evaluation times for $\boldsymbol{R}_{c.1}$, $\boldsymbol{R}_{c.2}$ and $\boldsymbol{R}_f$ are about 30 seconds, 5 min and 43 min, respectively. Figure 13 shows the responses of $\boldsymbol{R}_{c.1}$ at $\boldsymbol{x}^{(0)}$ and at $\boldsymbol{x}^{(1)} = [18.0\ 7.0\ 13.8\ 10.2\ 0.2\ 0.1]^T$ mm, as well as the response of $\boldsymbol{R}_{c.2}$ at $\boldsymbol{x}^{(0)}$. Because of the frequency shift between $\boldsymbol{R}_{c.1}(\boldsymbol{x}^{(0)})$ and $\boldsymbol{R}_{c.2}(\boldsymbol{x}^{(0)})$, the design specifications were adjusted accordingly (cf. Section II.*E*) while optimizing $\boldsymbol{R}_{c.1}$. Figure 14 shows the responses of $\boldsymbol{R}_{c.2}$ at $\boldsymbol{x}^{(1)}$ and at its optimized design $\boldsymbol{x}^{(2)} = [18.0\ 7.0\ 13.7\ 10.2\ 0.18\ 0.12]^T$ mm, as well as the response of $\boldsymbol{R}_f$ at $\boldsymbol{x}^{(2)}$. Figure 15 shows the responses of $\boldsymbol{R}_f$ at $\boldsymbol{x}^{(2)}$ (specification error +0.02 dB) and the refined design $\boldsymbol{x}^* = [17.994\ 7.013\ 13.663\ 10.138\ 0.128\ 0.118]^T$ mm (specification error –0.74 dB). Note that, in this case, the refinement step (3) was not constrained to the simulation grid.

Total optimization cost (Table 3) corresponds to less than 10 evaluations of the fine-discretization model. Similarly as for the first test problem, optimization of the second coarse-discretization model $\boldsymbol{R}_{c.2}$ was the major contributor to the computational cost.

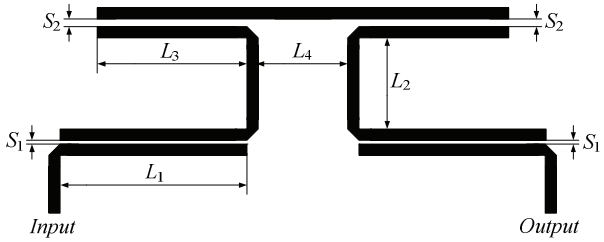

Fig. 12. Coupled-line bandpass filter: geometry [23].

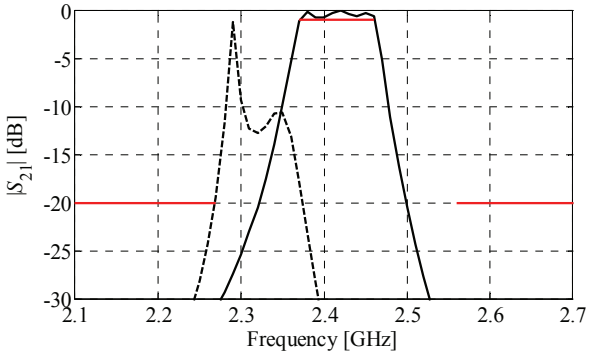

Fig. 13. Coupled-line bandpass filter: responses of $\boldsymbol{R}_{c.1}$ at the initial design $\boldsymbol{x}^{(0)}$ (dashed line) and at its optimized design $\boldsymbol{x}^{(1)}$ (solid line), as well as the response of $\boldsymbol{R}_{c.2}$ at $\boldsymbol{x}^{(0)}$ (dotted line); design specifications are adjusted to absorb the frequency shift between $\boldsymbol{R}_{c.1}(\boldsymbol{x}^{(0)})$ and $\boldsymbol{R}_{c.2}(\boldsymbol{x}^{(0)})$.

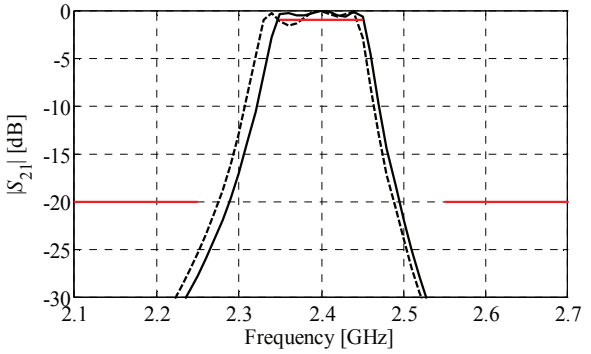

Fig. 14. Coupled-line bandpass filter: responses of the coarse-discretization model $\boldsymbol{R}_{c.2}$ at $\boldsymbol{x}^{(1)}$ (dashed line) and at its optimized design $\boldsymbol{x}^{(2)}$ (solid line), as well as the response of $\boldsymbol{R}_f$ at $\boldsymbol{x}^{(2)}$ (dotted line).

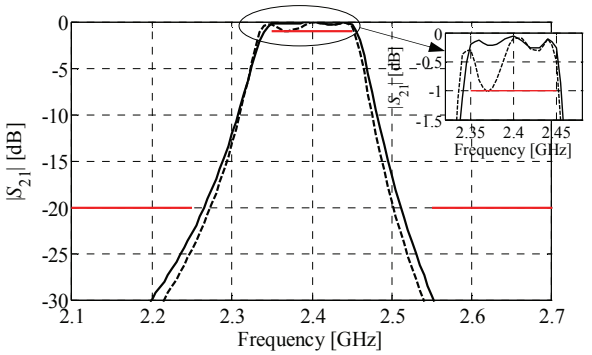

Fig. 15. Coupled-line bandpass filter: responses of the fine-discretization model $\boldsymbol{R}_f$ at $\boldsymbol{x}^{(2)}$ (dashed line) and at the refined final design $\boldsymbol{x}^*$ (solid line); here the original design specifications are shown.

D. Comparison with Direct Optimization

In order to illustrate the computational efficiency of the proposed technique, the fine models for the three filter examples have been directly optimized using the pattern-search algorithm of Section II.A. The results are presented in Table 4. In all cases, the design found by direct search is similar to that obtained using our method (specification errors –2.1 dB, –0.025, and –1.8 dB, respectively). However, the computational cost, depending on the example, is 10 to 20 times higher than that for the technique presented here.

Table 4: Direct fine model optimization results.

Example	CPU Cost	
	$\boldsymbol{R}_f$ Calls	Time
Stacked slotted resonators filter (III.*A*)	120	32 h
HTS filter (III.*B*)	210	179 h
Coupled-line bandpass filter (III.*C*)	133	95 h

IV. CONCLUSION

A simple and robust algorithm for microwave design optimization is proposed that exploits sequential, multi-grid optimization of coarse-discretization EM-simulation-based models and polynomial-approximation-based refinement of the final design. The presented method is easy to implement. It does not need any auxiliary equivalent-circuit model (which is typically used by space mapping) or any modifications of the original structure, such as cutting and inserting the tuning ports necessary by the tuning methodology. It is also computationally efficient, as most of the operations are performed on the coarse-discretization models. Because of its simplicity and versatility, the proposed method can be viewed as a step forward towards making simulation-driven microwave design feasible and computationally tractable.

ACKNOWLEDGMENT

The author thanks Sonnet Software, Inc., Syracuse, NY, for making ***em***™ available. This work was supported in part by the Reykjavik University Development Fund under Grant T09009.

REFERENCES

[1] R.V. Snyder, "Practical aspects of microwave filter development," *IEEE Microwave Magazine*, vol. 8, no. 2, pp. 42-54, Apr. 2007.

[2] A. Bhargava, "Designing circuits using an EM/circuit co-simulation technique," *RF Design*, p. 76, Jan. 2005.

[3] S. Shin and S. Kanamaluru, "Diplexer design using EM and circuit simulation techniques," *IEEE Microwave Magazine*, vol.8, no.2, pp.77-82, Apr. 2007.

[4] N. V. Queipo, R. T. Haftka, W. Shyy, T. Goel, R. Vaidynathan, and P.K. Tucker, "Surrogate-based analysis and optimization," *Progress in Aerospace Sciences*, vol. 41, no. 1, pp. 1-28, Jan. 2005.

[5] A. I. J. Forrester and A. J. Keane, "Recent advances in surrogate-based optimization," *Prog. in Aerospace Sciences*, vol. 45, no. 1-3, pp. 50-79, Jan.-April, 2009.

[6] J. W. Bandler, Q. S. Cheng, S. A. Dakroury, A. S. Mohamed, M. H. Bakr, K. Madsen, and J. Søndergaard, "Space mapping: the state of the art," *IEEE Trans. Microwave Theory Tech.*, vol. 52, no. 1, pp. 337-361, Jan. 2004.

[7] S. Amari, C. LeDrew, and W. Menzel, "Space-mapping optimization of planar coupled-resonator microwave filters," *IEEE Trans. Microwave Theory Tech.*, vol. 54, no. 5, pp. 2153-2159, May 2006.

[8] G. Crevecoeur, L. Dupre, and R. Van de Walle, "Space mapping optimization of the magnetic circuit of electrical machines including local material degradation," *IEEE Trans. Magn.*, vol. 43, no 6, pp. 2609-2611, June 2007.

[9] D. Echeverria and P. W. Hemker, "Space mapping and defect correction," *CMAM The International Mathematical Journal Computational Methods in Applied Mathematics,* vol. 5, no. 2, pp. 107-136, 2005.

[10] S. Koziel, J. W. Bandler, and K. Madsen, "A space mapping framework for engineering optimization: theory and implementation," *IEEE Trans. Microwave Theory Tech.*, vol. 54, no. 10, pp. 3721-3730, Oct. 2006.

[11] S. Koziel, Q. S. Cheng, and J. W. Bandler, "Space mapping," *IEEE Microwave Magazine*, vol. 9, no. 6, pp. 105-122, Dec. 2008.

[12] X. J. Zhang and D. G. Fang, "Using circuit model from layout-level synthesis as coarse model in space mapping and its application in modelling low-temperature ceramic cofired radio frequency circuits," *Microwaves, Antennas & Propagation, IET*, vol. 1, no. 4, pp. 881-886, Aug. 2007.

[13] D. Swanson and G. Macchiarella, "Microwave filter design by synthesis and optimization," *IEEE Microwave Magazine*, vol. 8, no. 2, pp. 55-69, Apr. 2007.

[14] J. C. Rautio, "EM-component-based design of planar circuits," *IEEE Microwave Magazine*, vol. 8, no. 4, pp. 79-90, Aug. 2007.

[15] J. C. Rautio, "Perfectly calibrated internal ports in EM analysis of planar circuits," *IEEE MTT-S Int. Microwave Symp. Dig.*, pp. 1373-1376, June 2008.

[16] S. Koziel, J. Meng, J. W. Bandler, M.H. Bakr, and Q.S. Cheng, "Accelerated microwave design optimization with tuning space mapping," *IEEE Trans. Microwave Theory and Tech.*, vol. 57, no. 2, pp. 383-394, 2009.

[17] Q. S. Cheng, J. W. Bandler, and S. Koziel, "Tuning Space Mapping Optimization Exploiting Embedded Surrogate Elements," *IEEE MTT-S Int. Microwave Symp. Dig*, pp. 1257-1260, 2009.

[18] S. Koziel, J. W. Bandler, and K. Madsen, "Quality assessment of coarse models and surrogates for space mapping optimization," *Optimization and Engineering*, vol. 9, no. 4, pp. 375-391, 2008.

[19] ***em***™ Version 12.54, Sonnet Software, Inc., 2009.

[20] N. M. Alexandrov and R. M. Lewis, "An overview of first-order model management for engineering optimization," *Optimization Eng.*, vol. 2, no. 4, pp. 413-430, Dec. 2001.

[21] C. L. Huang, Y. B. Chen, and C. F. Tasi, "New compact microstrip stacked slotted resonators bandpass filter with transmission zeros using high-permittivity ceramics substrate," *Microwave Opt. Tech. Lett.*, vol. 50, no. 5, pp. 1377-1379, May 2008.

[22] J. W. Bandler, R. M. Biernacki, S. H. Chen, R. H. Hemmers, and K. Madsen, "Electromagnetic optimization exploiting aggressive space mapping," *IEEE Trans. Microwave Theory Tech.*, vol. 43, no.12, pp. 2874-2882, Dec. 1995.

[23] H. M. Lee and C. M. Tsai, "Improved coupled-microstrip filter design using effective even-mode and odd-model characteristic impedances," *IEEE Trans. Microwave Theory Tech.*, vol. 53, no. 9, pp. 2812-2818, Sept. 2005.

[24] FEKO® *User's Manual*, Suite 5.3, EM Software & Systems-S.A. (Pty) Ltd, http://www.feko.info, 2008.

Slawomir Koziel received the M.Sc. and Ph.D. degrees in electronic engineering from Gdansk University of Technology, Poland, in 1995 and 2000, respectively. He also received the M.Sc. degrees in theoretical physics and in mathematics, in 2000 and 2002, respectively, as well as the PhD in mathematics from the University of Gdansk, Poland in 2003. He is currently an Associate Professor with the School of Science and Engineering, Reykjavik University, Iceland. His research interests include CAD and modeling of microwave circuits, surrogate-based optimization, space mapping, circuit theory, analog signal processing, evolutionary computation and numerical analysis.

Transmission through an Arbitrarily Shaped Aperture in a Conducting Plane Separating Air and a Chiral Medium

Ş. Taha İmeci[1], Fikret Altunkılıç[2], Joseph R. Mautz[2] and Ercüment Arvas[2]

[1] Vali İzzetbey Cad.,
KTO Karatay University, Karatay Medresesi Karşısı, Kemaliye Sok. No: 7
42030 Karatay – Konya – TURKEY
tahaimeci@halic.edu.tr

[2] Department of Electrical Engineering and Computer Science
Syracuse University, Syracuse, NY, 13244, USA
faltunki@syr.edu, jrmautz@syr.edu; earvas@syr.edu

Abstract- The analysis of chiral materials has been an important subject in computational electromagnetics. In this paper, the method of moments technique is used to solve the problem of transmission through an arbitrarily shaped aperture separating air and a chiral medium. The aperture is in an infinite PEC (perfect electric conductor) plane. The excitation is assumed to be a plane wave in air. The equivalence principle is used to replace the aperture with a conducting surface with an equivalent magnetic current on each side of it. By enforcing the continuity of the tangential components of the total electric and magnetic fields across the aperture, coupled integral equations are obtained. The aperture has been modeled by triangular patches. The equivalent magnetic currents are approximated by linear combinations of expansion functions. The mixed potential formulation for a homogeneous chiral medium is used to obtain the electric and the magnetic fields produced by these expansion functions. The coefficients of these expansion functions are obtained by using the method of moments to solve the coupled integral equations.

Index Terms- Apertures, chiral media, conductors, moment methods.

I. INTRODUCTION

In this work, an aperture problem is solved using some electromagnetic simulation tools and numerical analysis. More specifically, a numerical technique is used to solve an electromagnetic transmission problem involving a chiral medium. Before the development of fast software and hardware technologies, analytical solutions were possible and popular for solving simple numerical electromagnetic problems. After the new era of computing tools arose, it was possible to do extensive numerical analysis to solve more electromagnetic problems especially those of transmission and/or scattering.

Numerical analysis of chiral materials has been done using a variety of numerical methods, such as the method of moments (MoM) [1], the finite-difference time-domain (FDTD) method [2], the finite element method-boundary element method (FEM-BEM) [3], and the transmission line modeling (TLM) method [4]. In this paper, a MoM formulation has been developed for chiral material and this formulation has been verified for transmission through an aperture by comparing the numerical results with other solutions. In Section II, the constitutive relations and the field of sources in an unbounded chiral medium are discussed. The basic formulation which leads to the detailed formulation in Section III is developed in Section II. Section IV contains numerical results and discussion. Some of the numerical results are compared with results obtained elsewhere. The conclusion and final comments are given in Section V.

II. CHIRAL MEDIA

The constitutive relations for a chiral medium are given in [5] as:

$$\overline{D} = \varepsilon \overline{E} - j\xi \overline{H} \quad (1)$$

$$\overline{B} = \mu \overline{H} + j\xi \overline{E} \quad (2)$$

where ε is the permittivity, μ is the permeability, and ξ is the chirality. These constitutive relations reduce to those for a simple dielectric medium when $\xi = 0$. A chiral material is defined by its constitutive relations (1) and (2). The constitutive relations (1) and (2) completely define the electromagnetic behavior of a chiral material.

The electromagnetic fields must satisfy the Maxwell equations given by

$$\nabla \times \overline{E} = -j\omega \overline{B} - \overline{M} \quad (3)$$

$$\nabla \times \overline{H} = j\omega \overline{D} + \overline{J} \,. \quad (4)$$

The field in a chiral medium is a right-handed field plus a left-handed field. In order to get Maxwell's equations for the right- and left-handed fields and current sources of the wavefield decomposition [1], [5], [6] one can put these constitutive relations into (3) and (4) and get that,

$$\nabla \times \overline{E}_{\pm} = -j\omega \mu_{\pm} \overline{H}_{\pm} - \overline{M}_{\pm} \quad (5)$$

$$\nabla \times \overline{H}_{\pm} = j\omega \varepsilon_{\pm} \overline{E}_{\pm} + \overline{J}_{\pm} \quad (6)$$

Equations (5) and (6) are called the equivalent Maxwell equations for the right-handed and left-handed fields. These equations, and hence their solutions, are very similar to those of sources radiating in an unbounded regular (achiral) medium. The mixed potential formulation [7] is used to obtain the fields of these kinds of sources.

III. 3-D VIEW OF THE PROBLEM AND FORMULATION

Figure 1 shows a plane wave, coming from the direction specified by θ^i and ϕ^i incident upon an arbitrarily shaped aperture in the PEC plane. This plane separates the half-space filled with air (ε_0, μ_0), from that filled with a homogeneous chiral medium (ε_b, μ_b, ξ).

The equivalence principle [8], which is that for an achiral-achiral separation with one of the achiral mediums replaced by the chiral medium, is applied. An equivalent problem is obtained by closing the aperture with a PEC and placing magnetic currents $\pm\overline{M} = \pm\overline{E} \times \hat{z}$ immediately above and below the closed aperture as shown in Fig. 2. Continuity of $\overline{E} \times \hat{z}$ across the aperture is one boundary condition that is satisfied by putting $\overline{M}$ and $-\overline{M}$ in Fig. 2. Another boundary condition that must be satisfied is continuity of $\hat{z} \times \overline{H}$ across the aperture. By image theory, the field of $\overline{M}$ above the PEC plane is that of $2\overline{M}$ in air. Figure 3 is for determining the field of $-\overline{M}$ in the chiral medium.

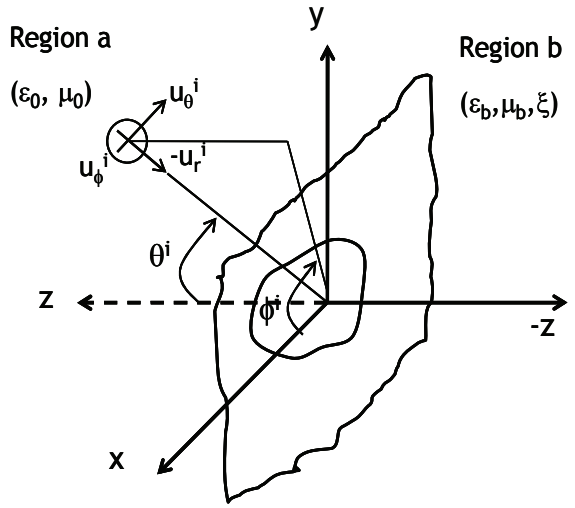

Fig. 1. Three dimensional depiction of the problem.

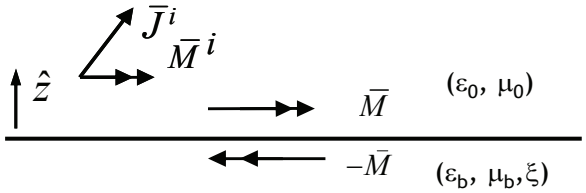

Fig. 2. Equivalence for regions a and b.

below the PEC plane in Fig. 2. If, in Fig. 2, radiation for z > 0 was not restricted to air and radiation for z < 0 was not restricted to the chiral medium, Fig. 2 would be valid for the separation of any two different mediums. In the image principle for a chiral medium, the image of the chiral medium is the chiral medium with the sign of its chirality changed. Therefore, application of the image principle does not result in a hypothetical situation where all space is filled with the same chiral medium. Instead of applying the image principle for a chiral medium, we deal with the infinite PEC plane directly. In order to apply the method of moments, we have to approximate the infinite PEC plane by a finite PEC plane. The finite PEC plane has to be so large that the electric current induced on it is nearly the same as the

electric current that would be induced on the infinite PEC plane. The effect of the finite PEC plane is that of the electric current $\overline{J}$ that flows on it in Fig. 3. Of course, $\overline{J}$ must be such that, on the finite PEC plane, the electric field of the combination of $\overline{J}$ and $-\overline{M}$ has no component tangent to the PEC plane. Because there should be no field in Region a of Fig. 3, the medium in Region a of Fig. 3 is of no consequence. Liberty was taken to put the chiral medium$(\varepsilon_b,\mu_b,\xi)$ in Region a of Fig. 3.

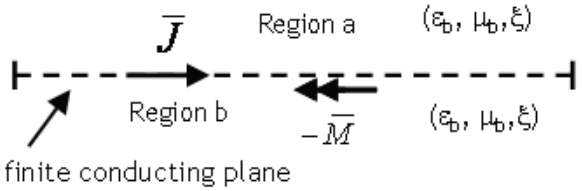

Fig. 3. Finite PEC plane just above $-\overline{M}$.

Now,

$$\overline{E}^{b}_{\tan}(\overline{J},-\overline{M})=0 \tag{7}$$

just above $-\overline{M}$, on the whole finite PEC plane in Fig. 3, and continuity of the tangential magnetic field across the aperture in the original problem of Fig. 1 is expressed as,

$$2\left[\overline{H}^{inc}_{\tan}+\overline{H}^{a}_{\tan}(0,\overline{M})\right]\Big|_{z=0^{+}}=\left[\overline{H}^{b}_{\tan}(\overline{J},-\overline{M})\right]\Big|_{z=0^{-}} \tag{8}$$

over the aperture. The superscript a indicates radiation in all space filled with the medium (ε_0, μ_0) of Region a, and the superscript b indicates radiation in all space filled with the medium $(\varepsilon_b,\mu_b,\xi)$ of Region b. Also, $\overline{H}^{inc}$ is the free-space incident magnetic field. Although the left-hand side of (7) and the right-hand side of (8) are obtained by using the finite PEC plane, the left-hand side of (8) is, in view of application of the method of images, obtained by using the infinite PEC plane.

The left-hand side of (7) and the right-hand side of (8) could not be obtained by using the infinite PEC plane because the usual method of images does not apply to an infinite PEC plane in a chiral medium.

Equations (7) and (8) are solved for $\overline{J}$ and $\overline{M}$ by using the method of moments.

$$\overline{J}(\overline{r})=\sum_{n=1}^{N'} I_n\overline{f}_n(\overline{r}) \tag{9}$$

$$\overline{M}(\overline{r})=\sum_{n=1}^{N} V_n\overline{f}_n(\overline{r}) \tag{10}$$

where $\{\overline{f}_n(\overline{r}),\ n=1,2,...\}$ are the RWG [9] expansion functions, I_n and V_n are unknown coefficients to be calculated, N is the number of expansion functions in the aperture, and N′ = is the number of expansion functions on the whole finite PEC plane. RWG stands for the last names of the authors of [9].

The only difference between the equivalence principle where one or both regions are chiral and the equivalence principle where both regions are achiral is that in the equivalence principle where one or both regions are chiral, the equivalent currents radiate in the chiral region or regions. In the manuscript, the equivalence principle is merely applied; its derivation and explanation appears in [8].

Our MoM approach is not with a dyadic Green's function but with the mixed potential formulation. The dyadic Green's function approach for obtaining the electric field of an electric current involves an integral whose integrand contains the Green's function and its second order derivative. This integral is difficult to evaluate because its integrand is singular. In the mixed potential approach [7], there is an integral whose integrand contains the Green's function and there is the gradient of an integral whose integrand contains the Green's function. By manipulation, one can trade the gradient operation on the latter integral for the surface divergence operation on the MoM testing function and arrive at a formulation that is more suitable for computation than the dyadic Green's formulation.

It is difficult to obtain a good estimate of the error incurred by the use of a finite ground plane. We did a crude convergence study where we began with a small ground plane and made it larger and larger until the magnitude of the electric current near its edges was less than 11% of its maximum value in the vicinity of the magnetic current.

IV. NUMERICAL RESULTS

A. Square Aperture

Figure 4 shows a square conducting plate of side length 2λ. At its center is a square aperture of side length L=0.25λ. The plate and the aperture are modeled by triangular patches, with a finer mesh around the aperture. Figures 5 – 8 show currents $|M_y|$ and $|J_x|$ due to a normally incident plane wave traveling in the negative z-direction. The electric field of this plane wave is

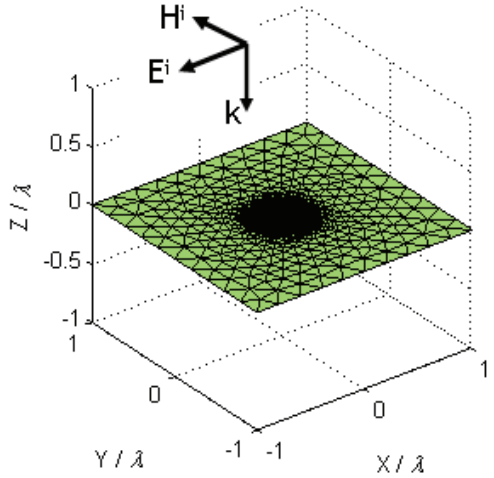

Fig. 4. Square aperture in a finite conducting plane.

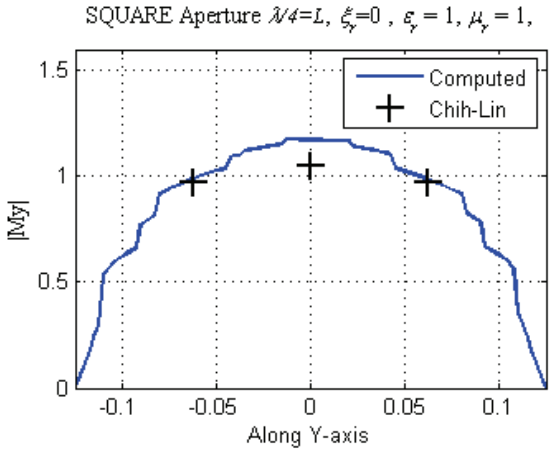

Fig. 5. Equivalent magnetic current when ξ=0.

$\overline{E}^{inc} = -\overline{a}_x E^{inc} e^{jk_o z}$. Figures 5 and 6 are for the special case where the chiral material is replaced by air (ε_0, μ_0). This case was considered to compare our results with those of [10]. In Figs. 5 – 10 the units along each horizontal axis are those of the ratio of length to wavelength. The units of M_y are those of the incident electric field and the units of J_x are those of the incident magnetic field. The phase of M_y is plotted in degrees. Our computed results shown in Figs. 5 and 6 are in good agreement with [10].

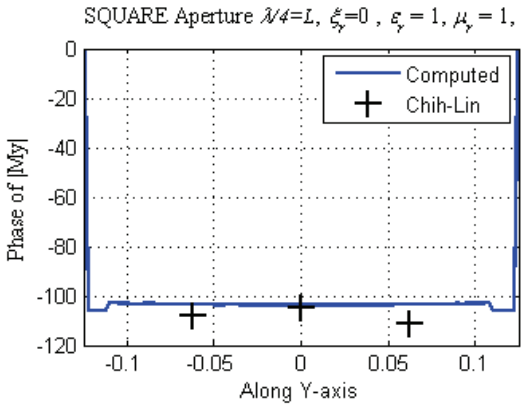

Fig. 6. Phase of equivalent magnetic current when ξ=0.

In [10], only 32 triangles were used in the aperture region while we have 241 triangles, and finer mesh around the edges. The finer mesh, easily obtainable with computational facilities of our day, should give better accuracy than that in [10]. For achiral media, the present approach still uses the finite PEC plane for radiation in the Region b half space whereas the approach in [10] uses an infinite PEC plane. For the achiral cases, agreement of results of the present approach with results in [10] therefore shows that, at least for these achiral cases, the finite PEC plane was large enough to be a good approximation of an infinite PEC plane. A 2254×2254 matrix was used. The computation time for a 4GHz processor machine in MATLAB was 16 minutes. Figure 7 shows the effect of chirality on the equivalent magnetic current in the aperture, and Fig. 8 shows J_x, the x-component of J, on the finite PEC plane. In Figs. 7 and 8, $\varepsilon_r = 2$, $\mu_r = 1$ and $\xi_r = \xi / \sqrt{\mu\varepsilon}$ where ε_r, μ_r and ξ_r are, respectively, relative permittivity, permeability and chirality of Region b. No results for comparison with the curves of Figs. 7 and 8 were available in the literature. We observe that as chirality gets smaller, the results in Fig. 7 seem to approach those in Fig. 5 despite the difference in

permittivities. In Fig. 8, $\eta_0 = \sqrt{\mu_0 / \varepsilon_0}$. It is noted that the current in Fig. 8 is very small as one moves away from the aperture by only half a wavelength. This is justification for approximating an infinite PEC plane with one that is a square of side length only 2λ.

Co-polarized and cross-polarized bistatic radar cross sections (RCS) are shown in Figs. 9 and 10. The co-polarized RCS is called $\sigma_{\theta\theta}$ because the incident electric field is θ-polarized and only the θ-component of the diffracted electric field is received. The RCS is a measure of the square of the magnitude of the diffracted field in Region a. The diffracted electric field is the electric field due to the aperture. That is, the diffracted electric field is the electric field that exists when the aperture is in the PEC screen minus the electric field that would exist if the aperture were not in the PEC screen. The cross-polarized RCS is called $\sigma_{\phi\theta}$ because the incident electric field is θ-polarized and only the ϕ-component of the diffracted electric field is received. For both Figs. 9 and 10, the excitation is a normally incident (θ^{inc}=0) plane wave with its electric field polarized in the –x-direction. In Fig. 9, the θ-component of the diffracted electric field is received at θ in the ϕ=0 plane. In Fig.10, the ϕ-component of the diffracted electric field is received at θ in the ϕ=0 plane. The ϕ component in the ϕ=0 plane is the y component in the xz plane. All figures which have "along Y-axis" at the bottom are versus y / λ along the y-axis.

The internal field has been calculated along the *z*-axis, from the center of the aperture at *z*/λ = 0 down to *z*/λ = −1. The side length of the square aperture is L = λ/4 and the side length of the conducting plane is 2λ. The excitation is again a normally incident plane wave whose electric field is $\bar{E}^{inc} = -\bar{a}_x E^{inc} e^{jk_o z}$. Computed values are the magnitudes of $-E_x / E^{inc}$ and E_y / E^{inc} and their phases with and without chirality. In Fig. 11 where the chirality is zero, $\left|E_x / E^{inc}\right|$ approaches $\left|M_y / E^{inc}\right|$ in the aperture in Fig. 5. In Fig. 12 where the chirality is also zero, the phase of

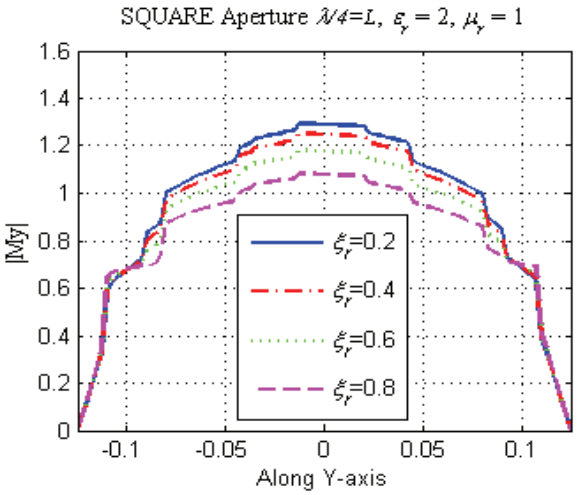

Fig. 7. Equivalent magnetic current with different chiralities.

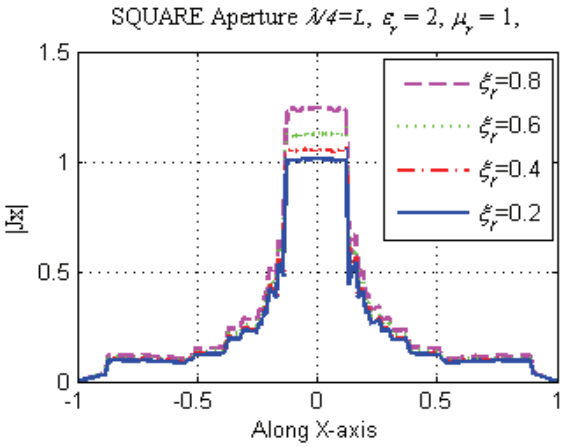

Fig. 8. Equivalent electric current with different chiralities.

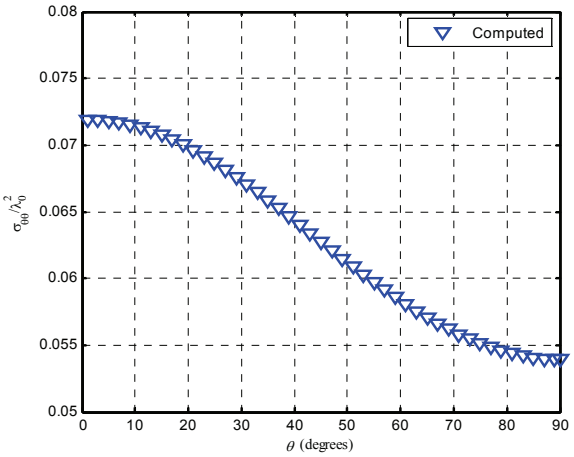

Fig. 9. $\sigma_{\theta\theta}$ of square aperture with ξ_r =0.4, ε_r = 2, μ_r =1.

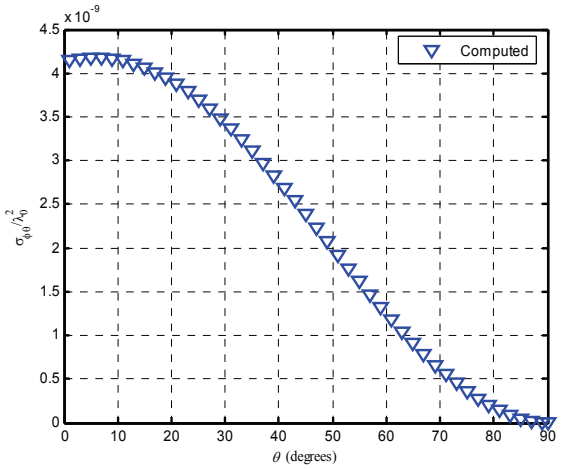

Fig. 10. $\sigma_{\phi\theta}$ of square aperture with ξ_r=0.4, $\varepsilon_r = 2$, μ_r=1.

$-E_x / E^{inc}$ approaches the phase of M_y / E^{inc} in the aperture in Fig. 6. In Fig. 13, $\left|E_y / E^{inc}\right|$ is well below $\left|E_x / E^{inc}\right|$ as expected. Figures 14 and 15 show $\left|E_x / E^{inc}\right|$ and $\left|E_y / E^{inc}\right|$ when ξ_r=0.5.

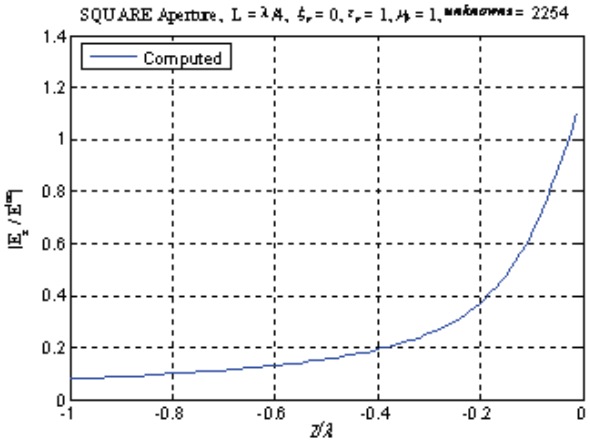

Fig. 11. $\left|E_x / E^{inc}\right|$ in Region b behind aperture when ξ_r=0.

Figure 16 shows the transmission cross section patterns, τ_θ in the x = 0 plane, and τ_ϕ in the y = 0 plane where,

$$\tau_\theta = 2\pi r^2 \left|\eta_0 H_\theta / E^{inc}\right|^2 \qquad (11)$$

$$\tau_\phi = 2\pi r^2 \left|\eta_0 H_\phi / E^{inc}\right|^2 \qquad (12)$$

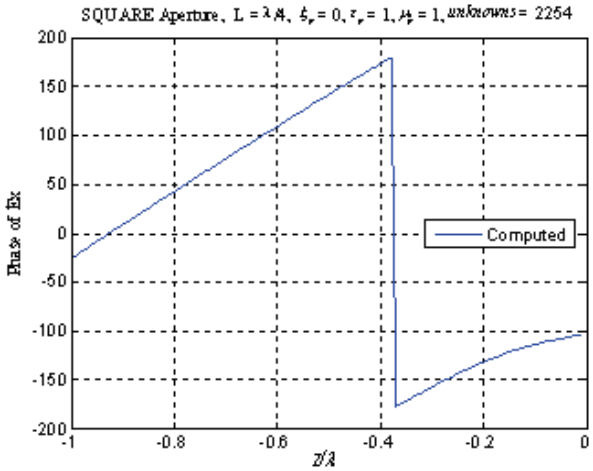

Fig. 12. Phase of $\bar{E}_x$ in Region b behind aperture when ξ_r=0.

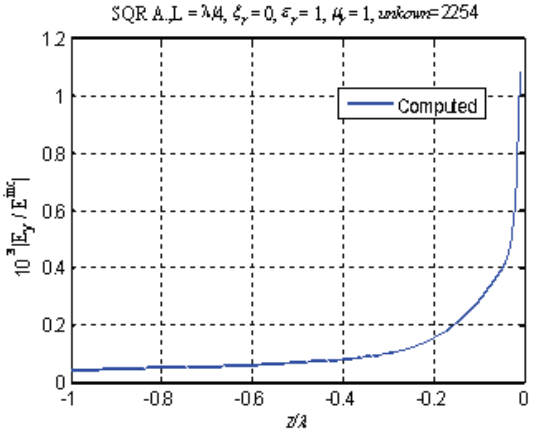

Fig. 13. $\left|E_y / E^{inc}\right|$ in Region b behind aperture when ξ_r=0.

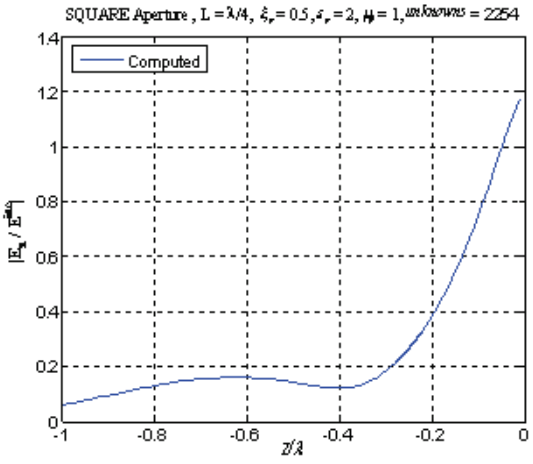

Fig. 14. $\left|E_x / E^{inc}\right|$ in Region b behind aperture when ξ_r=0.5.

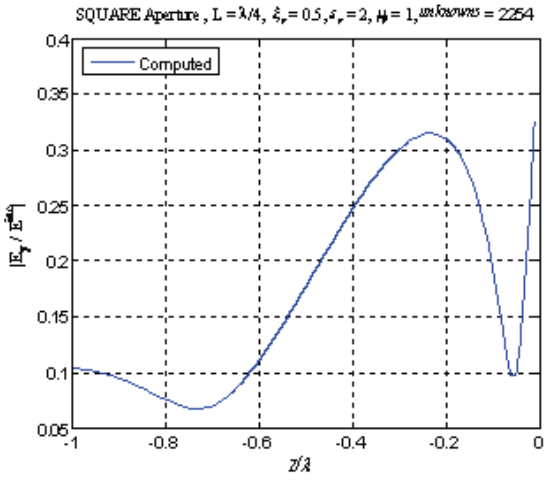

Fig. 15. $\left|E_y / E^{inc}\right|$ in Region b behind aperture when ξ_r =0.5.

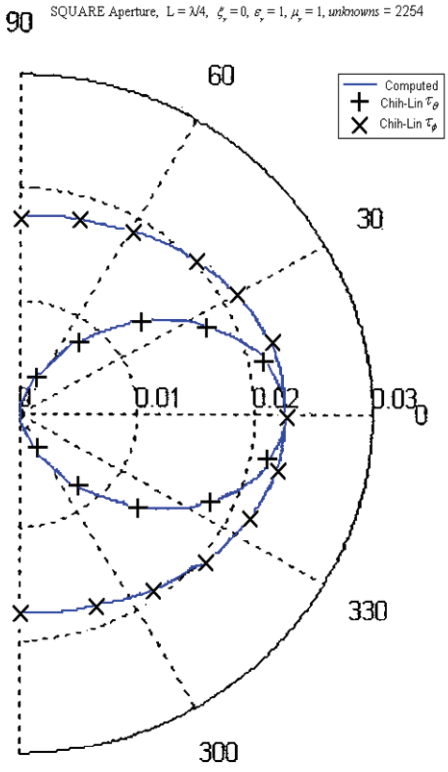

Fig. 16. Transmission cross section patterns when ξ_r =0.

These patterns are in good agreement with those in [10]. Direct comparison with patterns shown in [11] is not possible because all patterns shown in [11] are for the dual problem of scattering by a rectangular plate. Figures 17 and 18 show the patterns with various chiralities. Table 1 shows the transmission coefficient comparison results, which agree with those in [10], and also shows the change with various chiralities. The transmission coefficient is P_{trans} /P_{inc}. P_{trans} is the transmitted power going through the aperture. P_{inc} is the incident power in free space on the aperture.

$$P_{trans} = -\frac{1}{2}\mathrm{Re}\int_{apert.}\left(\overline{E}\times\overline{H}^{*}\right)\cdot\hat{z}\,ds \tag{13}$$

$$P_{inc} = \eta\left|\overline{H}^{inc}\right|^{2} S\cos\theta^{inc} \tag{14}$$

where S is the area of the aperture.

If the PEC plane was really finite, then, very far into the chiral material, the PEC plane would have no effect. As a result, only the effect of the incident field on the interface between air and the chiral material would be seen. This effect would mask any transmission cross section. However, because the left-hand side of (8) is obtained by using the infinite PEC plane, the PEC plane does not look small very far into the chiral material so that transmission cross sections can be obtained. Chiral materials are also used to reduce the radar cross section [12],[13].

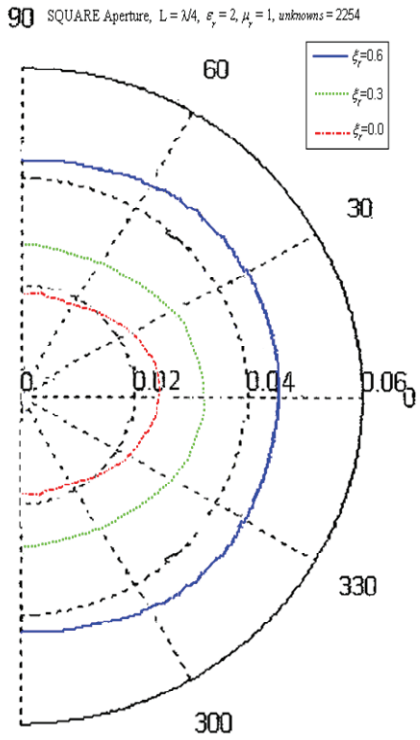

Fig. 17. Transmission cross section pattern (τ_ϕ) with various chiralities.

Table 1: Transmission coefficient for square aperture.

SQUARE APERT. W=L=λ/4	CHIH LIN I	COMPTD. (ξ_r=0)	COMPTD. (ξ_r=0.3)	COMPTD. (ξ_r=0.6)
APERT. AREA	0.0625 (λ^2)	0.0625 (λ^2)	0.0625 (λ^2)	0.0625 (λ^2)
TRANS. COEFF.	0.21483	0.21228	0.33157	0.41391
TRANS. AREA	0.01342 (λ^2)	0.01326 (λ^2)	0.02072 (λ^2)	0.02586 (λ^2)

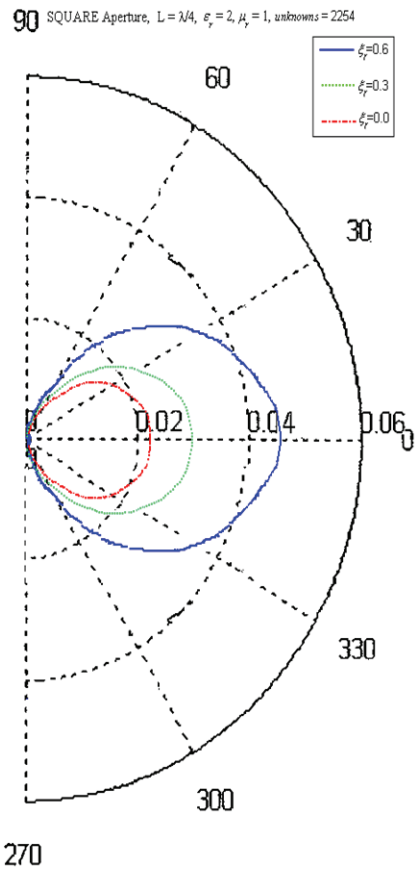

Fig. 18. Transmission cross section pattern (τ_θ) with various chiralities.

B. Slot Aperture

As a second check, an aperture which is a thin slot is meshed. The mesh starts fine and gets coarser near the edges of the finite conducting plane. The excitation is a normally incident unit plane wave traveling in the $-z$ direction. The mesh is finer than that for the square aperture because of the thin width (W = λ/20) shape. This time, 3972 unknowns took 23 minutes on the same machine mentioned previously in Figs. 20 – 28, where the units along each horizontal axis are those of the ratio of length to wavelength, the units of M_y are those of the incident electric field and the phase of M_y is plotted in degrees. Three different slot lengths are considered. The width is always λ/20, but the lengths are λ/4, λ/2, and λ. In the case of the length λ/2, the magnetic current is large because of a resonance. When the chirality is equal to zero, the magnetic current magnitude and phase agree with those in [10] and [14] in all cases. Table 2, for which $\varepsilon_r = \mu_r = 1$, gives transmission coefficients for ξ =0, 0.3 and 0.6. In Table 2, the computed transmission coefficients for ξ_r =0 compare favorably with the transmission coefficients in [10].

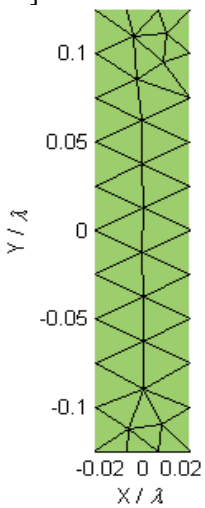

Fig. 19. Slot with W = λ/20 and L = λ/4.

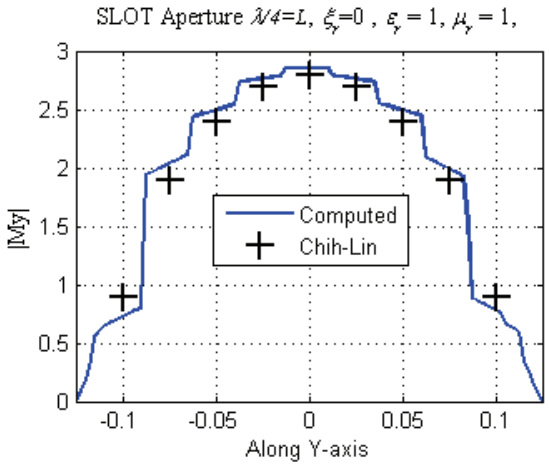

Fig. 20. Magnetic current comparison for slot aperture of W = λ/20 and L = λ/4.

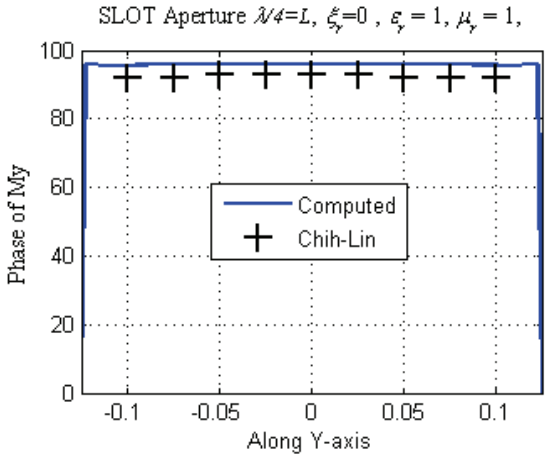

Fig. 21. Phase comparison for slot aperture of L = λ/4.

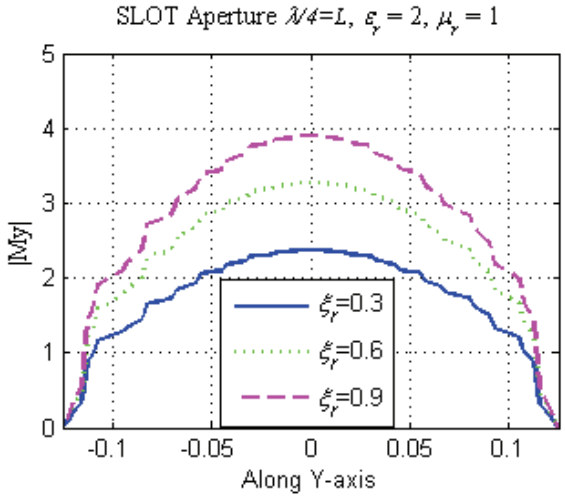

Fig. 22. Magnetic current with different chirality values.

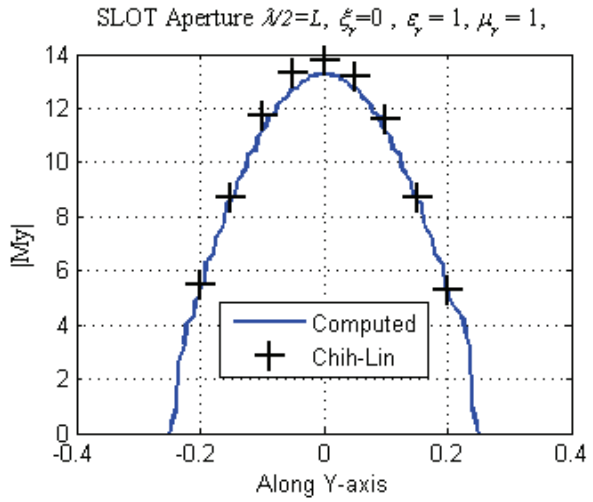

Fig. 23. Magnetic current comparison for slot aperture of W = λ/20 and L = λ/2.

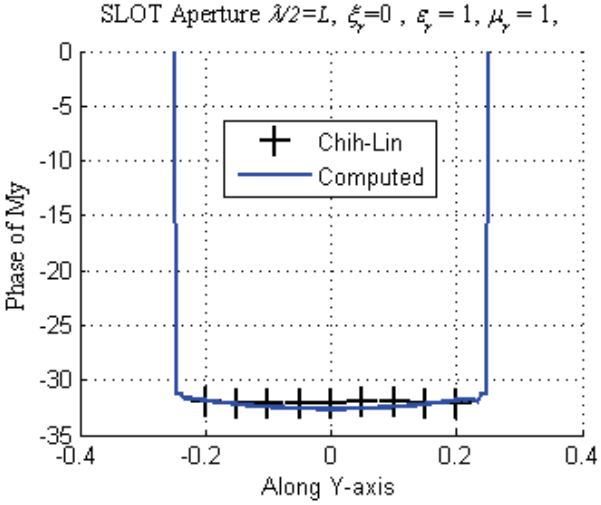

Fig. 24. Phase comparison for slot aperture of L = λ/2.

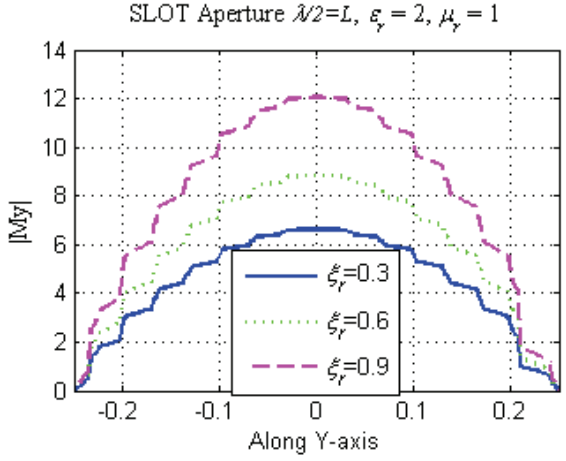

Fig. 25.Magnetic current with different chirality values.

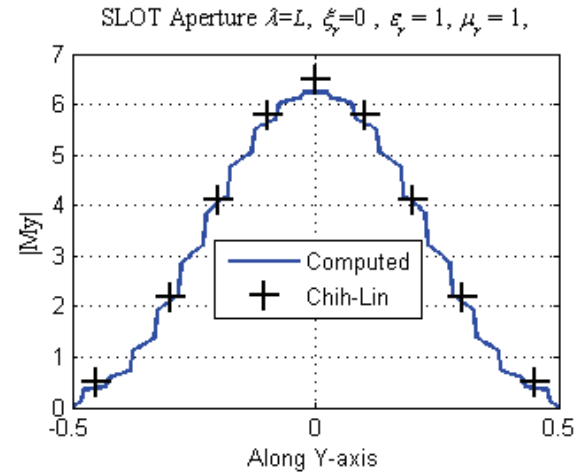

Fig. 26. Mag. current comparison for slot aperture of L=λ.

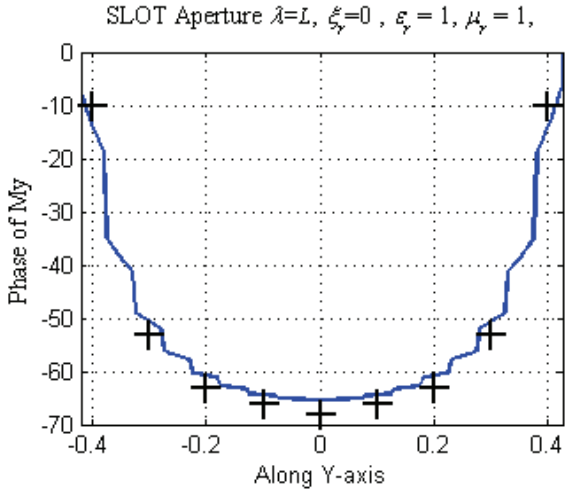

Fig. 27. Phase comparison for slot aperture of L = λ.

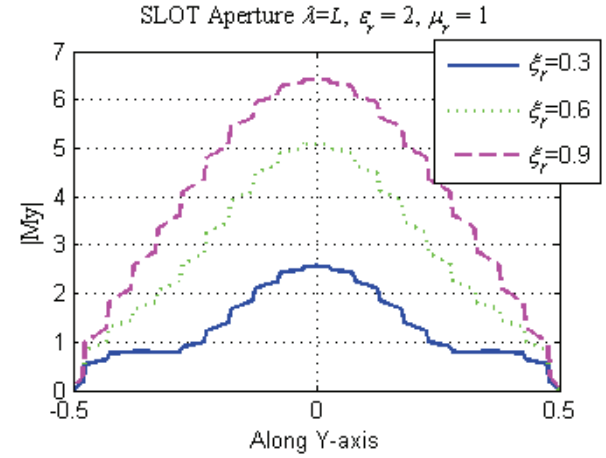

Fig. 28. Magnetic current with different chirality values.

Table 2: Transmission coefficent for slot aperture.

SLOT APERT. W=λ/20		CHIH LIN I [10]	COMP UTED ξ_r=0	COMP UTED ξ_r=0.3	COMP UTED ξ_r=0.6
L=λ/4	AP. AREA	0.0125 (λ²)	0.0125 (λ²)	0.0125 (λ²)	0.0125 (λ²)
	T. COEF	0.179	0.181	0.273	0.395
	T. AREA	0.00224 (λ²)	0.00226 (λ²)	0.00341 (λ²)	0.00494 (λ²)
L=λ/2	AP. AREA	0.025 (λ²)	0.025 (λ²)	0.025 (λ²)	0.025 (λ²)
	T. COEF	8.182	8.131	13.15	19.95
	T. AREA	0.20457 (λ²)	0.20329 (λ²)	0.32894 (λ²)	0.49883 (λ²)
L=λ	AP. AREA	0.05 (λ²)	0.05 (λ²)	0.05 (λ²)	0.05 (λ²)
	T. COEF	1.516	1.518	1.963	2.198
	T. AREA	0.07558(λ²)	0.07559 (λ²)	0.09801 (λ²)	0.10999 (λ²)

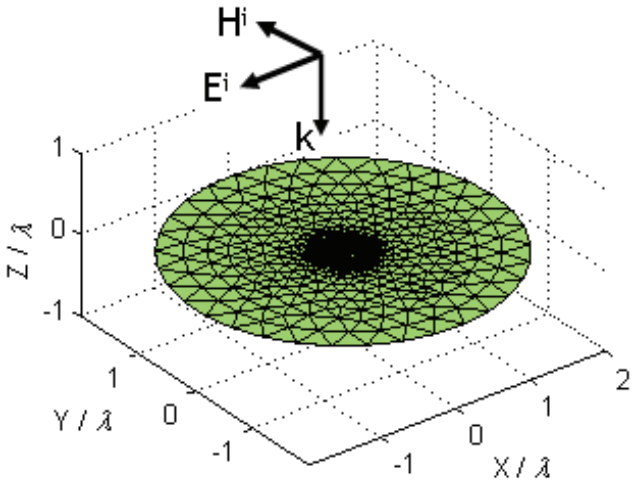

Fig. 29. Finite conducting plane with 2267 unknowns.

C. Circular Aperture

As a third check, a circular mesh is applied to a circular aperture. As it is seen in Fig. 29, the mesh

is fine at the edge of the aperture and is coarse at the end of the finite conducting plane. The incident

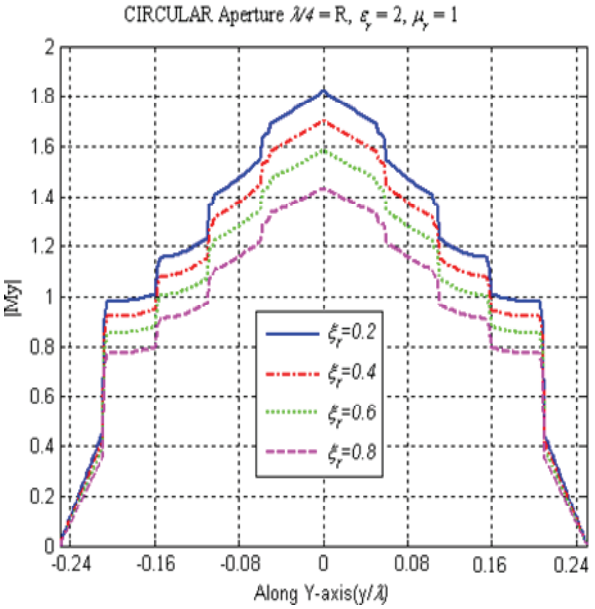

Fig. 30. Magnetic current with different chirality values.

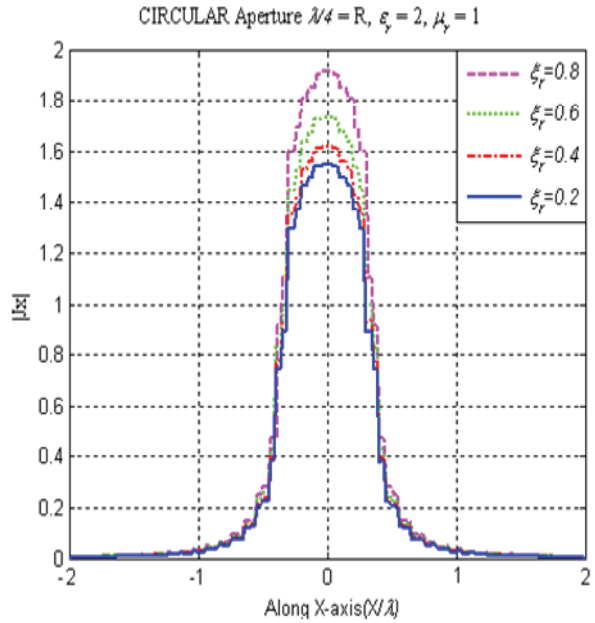

Fig. 31. Electric current with different chirality values.

field is again a normally incident unit plane wave traveling in the $-z$ direction. The radius of the aperture is R=λ/4. The mesh size is close to that of the square aperture. This time, 3267 unknowns took 19 minutes on the same machine mentioned previously. When the chirality is equal to zero, the maximum value of the magnetic current agrees with that in [10]. In Figs. 30 and 31, the dominant components of the equivalent electric and the magnetic currents are plotted for various chiralities. The magnetic current decreases with increasing chirality as for the square aperture. Again chirality affects the current at the center of the aperture more than that at the edges.

V. CONCLUSION

In this work, the method of moments technique is used to solve the problem of transmission through an arbitrarily shaped aperture in a perfectly conducting plane separating air and a chiral medium. Excitation is assumed to be a plane wave. The equivalence principle is used to replace the aperture with a conducting surface with an equivalent magnetic current on each side of it. By enforcing the continuity of the tangential components of the total electric and magnetic fields across the aperture, coupled integral equations are obtained. Triangular patches have been used to model the current in the aperture and on the conductor. The equivalent magnetic currents are approximated by linear combinations of expansion functions. The mixed potential formulation for a homogeneous chiral medium is used to obtain the electric and the magnetic fields produced by these expansion functions. In the mixed potential formulation, the expression for the electric field of an electric current contains the electric scalar potential as well as the magnetic vector potential. The coefficients of these expansion functions are obtained by using the method of moments to solve the coupled integral equations.

ACKNOWLEDGMENT

The authors would like to thank S. Arvas, T. Yemliha and D. Worasawate for providing the meshing programs and the MoM codes.

REFERENCES

[1] D. Worasawate, J. R. Mautz., and E. Arvas, "Electromagnetic scattering from an arbitrarily shaped three-dimensional homogeneous chiral Body," *IEEE Trans. Antennas Propagat.*, vol. 51, pp. 1077–1084, May 2003.

[2] V. Demir, A. Z. Elsherbeni, and E. Arvas, "FDTD formulation for dispersive chiral media using the Z transform method," *IEEE Trans. Antennas Propagat*., vol. 53, pp. 3374–3384, Oct. 2005.

[3] F. Bilotti, A. Toscano, and L. Vegni, "FEM-BEM formulation for analysis of cavity-backed patch antennas on chiral substrates," *IEEE Trans*. *Antennas Propagat*., vol. 51, pp. 306-311, Feb. 2003.

[4] C. Christopoulos, J. Paul, and D. W. P. Thomas, "Simulation of EM wave propagation in magnetoelectric media using TLM," *Int. J. Numer. Model*., vol. 14, pp. 493–505, 2001.

[5] D. Worasawate, "Electromagnetic scattering from an arbitrarily shaped three-dimensional chiral body," *Ph.D. dissertation,* Syracuse University, 2002.

[6] I. V. Lindell, A. H. Sihvola, S. A. Tretyakov, and A. J. Viitanen, *Electromagnetic Waves in Chiral and Bi-Isotropic Media*, Artech House, 1994.

[7] K. A. Michalski, "The mixed-potential electric field integral equation (EFIE) for objects in layered media," *AEU,* vol. 39, pp. 317–322, Sept-Oct. 1985.

[8] R. F. Harrington, *Time-Harmonic Electromagnetic Fields*, New York: McGraw-Hill, 1961

[9] S. M. Rao, D. R. Wilton, and A. W. Glisson, "Electromagnetic scattering by surfaces of arbitrary shape," *IEEE Trans. Antennas Propagat*., vol. AP-30, pp. 409–418, May 1982.

[10] C. -L. I and R. F. Harrington, "Electromagnetic transmission through an aperture of arbitrary shape in a conducting screen," *Technical Report No. 16,* Syracuse University, April 1982.

[11] K. Hongo and H. Serizawa, "Diffraction of electromagnetic plane wave by a rectangular plate and a rectangular hole in the conducting plate," *IEEE Trans*. *Antennas Propagat*., vol. 47, pp. 1029–1041, 1999.

[12] D. L. Jaggard and N. Engheta, "Chirosorb™ as an invisible medium," *Electronics Letters,* vol. 25, no. 3, pp. 173-174, Feb. 1989.

[13] R. Sharma and N. Balakrishnan, "Scattering of electromagnetic waves from arbitrary shaped bodies coated with a chiral material," *Smart Materials and Structures,* vol. 7, no. 6, pp. 851-866, Dec. 1998.

[14] R.F. Harrington and J.R. Mautz, "Electromagnetic transmission through an aperture in a conducting plane," *AEU*, vol. 31, pp. 81–87, 1977.

Ş. Taha İmeci received the B.Sc. degree in Electronics and Communications Engineering from Yildiz Technical University, Istanbul, Turkey in 1993, and the M.S.E.E. and Ph.D. Degrees from Syracuse University, Syracuse, NY in 2001 and 2007, respectively.

He was with Anaren Microwave Inc., East Syracuse, NY from 2000 to 2002, and Herley Farmingdale, New York from 2002 to 2003, and PPC, Syracuse, NY from 2003 to 2005, and Sonnet Software Inc., Liverpool, NY from 2006 to 2007. He was a teaching assistant in the Department of Electrical Engineering and Computer Science at Syracuse University from 2005 to 2006. He has authored an abstract, "A project-based graduate antenna course," *2003 IEEE International AP Symp., and USNC/CNC/URSI North American Radio Science Mtng*, June 22–27, Columbus, OH, p. 454, URSI Digest., and five conference papers, "A wide band 3dB Hybrid/Hopfer Coupler" at *Antem/URSI 2004,* July 20–23 Ottawa-Canada, "Electromagnetic transmission through an aperture in a conducting plane between air and a chiral medium" *Aces2008, March 30th-April 4th, Niagara Falls-Canada,* "Circularly Polarized Microstrip Patch Antenna with Slits", "20 dB Hybrid Stripline Coupler", "Corners Truncated Microstrip Patch Antenna", at *Aces2010 ,April 26th-April29th Tampere, Finland,* and he has authored 5 conference papers in Turkey.

Dr. Imeci is a member of TMMOB, Chamber of Electrical Engineers in Turkey since 1993, and the Applied Computational Electromagnetics Society (ACES).

Fikret Altunkilic was born in Ordu, Turkey in 1970. He received the B.Sc. degree in Electronics and Communications Engineering from Istanbul Technical University, Istanbul, Turkey in 1996, and the M.S.E.E. and Ph.D. Degrees from Syracuse University, Syracuse, NY in 2003 and 2007, respectively. He is presently with Skyworks Solutions, Woburn, MA.

Joseph R. Mautz (S'66-M'67-SM'75-F'05-LF'05) was born in Syracuse, NY in 1939. He received the B.S., M.S. and PhD. Degrees in electrical engineering from Syracuse University, Syracuse, NY in 1961, 1965, and 1969 respectively.

Until July 1993, he was a Research Associate in the Department of Electrical and Computer Engineering of Syracuse University working on radiation and scattering problems. He is presently an adjunct professor in the Electrical Engineering and Computer Science Department at the same University. His primary fields of interest are electromagnetic theory and applied mathematics. He is a member of the Applied Computational Electromagnetics Society (ACES).

Ercüment Arvas (M'85-SM'89-F'03) received the B.S. and M.S. degrees from the Middle East Technical University, Ankara, Turkey in 1976 and 1979, respectively, and the Ph.D. degree from Syracuse University, Syracuse, NY in 1983, all in electrical engineering.

From 1984 to 1987, he was with the Electrical Engineering Department, Rochester Institute of Technology, Rochester, NY. In 1987, he joined the Electrical Engineering and Computer Science Department at Syracuse University where he is currently a Professor in the Electrical Engineering and Computer Science Department. His research and teaching interests are in electromagnetic scattering and microwave devices.

Prof. Arvas is a member of the Applied Computational Electromagnetics Society (ACES).

Analysis of the Shielding Effectiveness of Metallic Enclosures Excited by Internal Sources Through an Efficient Method of Moment Approach

Rodolfo Araneo and Giampiero Lovat

Department of Electrical Engineering
"Sapienza" University of Rome, Via Eudossiana 18, 00184 Roma, Italy
rodolfo.araneo@uniroma1.it, giampiero.lovat@uniroma1.it

***Abstract*—** The shielding effectiveness of rectangular metallic enclosures having thin or thick apertures in one of their walls and possibly loaded with conducting bodies is studied in detail for internal electromagnetic sources consisting of electric or magnetic dipoles. The analysis is performed through an efficient integral-equation formulation based on the Method of Moments, which makes use of several numerical tools (acceleration of the enclosure Green's function evaluation, its interpolation, possible use of entire-domain basis functions, etc...) and physically-based approximations, critically discussed. Several cases are studied and comparisons with results obtained through different full-wave commercial software confirm the accuracy of the proposed approach and its superior performance in terms of computational time and memory storage.

***Index Terms*—** Shielding effectiveness (SE), enclosures, apertures, method of moments (MoM).

I. INTRODUCTION

The analysis of the interaction between an electromagnetic (EM) field and a metallic enclosure is a classical problem in EM shielding. The metallic cavity is usually adopted to shield the interior components from external EM radiators or vice versa, to protect the external environment from the radiation caused by interior EM sources. In any case, the role of the metallic enclosure is that of reducing the EM interference between the inner and the outer world. In this connection, the most important coupling mechanism occurs through the unavoidable presence of apertures on the enclosure walls (which are necessary for many practical purposes) [1].

A metallic enclosure behaves effectively as a resonant EM system, i.e., close to certain characteristic (resonant) frequencies the field amplitude can become very large (ideally infinite for perfectly conducting (PEC) walls). In the presence of apertures, the structure still remains resonant although the resonant frequencies can be shifted and the quality factor reduced (because of radiation losses through the apertures). In any case, at such resonant frequencies, the EM interference is maximum and the shielding effectiveness (SE) of the system dramatically deteriorates. The possible presence of internal loads is another crucial factor that influences the value of the resonant frequencies and the spatial distribution of the field [2]. Finally, the SE depends also on the considered EM source; the latter is usually taken as an impinging uniform plane wave, but, especially if radiation from the interior of the cavity is considered, it could be an electric or a magnetic finite source (e.g., a short-wire or a small-loop antenna) [3].

All these issues call for an efficient and reliable numerical tool for the EM analysis and many numerical techniques have been applied to this classical problem, e.g., analytical formulations [4-6], finite-element [7], mode-matching [8], method-of-moments [9-11], finite-difference-time-domain [12-14], and hybrid [15] approaches.

In this work, we adopt a standard integral-equation (IE) approach for the analysis of metallic enclosures with apertures of arbitrary shape and thickness and possibly loaded with 2-D or 3-D metallic objects. Contrarily to most of the studies (which assume an external plane-wave excitation), we consider here both electric and magnetic dipoles with arbitrary orientation as sources of the incident EM field. In fact, dipoles can represent

practical sources such as short-linear or small-loop antennas. The problem is solved through a mixed-potential formulation of the Method of Moments (MoM). Several numerical tools (such as acceleration of the enclosure Green's function (GF) evaluation, its interpolation, use of different basis functions) and physically-based approximations are introduced to increase the efficiency of the formulation. Finally, the results are compared with those obtained through different full-wave commercial software thus showing the accuracy of the proposed approach and its superior performance.

II. ELECTROMAGNETIC PROBLEM FORMULATION

The EM problem under analysis is sketched in Fig. 1, together with the adopted reference system and the involved geometrical parameters. A rectangular metallic cavity with PEC walls and dimensions $\ell_x \times \ell_y \times \ell_z$ is excited by either an electric or a magnetic dipole of unit amplitude and directed along the direction $\mathbf{u}_d$. The enclosure walls may have a finite thickness t, and one of them (e.g., that located at the plane $z = l_z$) may have one or more apertures of arbitrary shape. Finally, the enclosure can also contain PEC objects of arbitrary shape.

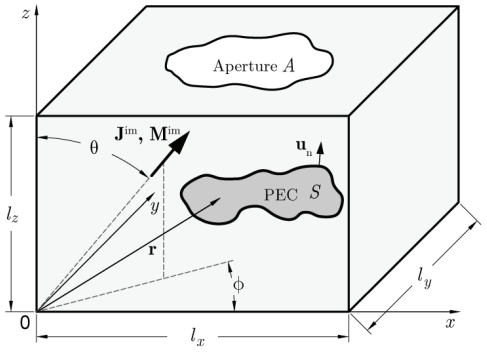

Fig. 1. Metallic rectangular enclosure (with an aperture on one of its walls and loaded with a conducting object) excited by arbitrarily directed electric and magnetic dipoles. The adopted reference system and the involved geometrical parameters are also shown.

In the absence of loading, the incident electric field $\mathbf{E}^{\text{inc}}$ is that radiated in free-space by the impressed dipole sources and it corresponds to a suitable combination (depending on the orientation of the dipoles) of the components of the free-space dyadic electric GFs ($\underline{\mathbf{G}}^{\text{fs}}_{\text{E,J/M}}$) (the subscripts J or M indicate an electric or a magnetic source, respectively). The electric shielding effectiveness SE_E of the enclosure at a given point $\mathbf{r}$ is thus defined as

$$\text{SE}_E = 20\log\frac{\left|\mathbf{E}^{\text{inc}}(\mathbf{r})\right|}{\left|\mathbf{E}(\mathbf{r})\right|} \tag{1}$$

where $\mathbf{E}(\mathbf{r})$ is the electric field at $\mathbf{r}$ due to the radiating dipole sources in the presence of the enclosure, apertures, and conducting objects.

III. INTEGRAL-EQUATION APPROACH

The set of IEs which solve the problem can be derived through a customary application of the equivalence principle [1], as illustrated in Fig. 2: first, for finite-thickness walls, both interfaces of the aperture in $z = l_z$ (section A_i) and $z = l_z + t$ (section A_e) are short-circuited and equivalent magnetic current densities $\mathbf{M}_\text{i}$ and $\mathbf{M}_\text{e}$ are introduced on them. Next, an equivalent electric current density $\mathbf{J}$ is introduced over the surface S of the PEC load (which is then removed). The problem is thus decomposed into three-coupled problems: the metallic enclosure (region 1), the closed short-circuited aperture (region 2), and the external region (region 3).

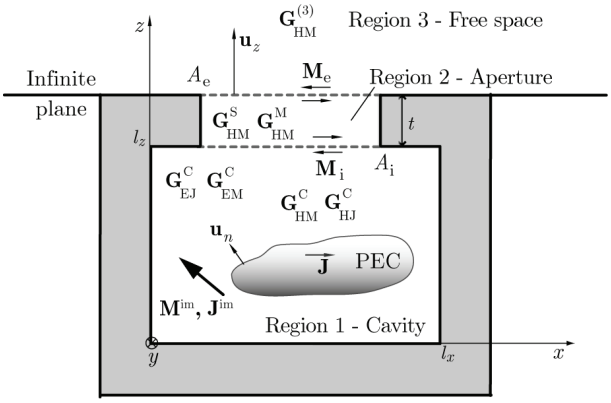

Fig. 2. Aperture in the thick conducting wall of the metallic enclosure and application of the equivalence principle.

By enforcing the boundary conditions at the sections A_i and A_e we have

$$\mathbf{u}_z \times \left[\mathbf{H}^{sc}(\mathbf{r}) + \mathbf{H}^{-}(\mathbf{r}) \right] = \mathbf{u}_z \times \mathbf{H}^{+}(\mathbf{r}) \qquad \mathbf{r} \in A_i \quad (2a)$$

$$\mathbf{u}_z \times \mathbf{H}^{-}(\mathbf{r}) = \mathbf{u}_z \times \mathbf{H}^{+}(\mathbf{r}) \qquad \mathbf{r} \in A_e, \quad (2b)$$

where $\mathbf{H}^{\pm}$ are the fields produced by $\mathbf{M}_{i,e}$ and the $+/-$ superscripts indicate evaluation just above and below the relevant sections. The field $\mathbf{H}^{sc}$ is the short-circuited magnetic field, radiated by the impressed sources and the equivalent current $\mathbf{J}$ (existing only over the surface of the PEC load) when the aperture is covered by a PEC surface.

Equations (2) can be cast into coupled IEs by expressing all magnetic fields as superposition integrals (symbol $\otimes$) between the sources and the relevant dyadic GFs:

$$\begin{aligned} &\mathbf{H}^{im} + \underline{\mathbf{G}}^{C}_{HJ} \otimes \mathbf{J} + \underline{\mathbf{G}}^{C}_{HM} \otimes \mathbf{M}_i \\ &\quad = -\underline{\mathbf{G}}^{S}_{HM} \otimes \mathbf{M}_i + \underline{\mathbf{G}}^{M}_{HM} \otimes \mathbf{M}_e, \quad \mathbf{r} \in A_i \end{aligned} \quad (3a)$$

$$\underline{\mathbf{G}}^{(3)}_{HM} \otimes \mathbf{M}_e = -\underline{\mathbf{G}}^{S}_{HM} \otimes \mathbf{M}_e + \underline{\mathbf{G}}^{M}_{HM} \otimes \mathbf{M}_i, \mathbf{r} \in A_e \quad (3b)$$

where the cross product with $\mathbf{u}_z$ is suppressed throughout. The magnetic field $\mathbf{H}^{im}$ is that inside the closed cavity due to the impressed dipole sources only (expressed as a suitable combination of components of HM-/HJ-type dyadic GFs of the cavity $\underline{\mathbf{G}}^{C}_{HM}$ and $\mathbf{G}^{C}_{HJ}$), while $\underline{\mathbf{G}}^{M}_{HM}$ and $\underline{\mathbf{G}}^{S}_{HM}$ are the GFs of region 2 (i.e., $\underline{\mathbf{G}}^{(2)}_{HM}$) when observation and source point lie on the opposite and same surface, respectively. Finally, $\underline{\mathbf{G}}^{(3)}_{HM}$ is the dyadic GF of the external region.

The above formulation requires the evaluation of the GFs in (3); the $\underline{\mathbf{G}}^{(3)}_{HM}$ GF is not available, neither is the $\underline{\mathbf{G}}^{(2)}_{HM}$ GF of the closed aperture, except for simple shapes (e.g., rectangular). However, some approximations (discussed next) can be made which allow for a simple solution of the problem without affecting the overall accuracy.

The third equation is obtained by enforcing the EFIE on the surface S of the PEC load inside the enclosure, i.e.,

$$\mathbf{u}_n \times \left(\underline{\mathbf{G}}^{C}_{EM} \otimes \mathbf{M}_i + \underline{\mathbf{G}}^{C}_{EJ} \otimes \mathbf{J} \right) = \mathbf{0} \quad \text{on } S, \quad (4)$$

where $\mathbf{u}_n$ indicates the unit vector normal to S and the electric fields have been expressed as superposition integrals between the equivalent magnetic/electric currents and the EM-type/EJ-type dyadic GFs of the cavity $\underline{\mathbf{G}}^{C}_{EM}$ and $\underline{\mathbf{G}}^{C}_{EJ}$, respectively. Equations (3)-(4) form a set of coupled IEs which, once solved in the unknowns $\mathbf{M}_{i,e}$ and $\mathbf{J}$, allows for the computation of the EM field inside and outside the enclosure.

IV. NUMERICAL TOOLS

Several approximations can be made together with a clever use of acceleration and interpolation techniques to speed up the computation of all required quantities for the solution of the problem. The most important and somewhat crude and limiting assumption is the following: the enclosure wall containing the aperture is extended to infinity, so that region 3 coincides with the half-space $z > l_z + t$ and the GF of the outer region $\underline{\mathbf{G}}^{(3)}_{HM}$ can be substituted with twice the free-space GF $\underline{\mathbf{G}}^{fs}_{HM}$ (which is known in a simple closed form). As shown in [11] for empty enclosures excited by an impinging uniform plane wave, this approximation leads to an error on the calculated SE_E smaller than 2 dB, regardless of the aperture position. The main drawback of such an approximation is that the radiated field can be evaluated only inside the enclosure and in the half-space beyond the aperture. However, the field outside the enclosure is expected to be maximum right in such an half-space, which thus constitutes the critical region for SE evaluations (as will be discussed in detail in the numerical results). On the other hand, the appealing of such an approximation is enormous, since otherwise the solution of the problem would require the discretization of all the enclosure walls thus introducing an unacceptable number of unknowns.

It should be noted that for vanishing thickness t the formulation in (3) is unstable, since both the GFs $\underline{\mathbf{G}}^{M}_{HM}$ and $\underline{\mathbf{G}}^{S}_{HM}$ diverge. As first shown in [16], an alternative and robust representation can be obtained by introducing the auxiliary variables $\mathbf{M}_\Sigma = (\mathbf{M}_e + \mathbf{M}_i)/2$ and $\mathbf{M}_\Delta = (\mathbf{M}_e - \mathbf{M}_i)/2$ and the GFs $\underline{\mathbf{G}}^{\Sigma}_{HM} = \underline{\mathbf{G}}^{S}_{HM} + \underline{\mathbf{G}}^{M}_{HM}$ and $\underline{\mathbf{G}}^{\Delta}_{HM} = \underline{\mathbf{G}}^{S}_{HM} - \underline{\mathbf{G}}^{M}_{HM}$ so that (3) can equivalently be written as

$$\underline{\mathbf{G}}_{\mathrm{HJ}}^{\mathrm{C}} \otimes \mathbf{J} + \left(\underline{\mathbf{G}}_{\mathrm{HM}}^{\mathrm{C}} + 2\underline{\mathbf{G}}_{\mathrm{HM}}^{\Delta} + 2\underline{\mathbf{G}}_{\mathrm{HM}}^{\mathrm{fs}}\right) \otimes \mathbf{M}_{\Sigma} + \left(2\underline{\mathbf{G}}_{\mathrm{HM}}^{\mathrm{fs}} - \underline{\mathbf{G}}_{\mathrm{HM}}^{\mathrm{C}}\right) \otimes \mathbf{M}_{\Delta} = -\mathbf{H}^{\mathrm{im}} \quad (5)$$

$$\left(\underline{\mathbf{G}}_{\mathrm{HM}}^{\Delta} + 2\underline{\mathbf{G}}_{\mathrm{HM}}^{\mathrm{fs}}\right) \otimes \mathbf{M}_{\Sigma} + \left(\underline{\mathbf{G}}_{\mathrm{HM}}^{\Sigma} + 2\underline{\mathbf{G}}_{\mathrm{HM}}^{\mathrm{fs}}\right) \otimes \mathbf{M}_{\Delta} = \mathbf{0}$$

which will be discussed next.

A. Thin Apertures

For very thin walls, the case of a zero-thickness aperture can be considered. In such a case the surfaces A_{e} and A_{i} coincide with the unique surface A, only one equivalent magnetic current $\mathbf{M}$ is introduced, and (3)-(4) actually reduce to *two* coupled equations

$$\mathbf{H}^{\mathrm{im}} + \underline{\mathbf{G}}_{\mathrm{HJ}}^{\mathrm{C}} \otimes \mathbf{J} + \underline{\mathbf{G}}_{\mathrm{HM}}^{\mathrm{C}} \otimes \mathbf{M} = -2\underline{\mathbf{G}}_{\mathrm{HM}}^{\mathrm{fs}} \otimes \mathbf{M}, \quad \mathbf{r} \in A \quad (6)$$

$$\mathbf{u}_n \times \left(\underline{\mathbf{G}}_{\mathrm{EM}}^{\mathrm{C}} \otimes \mathbf{M} + \underline{\mathbf{G}}_{\mathrm{EJ}}^{\mathrm{C}} \otimes \mathbf{J}\right) = \mathbf{0} \quad \text{on } S.$$

B. Thick Apertures

As already mentioned above, for thick apertures the system consists of *three* coupled equations. However, for not too large thicknesses, one can assume $\mathbf{M}_{\Delta} = \mathbf{0}$; as shown in [11] for the case of impinging plane waves (and based on the theory developed in [16]), the two coupled equations (5) thus reduce to the *unique* equation

$$\underline{\mathbf{G}}_{\mathrm{HJ}}^{\mathrm{C}} \otimes \mathbf{J} + \left(\underline{\mathbf{G}}_{\mathrm{HM}}^{\mathrm{C}} + 2\underline{\mathbf{G}}_{\mathrm{HM}}^{\Delta} + 2\underline{\mathbf{G}}_{\mathrm{HM}}^{\mathrm{fs}}\right) \otimes \mathbf{M}_{\Sigma} = -\mathbf{H}^{\mathrm{im}} \quad (7)$$

which is formally the same as the first of (6) for the zero-thickness case except for the perturbation term $\underline{\mathbf{G}}_{\mathrm{HM}}^{\Delta}$ which accounts for the finite thickness. As shown in [16], an approximate general expression for $\underline{\mathbf{G}}_{\mathrm{HM}}^{\Delta}$ GF can be obtained by considering the short-circuited cavity as a parallel-plate waveguide; such an expression is available in a simple closed form in the spectral domain and its calculation in the spatial domain requires only the evaluation of a Sommerfeld integral (for details, see [11]).

C. Use of Different Basis Functions for Rectangular Apertures

To discretize (2) and (3), the unknowns (equivalent electric and magnetic currents) need to be expanded through a suitable complete set of vector basis functions (BFs). In order to identify the most convenient representation, several BFs have been tested to represent the equivalent magnetic current on the surface of the aperture and the electric current on the surfaces of the interior conductors.

First, classical Rao-Wilton-Glisson (RWG) rooftop functions [17] have been used: the aperture and the surfaces of the interior conductors have been discretized through nonoverlapping triangles and the unknown current densities $\mathbf{M}$ (or $\mathbf{M}_{\Delta}$) and $\mathbf{J}$ have been expanded in RWG functions as

$$\mathbf{M}(\mathbf{r}) = \sum_{i=1}^{N} a_i^{\mathrm{M}} \boldsymbol{\Lambda}_i(\mathbf{r}), \quad \mathbf{J}(\mathbf{r}) = \sum_{i=1}^{N} a_i^{\mathrm{J}} \boldsymbol{\Lambda}_i(\mathbf{r}), \quad (8)$$

where a_i^{M} and a_i^{J} are unknown complex amplitudes. In the case of thick apertures, when the two surfaces A_{i} and A_{e} have the same shape (which is common in practical cases), the magnetic currents on both the interfaces should share the same mesh to make easier the computation of $\mathbf{M}_{\Sigma}$ and $\mathbf{M}_{\Delta}$.

Alternatively to RWG BFs, in order to achieve a better accuracy, first-order triangular patch (LL) BFs [18] have also been used. In this case, two BFs are associated with each interior edge i of the mesh ($i = 1, \ldots, N_E$) and they are defined on two adjacent triangles T_i^+ and T_i^-, uniquely identified by such i-th edge. These BFs can be expressed as

$$\boldsymbol{\Lambda}_i^1 = \begin{cases} \dfrac{\ell_i}{2A_i^+} \xi_{i+1} \mathbf{l}_{i-1} & \text{if } \mathbf{r} \in T_i^+ \\ \dfrac{\ell_i}{2A_i^-} \xi_{i-1} \mathbf{l}_{i+1} & \text{if } \mathbf{r} \in T_i^- \\ \mathbf{0} & \text{otherwise} \end{cases}$$

$$\boldsymbol{\Lambda}_i^2 = \begin{cases} \dfrac{\ell_i}{2A_i^+} \xi_{i-1} \mathbf{l}_{i+1} & \text{if } \mathbf{r} \in T_i^+ \\ \dfrac{\ell_i}{2A_i^-} \xi_{i+1} \mathbf{l}_{i-1} & \text{if } \mathbf{r} \in T_i^- \\ \mathbf{0} & \text{otherwise} \end{cases} \quad (9)$$

where ℓ_i is the length of the i-th edge, $A_i^{\pm}$ are the areas of the surface triangular patches, ξ_i are the area coordinates, and $\mathbf{l}_i$ is the vector associated

with the edge i. Following the notation used in [19], these BFs provide a linear normal-linear tangent (LN/LT) approximation of the current.

Adding two second-order BFs local to each triangle j ($j=1,...,N_T$) as suggested in [19], it is also possible to obtain a quadratic tangent (LN/QT) approximation along the edges. However, intense testing has demonstrated that the coefficients of these BFs are always two orders of magnitude smaller than the coefficients of the six linear functions, thus not providing a substantial improvement in the modeling of the current.

As concerns the singularities, the GFs in the three regions show a singularity $1/R$ as the observation point approaches the source; in the proposed approach, such a singularity is extracted and analytical formulas [20] are used for the correct integration of the static 3-D GF times the linear vector BFs on source triangles. Classical Gaussian quadrature rules are then used to compute all the remaining source and testing integrals [21].

Finally, entire-domain (ED) BFs have also been used to represent the magnetic current on rectangular apertures. In fact, the use of ED BFs, although restricted to simple geometries, is appealing because it allows for incorporating the possible diverging behavior of the current along the aperture edges and for significantly reducing the size of the MoM matrix. Using ED BFs, the equivalent magnetic current is expressed as

$$M_x = \sqrt{\frac{1-u^2}{1+v^2}} \sum_{m=0}^{M} \sum_{n=0}^{N} M_{0x}^{mn} U_m(u) T_n(v)$$
$$M_y = \sqrt{\frac{1-v^2}{1+u^2}} \sum_{m=0}^{M} \sum_{n=0}^{N} M_{0y}^{mn} U_m(v) T_n(u) \qquad (10)$$

where $M_{0x,y}^{mn}$ are unknown coefficients and $U_n(\cdot)$ and $T_n(\cdot)$ are the n-th order Chebyshev polynomial of first and second kind, respectively. The normalized variables $u=(2x-\ell_x)/\ell_x$ and $v=(2y-\ell_y)/\ell_y$ have been introduced to define the polynomials over the interval $[-1,+1]$ where they are orthogonal. Physically, the equivalent magnetic current components display an inverse square-root singularity at the edges tangential to the direction of the current, while they vanish at the edges normal to such a direction. This behavior is explicitly enforced in the functions in (10) so that they are expected to converge more rapidly to the exact solution. As concerns integration, numerical adaptive formulas have been used to carry out both the source and testing integrals.

It is worth mentioning that the singular behavior at the edges parallel to the direction of the magnetic current could also be enforced over a triangular mesh recurring to special singular RWG functions [22], but with an additional increase of preprocessing and computational efforts. (It should also be noted that in the presence of thick apertures the degree of singularity at the edges is different and another set of ED BFs, involving Gegenbauer polynomials, should be used.)

D. Acceleration of Green's Functions Calculation

Equations (2)-(3) can efficiently be solved by means of the MoM technique (with Galerkin's method) once they have been recast in a mixed-potential form (which is preferred because of the lower-order singularity in the integral kernel) [23]. Introducing the auxiliary potentials $\mathbf{A}$, V, $\mathbf{F}$, and W, the convolution terms can be expressed in terms of potential GFs $\underline{\mathbf{G}}_{A,F}$ and $G_{V,W}$ which, for the free-space case, are known in a simple closed form [1].

From a numerical point of view, a fast computation of the cavity GFs is required to make the proposed integral procedure an efficient technique alternative to classical full-wave methods. The four enclosure GFs are the two dyadic potential $\underline{\mathbf{G}}_{A,F}^{C}$ (which are diagonal) and the two scalar potential $G_{V,W}^{C}$. As is well known, the evaluation of the GFs of a rectangular cavity with PEC walls is a daunting task: two classical representations exist, the image and the modal representations, which are both very slowly converging. An efficient numerical acceleration scheme (based on the Ewald representation) is thus adopted, for which the GFs are expressed as a sum of two Gaussian fast-decaying convergent series which depend on the splitting parameter E [24]. The choice of the optimum E plays a crucial role in determining the rapidly-converging character of the series (which actually are multi-

index series and require a clever choice of the strategy used for their numerical summation); several useful details about these issues are given in [25]. Finally, the curls of the GFs can also be computed efficiently in a similar way: the relevant expressions can be found in [26].

E. Interpolation of the Enclosure Green's Function

To further speed-up the computation of all involved GFs, an interpolation technique has been developed in [26], extending the polynomial modeling previously presented in [27].

As concerns the four enclosure GFs, they can be interpolated by means of a triple series of Chebyshev polynomials of the first kind as reported in [26], after extracting their singularities and the singularities in their first derivatives. However, with respect to [26] where odd and even Chebyshev polynomials were used, here we used only even polynomials (this is obtained by interpolating the function $\tilde{D}_q / q$ defined in [26] instead of $\tilde{D}_q$).

The fast computation of the coefficients of the resulting Chebyshev series is a key step to ensure the efficiency of the interpolation. This can be obtained by means of a clever application of the 3-D Fast Cosine Fourier Transform, while the evaluation of the series can be performed by applying the Clenshaw algorithm (for details, see [26],[27]).

V. NUMERICAL RESULTS

A. Choice of the Basis Functions

If not otherwise specified, in all the numerical results presented next, a rectangular $l_x \times l_y \times l_z$ metallic enclosure having a rectangular $a_x \times a_y$ aperture placed in the middle of the wall in the $z = l_z$ plane is considered. The structure is excited by a y-oriented electric dipole placed in the middle of the cavity and the observation point for SE evaluations is located along an axis parallel to z, passing through the aperture center, and at a distance d from it.

A first interesting investigation concerns the determination of the best set of BFs for an accurate SE_E computation. Three different sets have been presented in Section IV.C and all of them have been tested in order to point out their advantages or drawbacks. A specific case is presented in Fig. 3, although the conclusions are general; an empty rectangular metallic enclosure with dimensions $l_x = l_z = 30$ cm and $l_y = 12$ cm has been considered, having a zero-thickness aperture with $a_x = 15$ cm and $a_y = 4$ cm, operating at the frequency $f = 1.5$ GHz. In Fig. 3, the behavior of the amplitude $M = |\mathbf{M}|$ is reported as a function of the observation point over the aperture for RWG BFs (a), LL BFs (b), and ED BFs (c).

It can be observed that, keeping a reasonable number of BFs, ED BFs provide the most accurate representation of the current, which is instead poor in the case of RWG BFs. A smoother curve is obtained through LL BFs, but at the cost of a double number of BFs (compared with RWG BFs with the same mesh). However, when dealing with moderate-size problems, the use of LL BFs significantly improves the accuracy of the solution with the same number of unknowns (i.e., using less triangles) and provides a faster convergence. Despite of these differences, the results obtained for the radiated electric field are *undistinguishable*. In conclusion, ED BFs furnish the most convenient numerical representation because a very small number is required, which entails a smaller MoM matrix size and a smaller number of integrations. On the other hand, if apertures of noncanonical shape are considered, the use of RWG basis functions (about 24 per wavelength) is sufficient to obtain accurate results for the radiated field.

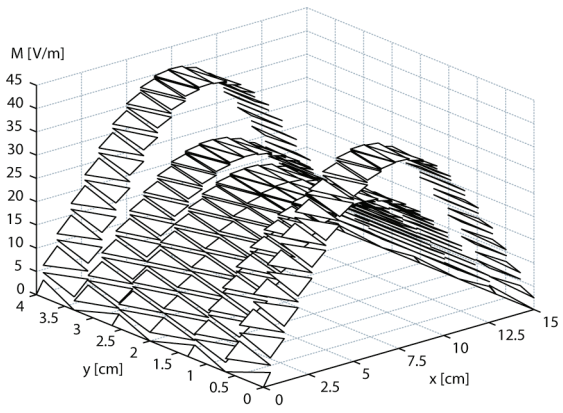

(a)

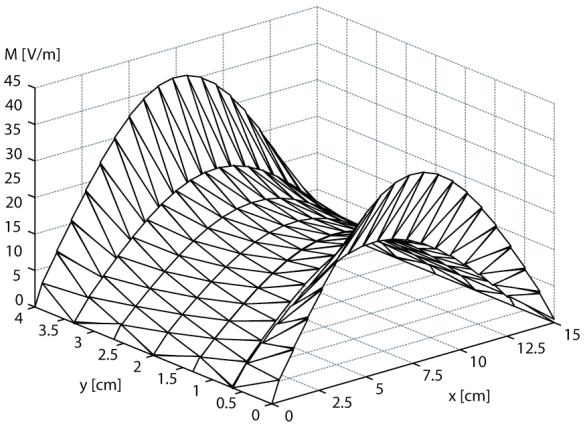

(b)

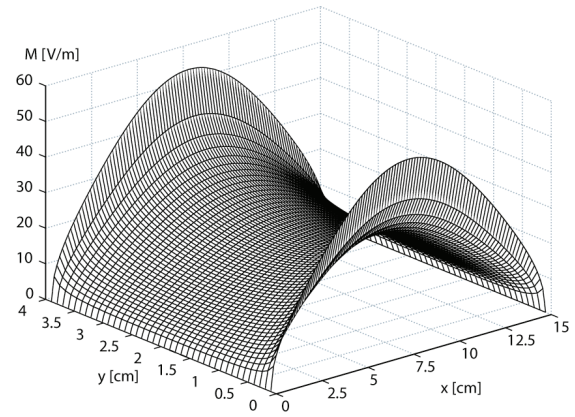

(c)

Fig. 3. Modeling of the equivalent magnetic current using different BFs: RWG (a), LL (b), and ED BFs (c). Parameters are in the text.

B. Thin and Thick Apertures

After testing the use of different types of BFs, we focus on the SE evaluation. A rectangular metallic enclosure with dimensions $l_x = l_y = l_z = 15$ cm has been considered, having aperture dimensions $a_x = 10$ cm and $a_y = 0.5$ cm (i.e., a narrow slot). In Fig. 4, the electric shielding effectiveness SE_E is reported as a function of frequency for an aperture with zero thickness ($t = 0$ mm) and for a thick aperture with $t = 5$ mm. The observation point is located at a distance $d = 20$ cm (i.e., $d = \lambda_0$ at $f = 1.5$ GHz). It can be observed that, as in the case of plane-wave illumination [11], in the case of long slots the finite thickness of the aperture increases the value of the SE_E also by several dB, especially in the low-frequency range. (It should be noted that the enclosure presents resonant frequencies at $f =$ 1.41, 1.73, 2.23, 2.45, 2.83, and 3 GHz, but only few of them are observed in Fig. 4, since for symmetry properties some modes are not excited by the source [1].)

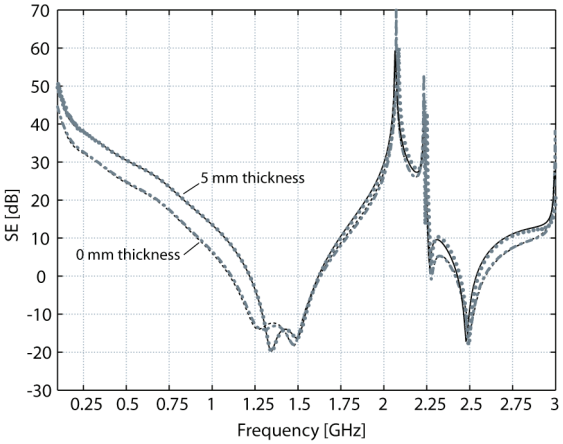

Fig. 4. Electric shielding effectiveness SE_E obtained through the proposed approach (solid line) and CST (dotted line) as a function of frequency for a thin and a thick aperture. Parameters are in the text.

In order to check the accuracy of the proposed approach, our results (solid lines) have been compared with those obtained through the commercial software CST Microwave Studio (based on the Finite Integration Technique in the time domain, dotted lines) and the agreement is excellent. However, even with the use of two planes of symmetry, CST requires a very long simulation time (a mesh with 71300 cells has been used, ensuring 20 cells for wavelength at 3 GHz). To accelerate the simulation, an auto-regressive filter could be used for calculating the frequency spectra without waiting for the probe time signal to reach the steady state, but the accuracy of the results strongly depends on the filter settings, which are very case sensitive.

As explained at the beginning of Section IV, a fundamental approximation of the proposed MoM approach consists in the replacement of the cavity wall containing the aperture with an infinite PEC plane. In the previous results it has been shown that such an approximation does not affect the accuracy of the formulation, at least for points located along the axis parallel to z and passing through the center of the aperture and in the

middle of the enclosure. However, the proposed formulation will certainly fail in evaluating the SE_E for points outside the enclosure and located in the half-space $z < l_z$ (since for the above-mentioned approximation the proposed approach gives a null field in such points). However, this is not a critical drawback since, by trivial considerations, the largest value of the electric field radiated by the dipoles is expected to be found in the half-space $z > l_z$. In any case, it would be interesting to know the limits of the region within which the proposed approach gives accurate results. For this reason, in Fig. 5 the same structure as in Fig. 3 is considered and the electric-field value (in dBV/m) is reported as a function of the angle θ (measured from the axis z with the origin placed at the center of the aperture) on the xz (a) and yz (b) planes, respectively, for different distances ($d =$ 5, 10, 20 cm) from the aperture center at the operating frequency $f = 1.5$ GHz. The results obtained through the proposed approach (solid lines) are compared with the full-wave results obtained through CST (dotted lines) and several remarks can be made.

First, as expected, the electric-field values are lower and lower by increasing the distance from the aperture (in Fig. 5 such values are normalized with respect to the maximum value present in the $d = 5$-cm case).

Let us consider now the xz plane (Fig. 5(a)); the length of the cavity wall along x is $l_x = 30$ cm, while the aperture dimension is $a_x = 10$ cm so that the curves corresponding to $d = 5$ cm and $d = 10$ cm end at $\theta = \pm 90^\circ$ (for which the observation point lies on the cavity wall), whereas the curve corresponding to $d = 20$ cm extends in the $z < l_z$ half-space. Interestingly, the pattern is almost isotropic in the very near-field region over the whole angular range (for $d = 5$ cm) or in a very wide angular range (for $d = 10$ cm and $d = 20$ cm). In any case, a very good agreement is always obtained in the $z > l_z$ half-space, while the electric-field values for $z < l_z$ when $d = 20$ cm are completely negligible (about 25 dB lower than the maximum value occurring at $\theta = 0^\circ$).

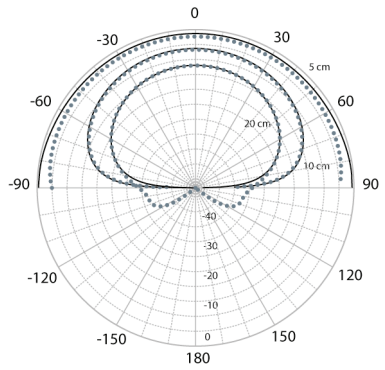

(a)

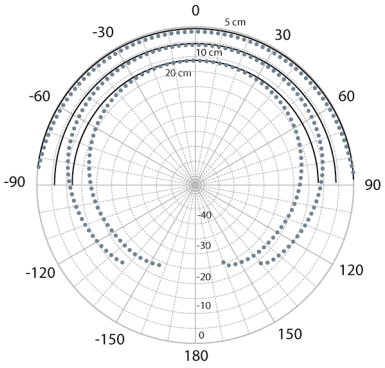

(b)

Fig. 5. Normalized electric-field amplitudes (in dBV/m) obtained through the proposed approach (solid line) and CST (dotted line) for different values of d in the xz (a) and yz plane (b). Parameters are in the text.

As concerns the yz plane (Fig. 5(b)), it results $l_y = 12$ cm and $a_y = 4$ cm; in this case only the curve corresponding to $d = 5$ cm ends at $\theta = \pm 90^\circ$. As in the xz plane, the pattern is almost isotropic over the whole angular range and an excellent agreement is obtained between the results of the proposed approach and those of CST. The curves corresponding to $d = 10$ cm and $d = 20$ cm extend in the $z < l_z$ lower half-space; they are nearly isotropic over the whole angular range for $z > l_z$ and a very good agreement is obtained between our formulation and the full-wave results (the maximum error is about 5 dB and obviously occurs over the plane $z = l_z$). In any case, the electric-field values for $z < l_z$ are lower than those for $z > l_z$ by about 5 – 10 dB, thus

confirming that the maximum radiation is obtained in the half-space above the aperture.

C. Loaded Enclosures

It is then interesting to study the effects of possible PEC loadings placed inside the enclosure. The same structure as in Fig. 5 (with a zero-thickness aperture) has been considered but loaded with a PEC plate parallel to the yz plane, with dimensions $d_y = 8$ cm and $d_z = 20$ cm and with its center located at (7, 6, 12) cm. (It should be noted that if the plates are connected to the cavity walls, suitable local basis functions defined on the triangles at the edges between the plates and the cavity walls have to be used, as done in [26].)

First, the SE_E of the empty enclosure has been studied as a function of frequency for $d = 20$ cm. The relevant results are reported in Fig. 6(a) (solid line) and they are compared with those obtained with both CST (dotted line) and FEKO (based on a frequency domain MoM, dashed line), showing an excellent agreement.

In Fig. 6(b), the SE_E of the loaded enclosure is reported, with the observation point as in Fig. 6(a). In this case, the calculation of the SE_E has been performed through the definition (1), where $\mathbf{E}^{\mathrm{inc}}(\mathbf{r})$ is assumed as the electric field radiated by the electric dipole *in the presence of the plate* and in the absence of the enclosure. Again, the results obtained with the proposed approach are in excellent agreement with those obtained with both CST and FEKO. However, FEKO uses 3504 triangles (10 triangles per wavelength) and requires about 2 hours to compute 601 frequency points (on a 3 GHz Intel Quad Core CPU), while CST uses 75800 cells and requires about 3 hours (with parallelization on four threads) to extinguish the transient inside the enclosure with an accuracy of -60 dB (in this case, due to the presence of the loading, only one plane of symmetry can be used). The proposed method, with 376 overall unknowns, requires just 72 minutes to compute 601 frequency points, providing a dramatic acceleration without affecting the accuracy of the results. A comparison between Fig. 6(a) and (b) also reveals that the SE_E is seriously affected by the presence of the PEC plate, especially in the high-frequency range.

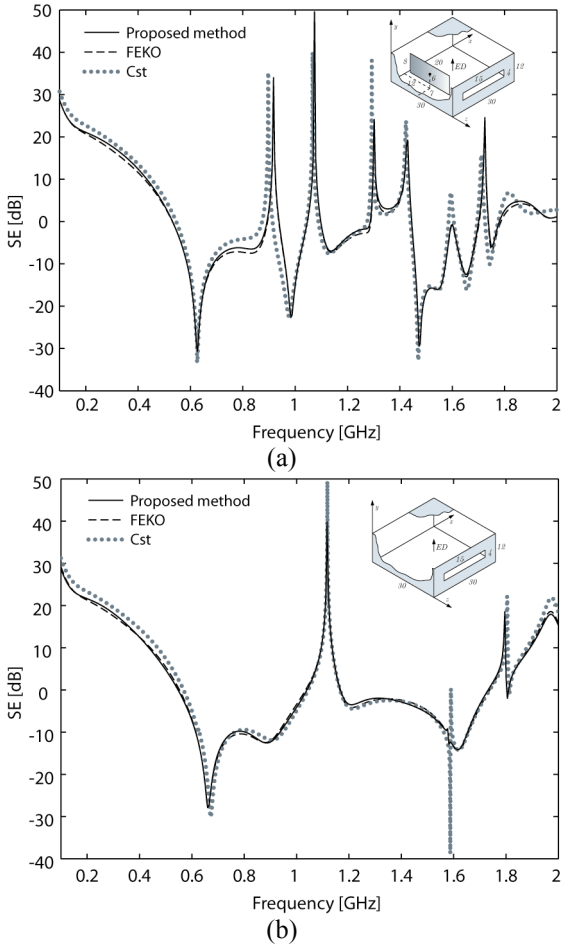

Fig. 6. SE_E obtained through the proposed approach (solid line), CST (dotted line), and FEKO (dashed line) as a function of frequency. Empty enclosure (a); loaded enclosure (b). Parameters are in the text.

D. Different Dipole Sources and Orientations

Finally, different types and orientations of the dipole sources have been considered. In fact, while an electric dipole represents a short linear antenna, a magnetic dipole may represent a small loop antenna lying on the plane orthogonal to the dipole direction. The SE_E has been calculated as a function of frequency for the same structure as in Fig. 4 at a distance $d = 20$ cm from the aperture.

In Fig. 7(a), the effects of electric dipole sources placed in the center of the enclosure and directed along the main axes (x, y, z) are reported. It can be seen that the worst case is represented by a y-oriented dipole (i.e., parallel to the shortest side of the aperture), which gives rise to values of

SE_E several dB lower than those corresponding to the other dipole orientations. The latter orientations present critical values of the SE_E only in correspondence of the resonant frequencies of the metallic cavity.

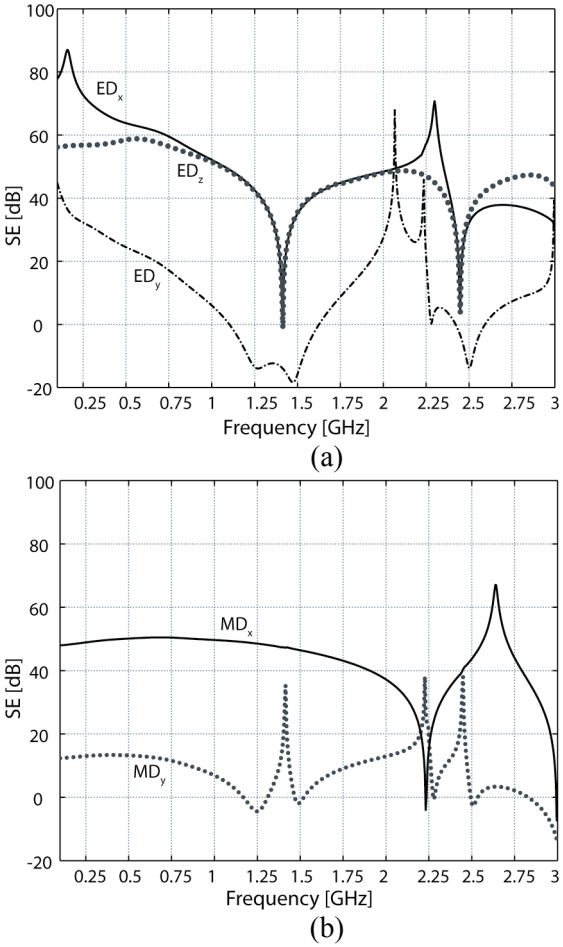

Fig. 7. SE_E obtained through the proposed approach as a function of frequency for different kind of sources and orientations: electric dipole (a) and magnetic dipole (b). Parameters are in the text.

In Fig. 7(b), the SE_E due to magnetic dipoles placed in the center of the enclosure and directed along the main axes (x, y, z) is shown. It can be seen that also for this excitation the worst case is represented by a y-oriented dipole (i.e., parallel to the shortest side of the aperture). It should be noted that no curve is reported corresponding to the z-oriented magnetic dipole: in fact, in such a case the planes containing the dipole and orthogonal to the xy plane are equivalent to PEC planes (by symmetry), so that at the observation point (which lies along the intersection between such planes) the electric field is null [1].

VI. CONCLUSIONS

This work has presented a detailed study of the shielding effectiveness of rectangular metallic enclosures having thin or thick apertures, possibly loaded with conducting bodies and the problem of a finite-source excitation (i.e., an arbitrarily oriented electric or magnetic dipole placed inside the cavity) has been addressed, instead of the more conventional plane-wave excitation; in fact, the dipoles may represent practical sources such as short-linear or small-loop antennas. An efficient Method-of-Moment formulation has been developed which overcomes typical difficulties of the classical approach through the use of acceleration techniques for the computation of the dyadic enclosure Green's function, interpolation schemes, different sets of basis functions modeling the apertures, and approximations which dramatically simplify the problem. Such approximations have been critically discussed and it has been shown how they still allow for maintaining a high level of accuracy in the problem solution. The efficiency and the accuracy of the proposed approach has been fully validated by means of comparisons with results obtained through independent full-wave software, thus showing the validity and the appealing of the method in solving this classical electromagnetic problem.

REFERENCES

[1] S. Celozzi, R. Araneo, and G. Lovat, *Electromagnetic Shielding*, Wiley-IEEE, Hoboken, 2008.

[2] W. Wallyn, D. De Zutter, and H. Rogier, "Prediction of the shielding and resonant behavior of multisection enclosures based on magnetic current modeling," *IEEE Trans. Electromagn. Compat.*, vol. 44, no. 1, pp. 130–138, Feb. 2002.

[3] F. Olyslager, E. Laermans, D. De Zutter, S. Criel, R. De Smedt, N., Lietaert, and A. De Clercq, "Numerical and experimental study of the shielding effectiveness of a metallic enclosure," *IEEE Trans. Electromagn. Compat.*, vol. 41, no. 3, pp. 202–213, Aug. 1999.

[4] M. P. Robinson, T. M. Benson, C. Christopoulos, J. F. Dawson, M. D. Ganley, A. C. Marvin, S. J. Porter, and D. W. P. Thomas, "Analytical formulation for the shielding effectiveness of enclosures with apertures," *IEEE Trans. Electromagn. Compat*., vol. 40, no. 3, pp. 240–248, Aug. 1998.

[5] R. Azaro, S. Caorsi, M. Donelli, and G. L. Gragnani, "A circuital approach to evaluating the electromagnetic field on rectangular apertures backed by rectangular cavities," *IEEE Trans. Microw. Theory Tech*., vol. 50, no. 10, pp. 2259–2264, Oct. 2002.

[6] T. Konefal, J. F. Dawson, A. Marvin, M. P. Robinson, and S. J. Porter, "A fast multiple mode intermediate level circuit model for the prediction of shielding effectiveness of a rectangular box containing a rectangular aperture," *IEEE Trans. Electromagn. Compat*., vol. 47, no. 4, pp. 678–691, Nov. 2006.

[7] S. Benhassine, L. Pinchon, and W. Tabbara, "An efficient finite-element time-domain method for the analysis of the coupling between wave and shielded enclosure," *IEEE Trans. Magn.*, vol. 38, no. 2, pp. 709–712, Feb. 2002.

[8] H. H. Park and H. J. Eom, "Electromagnetic penetration into a rectangular cavity with multiple rectangular apertures in a conducting plane," *IEEE Trans. Electromagn. Compat*., vol. 42, no. 3, pp. 303–307, Aug. 2000.

[9] G. Cerri, R. De Leo, and V. M. Primiani, "Theoretical and experimental evaluation of the electromagnetic radiation from apertures in shielded enclosures," *IEEE Trans. Electromagn. Compat.*, vol. 34, no. 4, pp. 423–432, Nov. 1992.

[10] V. Rajamani, C. F. Bunting, M. D. Deshpande, and Z. A. Khan, "Validation of Modal/MoM in shielding effectiveness studies of rectangular enclosures with apertures," *IEEE Trans. Electromagn. Compat.*, vol. 48, no. 2, pp. 348–352, May 2006.

[11] R. Araneo and G. Lovat, "An efficient MoM formulation for the evaluation of the shielding effectiveness of rectangular enclosures with thin and thick apertures," *IEEE Trans. Electromagn. Compat.*, vol. 50, no. 2, pp. 294–304, May 2008.

[12] M. Li, J. Nuebel, J. L. Drewniak, T. H. Hubing, R. E. DuBroff, and T. P. Van Doren, "EMI from cavity modes of shielding enclosures – FDTD modeling and measurements," *IEEE Trans. Electromagn. Compat.*, vol. 42, no.1, pp. 29–38, Jan. 2000.

[13] S. V. Georgakapoulos, C. R., Birtcher, and C. A. Balanis, "HIRF penetration through apertures: FDTD versus measurements," *IEEE Trans. Electromagn. Compat.*, vol. 43, no. 3, pp. 282–294, Aug. 2001.

[14] C. Jiao, X. Cui, L. Li, and H. Li, "Subcell FDTD analysis of shielding effectiveness of a thin-walled enclosure with an aperture," *IEEE Trans. Magn.*, vol. 42, no. 4, pp. 1075–1078, Apr. 2006.

[15] C. Feng and Z. Shen, "A hybrid FD-MoM technique for predicting shielding effectiveness of metallic enclosures with apertures," *IEEE Trans. Electromagn. Compat.*, vol. 47, no. 3, pp. 456–462, Aug. 2005.

[16] J. R. Mosig, "Scattering by arbitrarily-shaped slots in thick conducting screen: An approximate solution," *IEEE Trans. Antennas Propag.*, vol. 52, no. 8, pp. 2109–2117, Aug. 2004.

[17] S. M. Rao, D. R. Wilton, and A. W. Glisson, "Electromagnetic scattering by surfaces of arbitrary shape," *IEEE Trans. Antennas Propag.*, vol. 30, no. 3, pp. 409–418, Mar. 1982.

[18] L. C. Trintinalia, and H. Ling "First order triangular patch basis functions for electromagnetic scattering analysis," *J. Electromagn. Waves Appl.*, vol. 15, no. 11, pp. 1521–1537, 2001.

[19] A. F. Peterson, S. L. Ray, and R. Mittra, *Computational Methods for Electromagnetics*, IEEE Press, Piscataway, 1998.

[20] R. D. Graglia, "On the numerical integration of the linear shape functions times the 3-D Green's function or its gradient on a plane triangle," *IEEE Trans. Antennas Propag.*, vol. 41, no. 10, pp. 1448–1455, Oct. 2001.

[21] D. A. Dunavant, "High degree efficient symmetrical gaussian quadrature rules for the triangle," *Intern. Journal Num. Meth. Engineering*, vol. 21, pp. 1129–1148, 1985.

[22] J. W. Brown and D. R. Wilton "Singular basis functions and curvilinear triangles in the solution of the electric field integral equation," *IEEE Trans. Antennas Propag.*, vol. 47, no. 2, pp. 347–353, Feb. 2001.

[23] J. R. Mosig, "Integral equation technique," *Numerical techniques for microwave and millimeter wave passive structures*, Wiley, 1989.

[24] M.-J. Park, J. Park, and S. Nam, "Efficient calculation of the Green's function for the rectangular cavity," *IEEE Microwave Guided Wave Lett.*, vol. 8, no. 3, pp. 124–126, Mar. 1998.

[25] G. Lovat, P. Burghignoli, and R. Araneo, "Efficient evaluation of the three-dimensional periodic Green's function through the Ewald method," *IEEE Trans. Microw. Theory Tech.*, vol. 56, no. 9, pp. 2069–2075, Sep. 2008.

[26] R. Araneo and G. Lovat, "Fast MoM analysis of the shielding effectiveness of rectangular enclosures with apertures, metal plates, and conducting objects," *IEEE Trans. Electromagn. Compat.*, vol. 51, no. 2, pp. 274–283, Feb. 2009.

[27] A. Borij and S. Safavi-Naeni, "Rapid calculation of the Green's function in a rectangular enclosure with application to conductor loaded cavity resonators," *IEEE Trans. Microw. Theory Tech.*, vol. 52, no. 7, pp. 1724–1731, Jul. 2004.

Rodolfo Araneo was born in Rome, Italy, on October 29, 1975. He received the M.S. (*cum laude*) and Ph.D. degrees in electrical engineering from the University of Rome "La Sapienza", Rome, in 1999 and 2002, respectively.

During the master thesis in 1999 he was a Visiting Student at the National Institute of Standards and Technology (NIST) Boulder, CO where he worked on TEM cells and shielding. During the second semester of the year 2000 he was a Visiting Researcher of the Department of Electrical and Computer Engineering of University of Missouri–Rolla (UMR) where he worked on printed circuit boards and finite-difference time-domain techniques.

Dr. Araneo received the Past President's Memorial Awards in 1999 from IEEE EMC Society. His research activity is mainly in the field of electromagnetic compatibility (EMC) and includes numerical and analytical techniques for modelling high-speed printed circuit boards, shielding, and transmission line analysis.

Giampiero Lovat was born in Rome, Italy, on May 31, 1975. He received the Laurea degree (*cum laude*) in electronic engineering and the Ph.D. degree in applied electromagnetics, both from "La Sapienza" University of Rome, Rome, Italy, in 2001 and 2005, respectively.

In 2005, he joined the Electrical Engineering Department of "La Sapienza" University of Rome, where he is currently an Associate Researcher. From January 2004 to July 2004 he was a Visiting Scholar at the University of Houston, Houston, Texas. His present research interests include leaky-wave antennas, general theory and numerical methods for the analysis of periodic structures, electromagnetic theory of complex media, and shielding analysis of enclosures and of planar composite screens.

Dr. Lovat received a Young Scientist Award from the 2005 URSI General Assembly, New Delhi, India.

Wideband Equivalent Circuit Model and Parameter Computation of Automotive Ignition Coil Based on Finite Element Analysis

Jia Jin, Wang Quan-di, Yu Ji-hui, Zheng Ya-li

State Key Laboratory of Power Transmission Equipment & System Security and New Technology, Chongqing University, Chongqing 400030, China
twoj1985-163.com@163.com, wangquandi@yahoo.com.cn, yujihui@cqu.edu.cn, yaya9304@163.com

Abstract- This paper presents a coupled field-circuit method to predict the wideband characteristic of ignition coils. A lumped circuit model is proposed, which separates the winding of ignition coil into individual sections. In this circuit model, the capacitance between sections, turn-to-turn series capacitance of each single section and inductance of winding are calculated by Finite Element Analysis (FEA). This parameter identification is based on the energy principle. In addition, this paper analyzes the influence of frequency on the magnetic-flux distribution and the inductance, using the finite-element model with T-Ω formulation. The parameter inductance applied to the circuit model is classified into high frequency inductance and low frequency inductance. Through contrasting the measured and calculated result in frequency and time domain, reliability and feasibility of the presented method in this paper is verified.

Index Terms—Coupled field-circuit method, wideband characteristic, ignition coil, Finite Element Analysis (FEA), T-Ω formulation.

I. INTRODUCTION

Ignition coil acts as a transient voltage transformer in the ignition process [1]. Its function is to convert a low-voltage DC source into a very high and fast transient voltage at the spark plug gap. Due to the primary and secondary coil inductance, stray capacitance, and core eddy current loss, the ignition coil terminal characteristics become more sophisticated than in the stationary state. Thus, it is necessary to couple the finite element analysis (FEA) with an electric circuit model to perform system-level simulation.

In general, there are three main categories of models for a transient voltage transformer. The first type is the winding model, which is based on the multiconductor transmission-line theory (MTL) [2-3]. The second type [4-5] is the terminal or black box model, which provides the terminal characteristics of the transformer and is not necessarily related to a transformer's internal condition. The third type is the physical model; it can model all parts of the transformer in great detail and can be constructed according to equivalent lumped electric circuit parameters [6-7].

It is a crucial problem to correctly extract the equivalent parameters for establishing the wideband circuit model of the transient transformer. Methods for obtaining the parameters include the analytic method [3, 6], experimental method [5] and the numerical method [2, 8] (especially FEA). Because of the high computational accuracy and wide adaptation to complicated physical models, FEA provides the most useful avenue to obtain the stray parameters of transformer and investigate the steel core characteristic depending on the frequency.

A wideband, lumped parameter equivalent circuit model topology for ignition coil is proposed. Then the parameters in the circuit model are presented using electromagnetic finite element analysis. Finally, the measured and simulated frequency- and time-domain results are given and analyzed. These results show that the proposed model accurately predicts the ignition coil terminal responses in the frequency range between 100Hz and 10MHz.

II. COMPUTATIONAL MODEL

The ignition coil 2D cross-section is described in Fig. 1 (a). The primary winding has 150 turns and secondary has 13000 turns. Figure 1 (b) shows a single section of the secondary winding, which consists of hundreds of coated copper wires. The

wires in this secondary section are arranged of approximate 30 layers and 60 turns per layer.

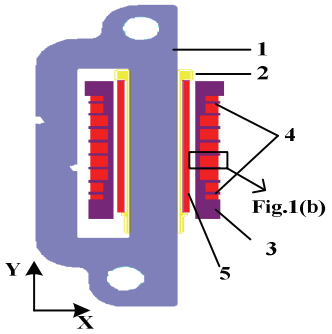

Fig.1(b)

(a)

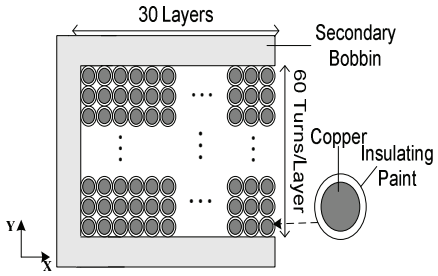

(b)

Fig. 1. Physical model of ignition coil, 1—Steel Core; 2—Primary Bobbin; 3—Secondary Bobbin; 4—Secondary Winding; 5—Primary Winding.

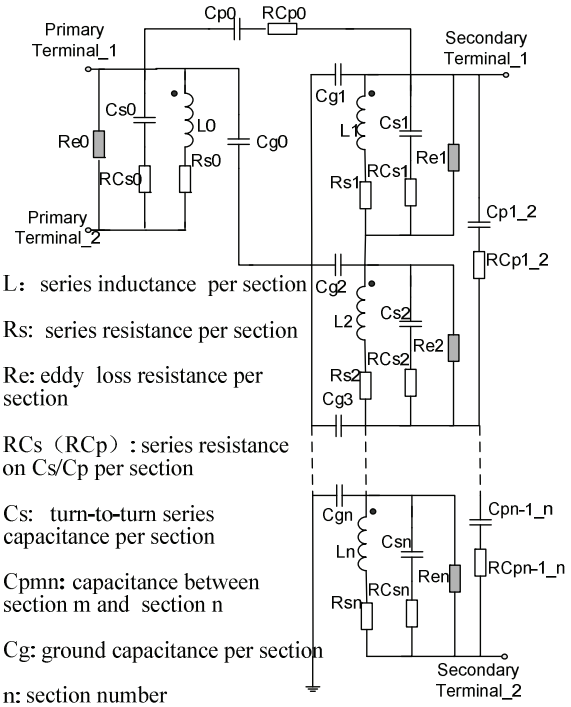

L: series inductance per section

Rs: series resistance per section

Re: eddy loss resistance per section

RCs (RCp): series resistance on Cs/Cp per section

Cs: turn-to-turn series capacitance per section

Cpmn: capacitance between section m and section n

Cg: ground capacitance per section

n: section number

Fig. 2. Equivalent circuit model of ignition coil.

Figure 2 shows the equivalent circuit model. This model separates the winding into individual sections. Each section of the circuit consists of capacitance C, inductance L and resistance R. Ten sections were used in this model.

III. FEA CALCULATION FOR PARAMETERS

A. Capacitance Cg and Cpmn

For calculating the ground capacitance Cg and the section-to-section capacitance Cpmn, simplified solid winding substituted the real winding section, as shown in Fig. 3 (a). *l*, *w* is length and width of a winding section. Calculating the capacitance from FEA is related to the electrostatic energy W^e. The first step is to assign a voltage U_i to the winding section *i*; all other winding section in the volume V are grounded. FEA programme discretizes problem volume V into tetrahedral element, as shown in Fig. 3 (b) (205007 tetrahedrons in total), and then solves the Laplace equation to get the electric field $\mathbf{E}_i$ and the displacement field $\mathbf{D}_i$ according to (1).

$$\nabla\cdot(\varepsilon\nabla\Phi_i)=0;\ \mathbf{E}_i=-\nabla\Phi_i;\ \mathbf{D}_i=\varepsilon\mathbf{E}_i \qquad (1)$$

Where, Φ_i is the electric scalar potential. The same procedure is applied to other conductor *j* in succession; in the end, W^C_{ij} can be obtained from (2). The computation time is about 115 minutes (Memory 2GB, CPU Frequency 2.19GHz).

$$W^C_{ij}=\frac{1}{2}\int_V \mathbf{E}_i\cdot\mathbf{D}_j\,dV=\frac{1}{2}\int_V \mathbf{E}_j\cdot\mathbf{D}_i\,dV \qquad (2)$$

Since the energy can also be expressed

$$W^C_{ij}=\frac{1}{2}C_{ij}U_iU_j \qquad (3)$$

Further combining the (2) and (3), we can get C_{ij}, which is one element in capacitance matrix. When $i\neq j$, section-to-section capacitance Cp_{ij} is equal to C_{ij}; when $i = j$, ground capacitance Cg can be written as

$$Cg_i = C_{ij} - \sum_{i\neq j} C_{ij}\cdot \qquad (4)$$

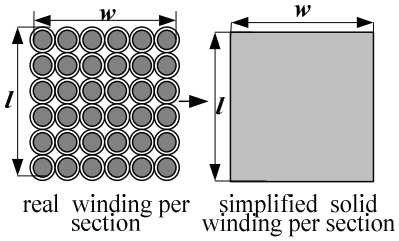

(a)

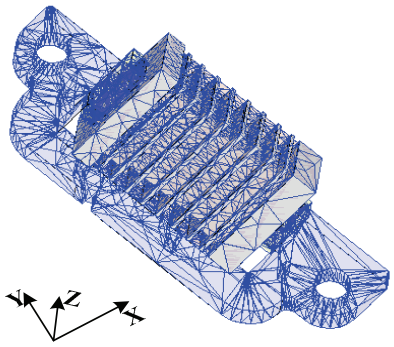

(b)

Fig. 3. Simplified solid model of real winding and 3D FEA mesh.

B. Capacitance Cs

For calculating the turn-to-turn series capacitance Cs of each winding section, the 3D geometry of each winding section is converted into an approximate 2D axis-symmetrical geometry. In this case, a simplified multi-layer sheet winding substitutes the real winding section, which omits the turn-to-turn capacitance in each layer of winding, as shown in Fig. 4 (a). The real winding is wound with round copper wire of diameter d_1 and overall wire diameter d_0; sheet winding is wound with rectangle conductor of length l and width u; h is the space between two layers. To guarantee that the cross-sectional area of the sheet winding is equal to that of the real winding, they have the following relations.

$$u = \frac{m\pi\left(\frac{d_1}{2}\right)^2}{l} \tag{5}$$

$$h = d_0 - d_1 \tag{6}$$

where m is the wire number in each layer of the real winding. FEA can be used to calculate the capacitance matrix, as mentioned in *A*, for the interaction between all the layers of sheet winding section. The computation time is about 3 minutes for each winding section. Figure 4(b) shows the triangular element when the layer number is 30 (25834 triangles in total). To this end, the electrostatic energy $W^C_{section}$ for a configuration of *N*-layer of winding, each excited with an applied potential, is given as

$$W^C_{section} = \frac{1}{2}\sum_{i=1}^{N}\sum_{j=1}^{N} C_{ij} U_i U_j \tag{7}$$

where U_i and U_j respectively represent the excited voltage to the layer i and the layer j of sheet winding. A modelling assumption is that the voltage difference (ΔU) between any two adjacent layer of winding is the same, so

$$U_i = i\Delta U, \quad U_j = j\Delta U \tag{8}$$

The stored energy $W_{section}$ can also be defined by the relation

$$W^C_{section} = \frac{1}{2} C_s U^2_{total} \tag{9}$$

where $U_{total} = (N-1)\Delta U$

Thus the series capacitance Cs in terms of all the layer-to-layer capacitance C_{ij} is

$$Cs(N) = \frac{\sum_{i}^{N}\sum_{j}^{N} ij C_{ij}}{(N-1)^2} \tag{10}$$

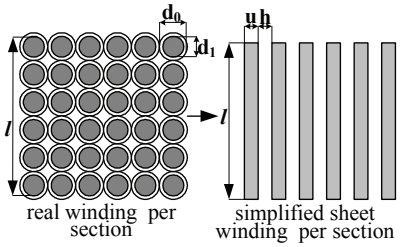

(a)

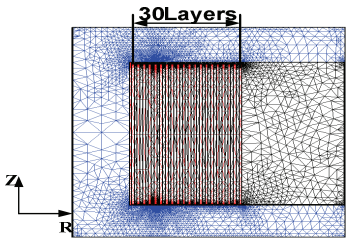

(b)

Fig. 4. simplified sheet model of real winding and 2D FEA mesh.

C. Inductance

In this work, the magnetic saturation phenomenon is ignored. Thus constant permeability μ, in the linear part of B-H curve, substitutes the varying steel property. The inductance of a set of winding sections can be calculated with the static magnetic store energy W^L, in analogy with the determination of capacitance from electric energy W^C. The procedure also depends on the FEA program to solve (11) for getting magnetic field $\mathbf{H}_i$ and magnetic flux density $\mathbf{B}_i$, which are corresponding to excitation with current I_i in winding section i, while the current excitations in the other winding section are zero. The same procedure is applied to other windings j in succession. The calculated energy in volume V can provide the self inductances (i=j) and mutual inductances ($i \neq j$), when combining (12) and (13). If the winding section i and j are, respectively, structured by N_i-turn and N_j-turn coil, the inductance L_{ij} can be obtained from (14).

$$\nabla \times \mathbf{H}_i = \mathbf{J}_i;\ \nabla \cdot \mathbf{B}_i = 0;\ \mathbf{B}_i = \mu \mathbf{H}_i \tag{11}$$

$$W_{ij}^{L} = \frac{1}{2}\int_V \mathbf{H}_i \cdot \mathbf{B}_j \, dV = \frac{1}{2}\int_V \mathbf{H}_j \cdot \mathbf{B}_i \, dV \tag{12}$$

$$W_{ij}^{L} = \frac{1}{2} L_{ij\_norm} I_i I_j \tag{13}$$

$$L_{ij} = N_i N_j L_{ij\_norm} \tag{14}$$

In reality, since the high frequency magnetic flux is difficult to enter inside the core of the transformer, the values of self and mutual inductances decrease as the frequency increases [8]. In order to study the impact of frequency on the magnetic flux, we adopted the magnetic scalar potential Ω in the whole domain and a current vector potential $\mathbf{T}$ in the conducting region to solve the eddy-problem. Applying Ampere's law, Faraday's law, and Gauss's law to the solenoidality of flux density yields two differential equations in conducting region as

$$\nabla \times \frac{1}{\sigma}(\nabla \times \mathbf{T}) = -j\omega\mu(\mathbf{T} - \nabla\Omega) \tag{15}$$

$$\nabla \cdot (\mu \mathbf{T}) = \nabla \cdot (\mu \nabla \Omega) \tag{16}$$

Here μ is the permeability, ω is angular frequency. In non-conducting region, the equation reduces to

$$\nabla \cdot (\mu \nabla \Omega) = 0 \tag{17}$$

The FEA program discretizes the problem region into tetrahedral elements, and by applying the Galerkin's approach, the discretized equation can be obtained [9]. After calculating the $\mathbf{T}$ and Ω of the nodal values, the magnetic flux density can be written as

$$\mathbf{B} = \mu(\mathbf{T} - \nabla\Omega) \tag{18}$$

In this work, we applied the unit current of 0Hz, 100Hz, 1kHz and 10kHz to the winding of the ignition coil. The magnetic lines of force in the core of the two-dimensional cross section are shown in Fig. 5; most of the magnetic line passes through the core when the frequency is 0Hz (static magnetic analysis) as shown in Fig. 5 (a); while as the frequency increases, the magnetic lines in the core significantly reduce when taking into account the skin effect and proximity effect, as shown in Fig. 5 (b), (c), and (d).

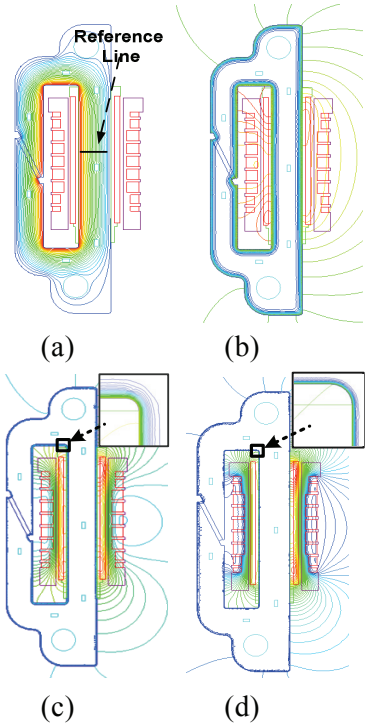

Fig. 5. Magnetic flux distribution of ignition coil at different frequencies at (a) 0Hz, (b) 100Hz, (c) 1kHz, and (d) 10kHz.

Figure 6 shows the flux as a function of core radius. B/B_{DC} is the relative value of static magnetic flux density on the reference line in

Fig. 5 (a); L/L_0 is relative position of the reference line; here, L_0 is the length of reference line. At 10kHz the magnetic flux within the transformer core is most completely displaced out of the core. Hence, when the frequency is above 10kHz, the core of ignition coil can be assumed as air or magneto-resistive material. In order to calculate the inductance matrix at low or high frequency with static magnetic analysis, relative permeability μ_r=2800 is defined for low frequency range, and the inductance matrix is defined as $\boldsymbol{L}_L$; while μ_r=0.001 is for high frequency range, and in this case the inductance matrix is defined as $\boldsymbol{L}_H$, as shown in Fig. 7.

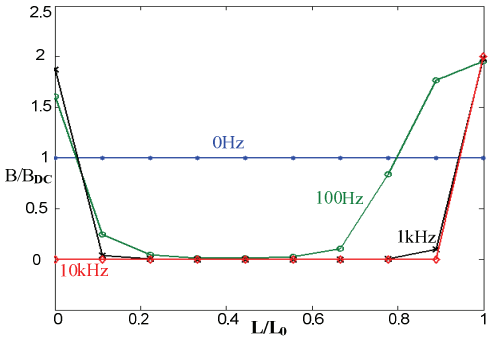

Fig. 6. Relative magnetic flux density value on the reference line.

D. Resistance

The winding resistance Rs/l =8.85Ω/m for the wire is used in this case. The effective resistance is expected to be larger because of the skin and proximity effect, but due to the small impact on the overall impedance of winding, this solution is considered sufficient. RCs/RCp represents the capacitance dielectric loss and its calculation equation is

$$RCs(f)/RCp(f) = \frac{tg\gamma}{2\pi fC} \qquad (20)$$

Here, tgγ is the dielectric loss tangent; C is the series capacitance value. In [6], the power factor of the capacitance circuit can be expressed by three different models, and the equivalent frequent point is determined by the intersection of power factor curves from the three models. The eddy current loss resistance Re is calculated based on [10], which does not generally change the overall shape of impedance curve of winding, but only influence the maximum limits.

IV. SIMULATION AND EXPERIMENT

A. Frequency-Domain

To investigate the secondary winding terminal impedance response from 100Hz to 10MHz, the following simulation cases were studied: Case (A), low frequency inductance matrix LL is adopted as series inductance L; Case (B), high frequency inductance matrix LH is adopted as series inductance L; Case (C), ignoring the turn-to-turn series capacitance Cs. As shown in Fig. 8, in case (A), the simulation matches well with the measurement from 100Hz to 10MHz. In case (B), the simulation partly agrees with the measurement from 80kHz to 10MHz. From the plots of case (A) and (B), inductances of winding convert from the LL to LH above 80 kHz; but the plot of (A), adopting the LL, agrees well with the measurement in the whole frequency domain; this phenomenon shows that the inductance does not influence the overall impedance in high frequency. In case (C), the simulation partly agrees with the measurement from 100Hz to 15kHz, which means the impedance of ignition coil above 15kHz is mainly decided by the capacitance of the winding. The measured data was got by impedance analyzer-Agilent4294A.

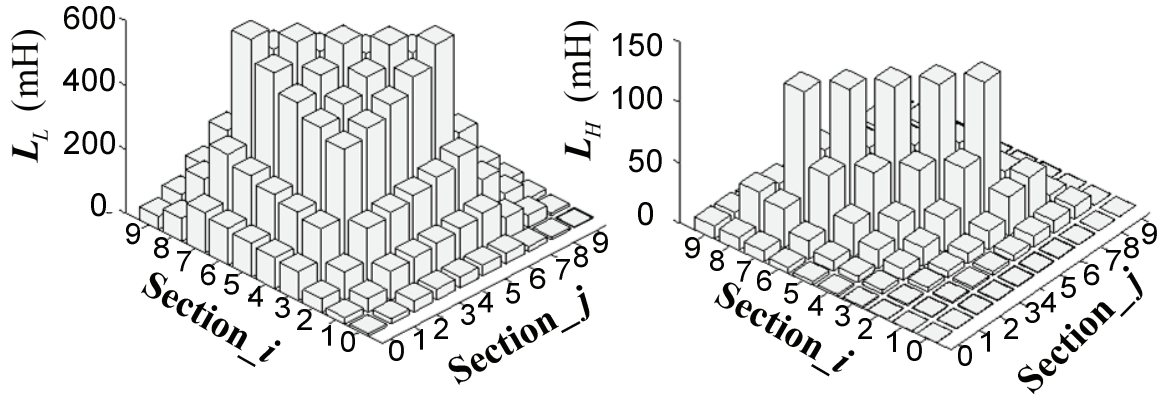

Fig. 7. Inductance Matrix in low-frequency (left) range and high frequency range (right).

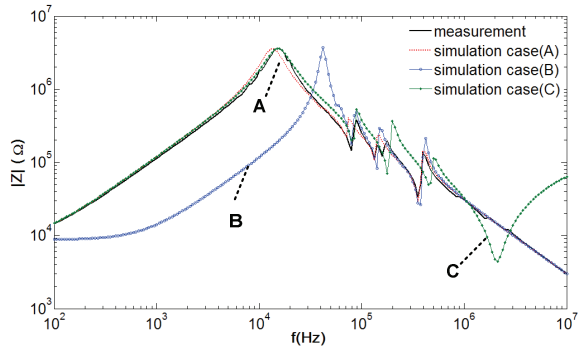

Fig. 8. Measured and simulated magnitudes of secondary winding impedance.

B. Time-Domain

In time-domain simulation, we used the case (A) to investigate the transient response of ignition coil. Fig.9 shows the transient voltage test circuit principle. The test equipments include: High-voltage probe Tektronix P6015A, Current probe Agilent 1146A, Oscilloscope Tektronix MSO 4032 and Waveform generator Agilent 33220A.

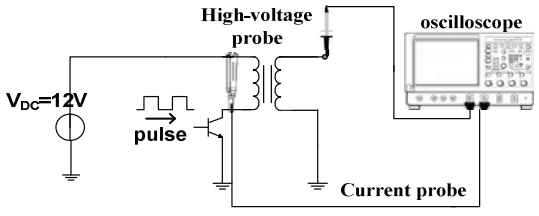

Fig. 9. Time-domain test circuit principle of ignition coil.

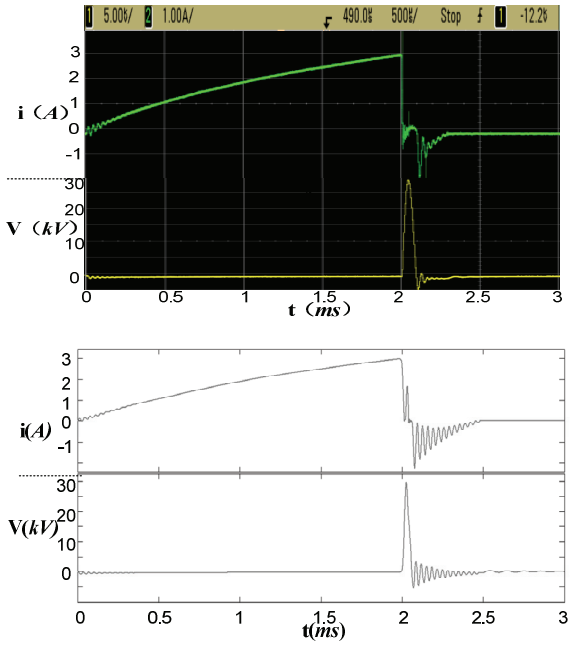

Fig. 10. Measured (upper) and simulated (lower) current of primary winding and voltage of secondary winding.

The primary winding current and secondary winding voltage are measured and simulated, as shown in Fig. 10. At t=0ms, at the opening of the switch device, the primary current waveform and secondary voltage waveform have small oscillation due to the inductance and capacitance in the ignition coil. In the interval 0ms < t < 2ms, the primary current is approximately linearly increasing to maximum value of 3A, and the

secondary voltage switches to zero. At t=2ms, at the closing of the switch device, the high changing rate of primary current induces high-voltage pulse of amplitude of 30kV in secondary winding. And for t>2ms, the primary current shows damped ringing around average value of -1A, while the secondary voltage shows damped ringing around average value of 0V. The simulation agrees well with the main part of waveform of the measurement.

V. CONCLUSION

This paper presented an equivalent lumped circuit model for predicting the wideband characteristic of automotive ignition coil. The main parameters in the circuit were calculated with FEA. In addition, FEA provides the approach to analysis the impact of frequency on the magnetic flux in the core. This circuit model was validated by experiment in both frequency and time domains, and those simulations agreed well with measurements.

ACKNOWLEDGEMENT

This work was supported in part by the National Natural Science Foundation of China (No. 50877081) and in part by the Third Stage Training of the "211 Project" of Chongqing University (No. S-09111).

REFERENCES

[1] B. Rohwein and B. Camilli, "Advanced automotive ignition system", *Digest of Technical Papers-IEEE International Pulsed Power Conference,* vol. 1, pp. 40-45, 1995.

[2] P. Ying, R. Jiangjun, Z. Yu, et al., "Calculation of very fast transient voltage distribution in pulse transformer", *Proceedings of the CSEE,* vol. 25, no. 11, pp. 140-145, 2005.

[3] M. Popov, L. van der Sluis, and. J. L. Roldan, "Analysis of Very Fast Transients in Layer-Type Transformer Windings", *IEEE Transactions on Power Delivery,* vol. 22, no. 1, pp. 238-247, 2007.

[4] J. Biernacki and D. Czarkowski, "High Frequency Transformer Modeling", *IEEE International Symposium on Circuit and Systems,* vol. 3, pp. 676-679, 2001.

[5] M. A. Eldery, Saadany, and Salama, "Parameters Identification of Sectional Wingding High Frequency Transformer Model Using Neural Network", *IEEE International Symposium on Micro-Nanomechatronics and Human Science,* vol. 2, pp. 974-977, 2005.

[6] M. T. Yoshikazu and T. Teranishi, "Modeling and Analysis of Transformer Winding at High Frequencies", *The International Conference on Power Systems Transients (IPST05),* 2005.

[7] M. Wang, A. John Vandermaar, and K. D. Strivastava, "Improved Detection of Power Transformer Winding Movement by Extending the FRA High Frequency Range", *IEEE Transactions on Power Delivery,* vol. 20, no. 3, pp. 1930-1938, 2005.

[8] A. M. Miri, N. A. Riegel, and Andreas, "Finite Element Models For the Computation of the Transient Potential and Field Distribution in the Winding System of High Voltage Power Transformers," *IEE Conference Publication,* vol. 2, pp. 467, pp. 39-42, 1999.

[9] P. Zhou,W. N. Fu, D. Lin, S. Stanton, and Z. J. Cendes, "Numerical modeling of magnetic devices," *IEEE Trans. Magn.*, vol. 40, pp. 1803–1809, July 2004.

[10] J. Benecke and S. Dickmann, "Analytical HF Model for Multipole DC Motors", *Proceedings of the 18th international Zurich Symposium on Electromagnetic Compatibility,* pp. 201-204, 2007.

Jia Jin was born in Si Chuan Province, China in 1985. Since 2007, he has been pursuing his M.S degree at the college of electrical engineering in Chongqing University, China. His areas of interest are electro-magnetic computation and electromagnetic compatibility.

Wang Quandi was born in Anhui province, China in 1954. She received her Ph.D degree from the College of Electrical Engineering of Chongqing University, Chongqing, China, in 1998. Currently, she is a professor in the college of Electrical Engineering, Chongqing University. Her main research interests are simulation and numerical computation of electromagnetic fields.

Yu Jihui was born in Changsha, Hunan province, China in 1944. Now, he is Professor of the College of Electrical Engineering at Chongqing University in China. His main research interests are the numerical computation and simulation of electromagnetic fields and electromagnetic compatibility, and also in the information management system field.

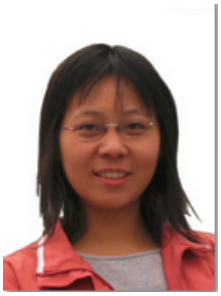

Zheng Ya-li was born in Henan Province, China in 1982. She received the B.S. degree in electrical engineering from Chongqing University, Chongqing, China, in 2005, where she is pursuing her Ph.D. degree in electrical engineering. Her research interests include electromagnetic computation, electromagnetic compatibility and transmission-line analysis.

Design and Simulation of Frequency-Selective Radome Together with a Monopole Antenna

Baoqin Lin, Sishen Du, Huanmei Zhang, Xiangyan Ye

Institute of Telecommunication and Engineering,
Engineering University of Air Force
Xi'an, 710077, P. R. China
aflbq@sina.com

Abstract- In this paper, we present a novel axi-symmetric conical FSS radome at S-band and investigate the effect of the FSS radome located in close proximity of a monopole antenna. The strict periodic array of the novel FSS radome was indicated in detail, and the FSS radome together with a monopole antenna was simulated using the Ansoft software HFSS both at the pass and stop bands. The simulated results show that the novel FSS radome has a narrow band-pass response and is prospectively useful for out-of-band RCS control.

Index Terms- Frequency selective surfaces, FSS, Radome.

I. INTRODUCTION

Frequency selective surfaces (FSS) have attracted considerable attention in telecommunications, antenna design, and electromagnetic compatibility for several decades. The investigation of FSS has been the subject of much fruitful study [1-6]. They have been proposed to be used as polarizers, space filters, sub-reflectors in dual frequency antennas, and antenna radomes for radar cross section (RCS) control [3].

As a radome, the FSS is curved and has non-planar illumination. Because the FSS radome is often designed as a large structure, the approximate locally planar technique (LPT) method has been used to determine the scattering from a large FSS radome [4]. This LPT involves dividing the surface into a number of subarrays, each of which is assumed to be a segment of an infinite planar surface. The infinite FSS theory with plane wave illumination is applied to analyze each subarray.

In this paper, we propose a novel small FSS radome at S-band, which is mounted on sharp conical surface, and the strict periodic array of the FSS radome is indicated in detail. The FSS radome, together with a monopole antenna, is to be analyzed. Because the FSS radome is located in close proximity to a monopole antenna, and the whole structure is not too large and can be effectively simulated using the Ansoft software HFSS. The influence of the small FSS radome on the radiation of a monopole antenna is investigated by comparing the antenna radiation with the FSS radome present or not.

II. DESIGN

A FSS radome is a periodic array mounted on a curved surface. Firstly, we try to design the configuration of its unit cell. According to the narrow band-pass response of the known FSS based on the aperture coupled microstrip patches [5-6], its unit cell is chosen as two back-to-back circular patches laid on the surface of two dielectric slabs sharing a common ground plane, and one small crossed slot is set up on the ground plane to couple the fields from one patch to the other.

After the unit cell is chosen, the periodic array is established. For a miniature FSS radome, its curved surface has a much higher surface curvature, and a strict periodic array mounted on the sharply curved surface is difficult to construct. After much thought, we choose the FSS radome as a conical structure. This design is based on a novel axi-symmetric planar FSS. The geometry of the devised axi-symmetric planar FSS, as well as the chosen unit cell, are shown in Fig. 1.

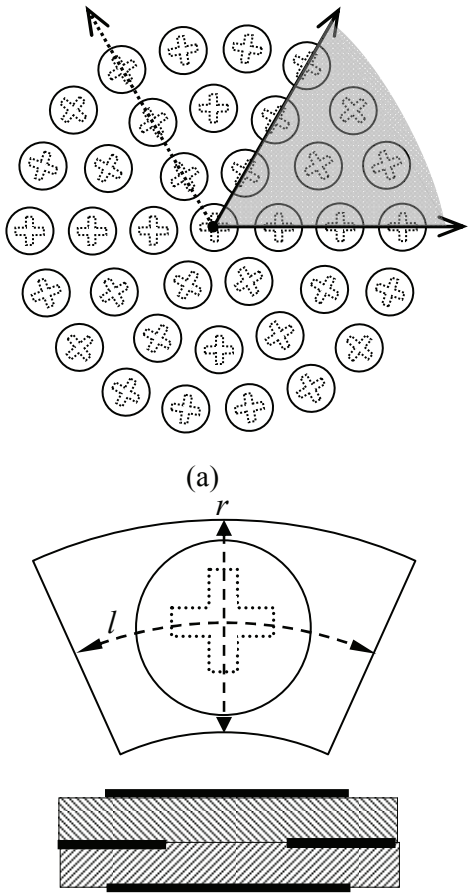

Fig. 1. Geometry of an axi-symmetric planar FSS using aperture coupled patches. (a) Top view; (b) Unit Cells.

For the axi-symmetric planar FSS, the area of one unit cell is fan-shaped and its size is defined by two parameters, the length of the center arc l and the radius r, as shown in Fig. 1(b). To keep the axi-symmetry of the FSS, the ratio of the radius r to the center arc l shall be chosen as some fixed values, now we select it as:

$$\frac{r}{l}=\frac{3}{\pi}.$$

In this way, the made-up FSS is just an axi-symmetric structure which is made up of six large pie slices, as shown in Fig. 1(a).

Now a novel axi-symmetric conical FSS radome can be constructed when one or two large pie slices of the axi-symmetric planar FSS are taken out and the left structure is circled around the center axis. When one large pie slice is taken out, the obtained FSS radome is named FSS radome A; when two large pie slices are taken out, a much sharper FSS radome B is obtained.

III. SIMULATED RESULTS

As an axi-symmetric structure, the small conical FSS radome can be simulated using the FDTD method in three-dimension cylindrical coordinates. We use Ansoft software HFSS to simulate it as a simple method.

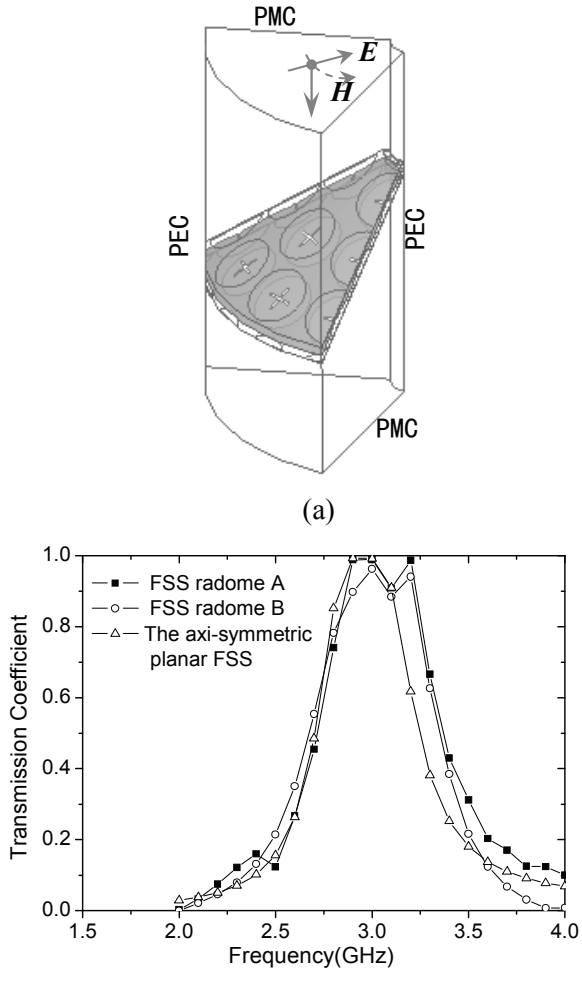

Fig. 2. Three dimensional simulated model of the FSS radome (a) and the simulated transmission coefficients (b).

After a series of simulations, we choose the structural parameters of the unit cell as follows: the radius of fan-shaped cell is r = 22.0*mm*, the radius of two

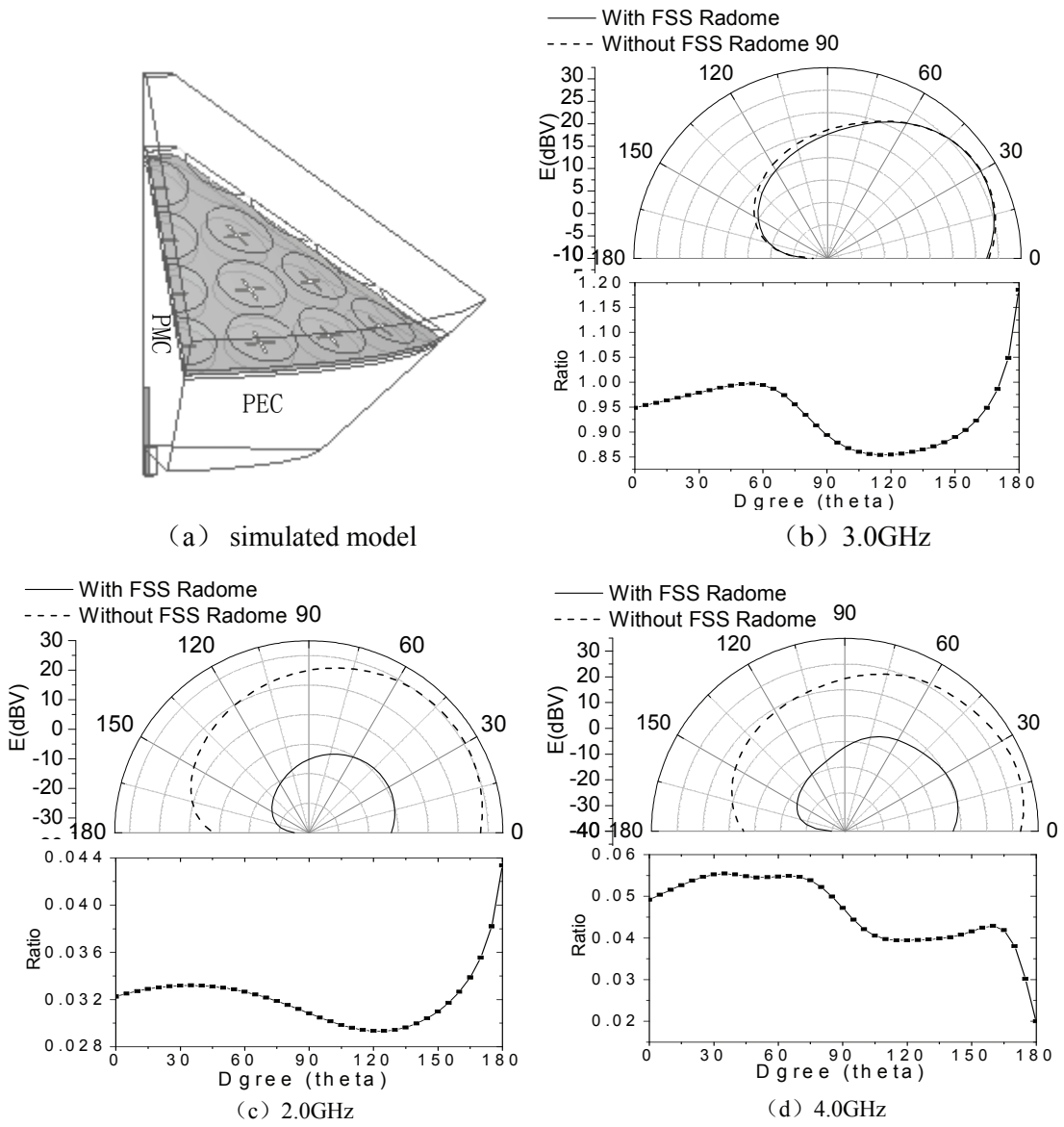

Fig. 3. Three dimensional simulated model of the FSS radome A with a monopole antenna (a) and the simulated results at three frequencies3.0GHz (b),2.0GHz (c) and 4.0GHz (d).

back-to-back circular patches are all 10.0*mm*, the crossed slot on the ground plane contains two vertical rectangular gapes with the width 0.8*mm* and the length 9.0*mm*, the thickness of two dielectric slabs is 2.0*mm* and their dielectric constants are chosen as $\varepsilon_r = 6.0$.

The band-pass response of the conical FSS radome was analyzed first. According to its axi-symmetry, we pose the FSS radome into a large coaxial cable, and only choose one large pie slice as the simulated structure, as shown in Fig. 2(a). The analyzed transmission coefficients of the axi-symmetric planar FSS and the conical FSS radome are shown in Fig. 2(b). It is shown that the transmission coefficients have changed little when the axi-symmetric planar FSS was changed as the conical FSS radomes A and B. The desired narrow pass band response have been detected for all cases.

The conical FSS radome together with an antenna is simulated in succession. To keep the axi-symmetry of the whole structure, a monopole

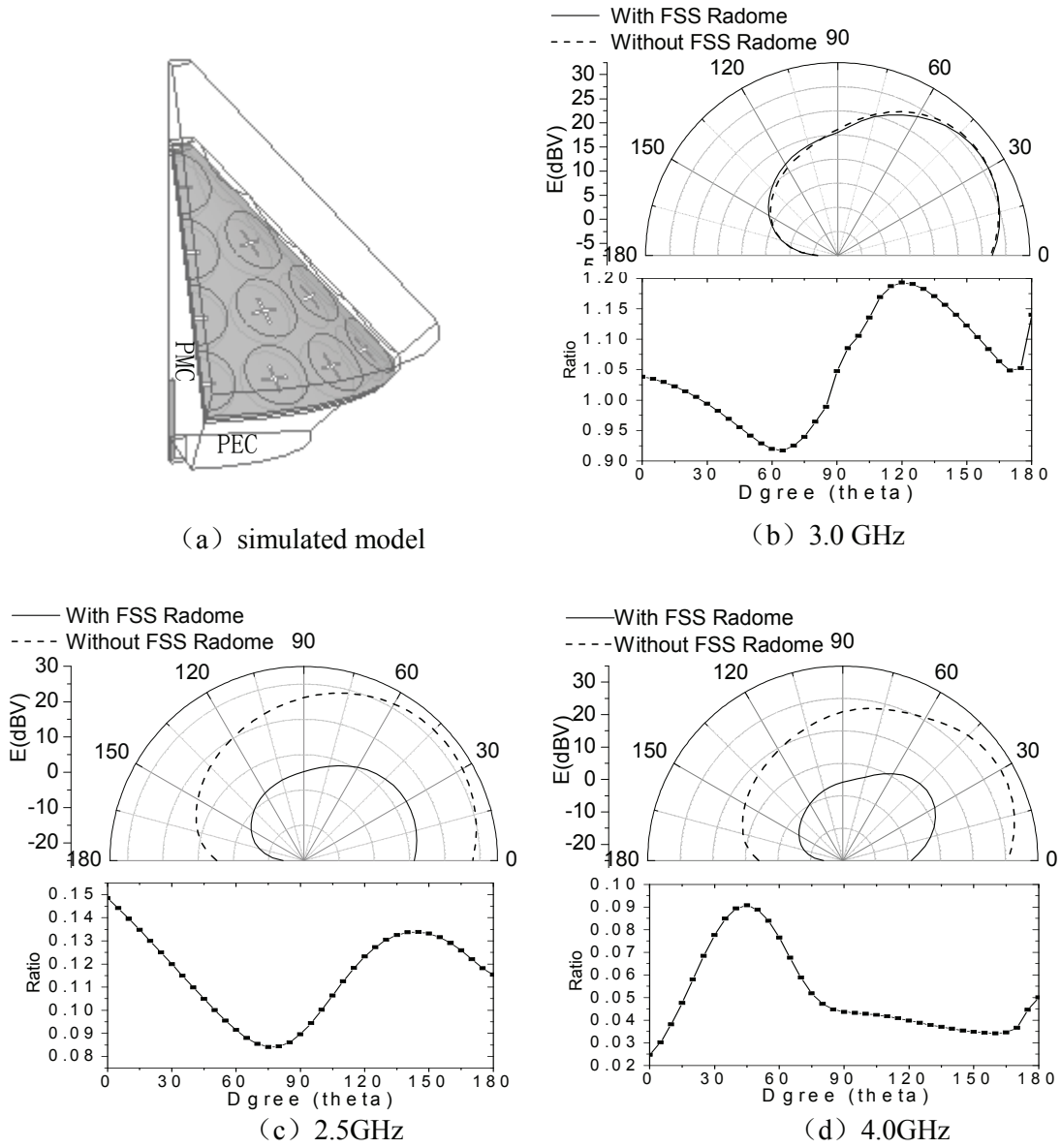

（a）simulated model （b）3.0 GHz

（c）2.5GHz （d）4.0GHz

Fig. 4. Three dimensional simulated model of the FSS radome B with a monopole antenna (a) and the simulated results at the three frequencies 3.0GHz (b), 2.5GHz (c) and 4.0GHz (d).

antenna is selected and laid on the center axis of the conical FSS radome. In this way, we can separate one large pie slice from the whole structure using PMCs as the simulated structure.

Firstly, for the FSS radome A, the simulated structure is shown in Fig. 3(a). The radiation of the monopole antenna has been effectively simulated at three frequencies 2.0GHz, 3.0GHz, and 4.0GHz when the FSS radome A is presented or not. In the simulated results, these radiate electric fields in the middle longitudinal dissected plane of the simulated structure, as well as the ratio of the radiate fields in the presence of FSS radome A to that of the same antenna in the absence of the radome A, are shown in Fig. 3(b), (c) and (d).

At a frequency of 3.0 GHz which is in the pass band of the FSS radome A, the length of the monopole antenna is 25.0 mm. The data in Fig. 3(b) show that the FSS radome has little effect on the radiation of the monopole antenna, and the ratio is all close to 1.0 when the observation angle

varies from 0 degrees to 180 degrees. While at frequencies of 2.0GHz and 4.0GHz, which are both in the stop band of the FSS radome A, the length of the monopole antenna is changed to 37.5 mm and 18.7 mm, respectively. The simulated results in Fig. 3(c) and (d) show that the radiation of the monopole antenna has been controlled in all directions because of the placement of the FSS radome A, as the ratio is reduced to -25~-35dB. It is verified that the FSS radome A has a desired band-pass response and will be prospectively useful for out-of-band RCS control.

Secondly, a similar process of simulations for the FSS radome B has been executed at the three frequencies: 2.5GHz, 3.0GHz, and 4.0GHz. The simulated structure and acquired results are shown in Fig. 4. According to the simulated results, the desired band-pass response of the FSS radome B has been effectively verified in the same way.

Finally, we combine the conical FSS radome A with a cylindrical FSS as a novel FSS radome. The unit cell of the cylindrical FSS is the same as that of the conical FSS. The longitudinal period is

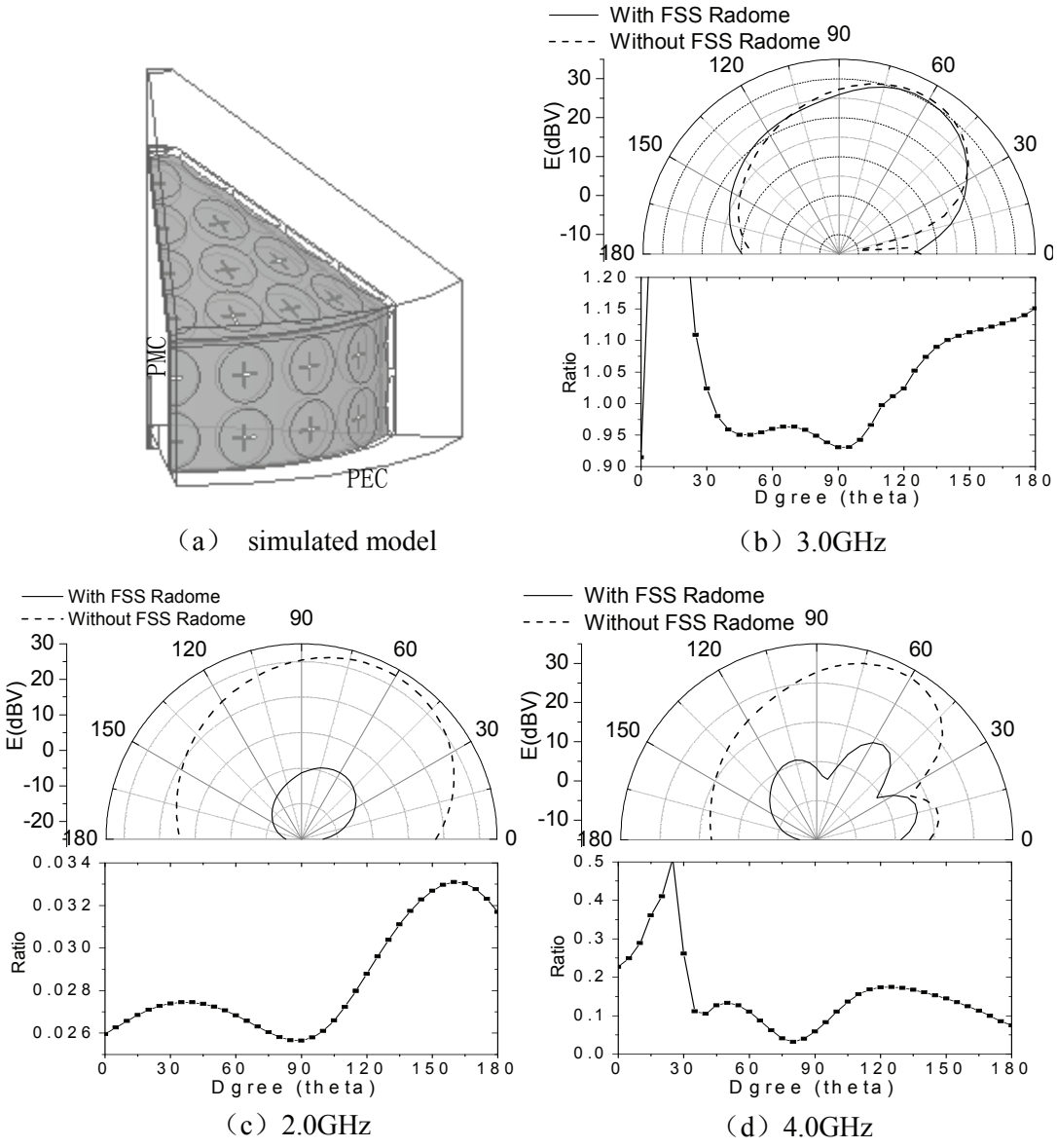

Fig. 5. Three dimensional simulated model of the novel FSS radome with a monopole antenna (a) and the simulated results at three frequencies3.0GHz (b), 2.0GHz (c) and 4.0GHz (d).

kept as 22.0mm, and the transverse period is changed to 24.9mm to keep the axi-symmetry of the whole structure. The simulated structure combined with the novel FSS radome with a monopole antenna is shown in Fig. 5(a), and the simulated results at three frequencies 3.0GHz, 2.0GHz, and 4.0GHz are shown in Fig. 5(b), (c) and (d), respectively. As the placement of the novel FSS radome, the data in Fig. 5(d) show that the reduction of the antenna radiation at 4.0GHz is relatively low in some directions, while the ratio is close to -20dB in most directions. The band-pass response of the FSS radome can still be seen.

IV. CONCLUSION

A novel axi-symmetric conical FSS radome was proposed in this paper. Its design was based on a novel axi-symmetric planar FSS, and its structure was described in detail. The effect of the proposed structure is effectively simulated with a monopole antenna using the Ansoft software HFSS. The simulated results showed that the novel FSS radome has a narrow band-pass response and is prospectively useful for out-of-band RCS control.

REFERENCES

[1] T. K. Wu, *Frequency Selective Surface and Grid Array, John* Wiley& Sons, Inc, 1995.

[2] B. Munk, *Frequency Selective Surfaces: Theory and Design,* John Wiley & Sons, Inc., 2000.

[3] R. Mittra, C. C. Chan, and T. Cwik, "Techniques for analyzing Frequency Selective Surfaces: A Review," *Proc. IEEE,* vol. 76, no. 12, pp. 1593–1615, 1988.

[4] A. Caroglanian and K. J. Webb, "Study of curved and planar Frequency Selective Surfaces with nonplanar illumination," *IEEE Trans. Antennas Propagat.,* vol. 39, no. 2, pp. 211–220, 1991.

[5] R. Pous and D. M. Poxar, "A frequency selective surfaces using aperture-coupled microstrip patches," *IEEE Trans. Antennas Propagat.,* vol. 39, no.12, pp. 1763–1770, 1991.

[6] A. A. Tamijani, K. Sarabandi, and G. M. Rebeiz, "Antenna–Filter–Antenna Arrays as a Class of Bandpass Frequency-Selective Surfaces," *IEEE Trans. Microwave Theory and Techniques,* vol. 52, no.8, pp. 1781-1790, 2004.

Baoqin Lin was born in Hunan, China, in 1976. He received his M.S. degrees in microwave theory and techniques from Air Force Engineering University, Xi'an, China, in 2002, and the Ph. D. degree in 2006 from National University of Defense Technology, Changsha.

He is currently engaged in research in Air Force Engineering University, His research interests include the analysis of frequency selective surfaces, electromagnetic bandgap materials and stealth technology.

Sishen Du was born in Shanxi, China, in 1962. He is associate Professor in Air Force Engineering University. His research interests are in microwave circuits and antennas, electromagnetic scattering. He also interested in the analysis of frequency selective surfaces.

Subtraction of Discontinuity Susceptance for WIPL-D Source Modeling

Hossam A. Abdallah, Wasyl Wasylkiwskyj

Department of Electrical & Computer Engineering
The George Washington University
Washington DC 20037 USA
hossam@gwu.edu, wasylkiw @gwu.edu

Abstract- WIPL-D does not include a provision for a direct specification of a coaxial line excitation of patch antennas in terms of the incident dominant TEM mode. Instead, such an excitation is approximated by a voltage generator in series with a thin wire, one end of which is connected to the inner conductor of the coax and the other end to a flat shorting cap joined to the outer conductor. The transition from the diameter of the inner conductor to the diameter of the wire gives rise to a spurious capacitive shunt susceptance leading to an error in the calculated antenna input impedance. It is shown that this susceptance can have a significant effect on the WIPL-D calculations of the return loss of narrow band patch antennas. A computational technique is presented for neutralizing this modeling deficiency.

Index Terms- WIPL-D, narrow band patch antennas, return loss.

I. INTRODUCTION

WIPL-D is a program that allows modeling and analysis of metallic and/or dielectric/magnetic structures (antennas, scatterers, passive microwave circuits, etc.) [1]. We have used WIPL-D to design the coaxially fed patch antenna illustrated in Figure 1 (a). The cross section of the coax feed and patch antenna is shown in Figure 1(b). One peculiarity of WIPL –D is that it does not allow a direct coaxial line feed (e.g., a magnetic current sheet corresponding to the TEM coax mode electric field). Instead, auxiliary structures are employed at the input end to facilitate the injection of a voltage source. These are illustrated in Fig. 1 (c). One arrangement, shown in the upper portion of Fig.1(c), employs a thin short wire (length $r_0/4$, with r_0 is the radius of the inner conductor of the coax) that connects the inner conductor to the conducing back plate terminating the coax. An ideal voltage source is applied in series with the wire. We refer to this type of arrangement as an edge excitation. Alternatively, to provide a smoother transition from the coax inner conductor to the thin wire at the voltage source, several wires may be used, each connecting the voltage source with a wire to a side of a regular polygon approximating the cross section of the inner conductor of the coax. In WIPL-D at most 12 wire - to -plate junctions can be defined, which limits the modeling of the cross-section of a circular cylinder to a polygon with 12 sides. This second form of excitation is illustrated schematically in the lower portion of Fig. 1c).We shall refer to it as cone excitation.

As a result of the transition of the coax inner conductor to the voltage source both the edge and the cone excitations give rise to a shunt discontinuity susceptance. This susceptance is an artifact of the feed structure used to facilitate numerical calculations and would normally not be present when a real physical coaxial feed is employed. Using WIPL calculations for the input impedance of a patch antenna we investigate the effect of this susceptance and present a technique for neutralizing the resulting error.

Referring to the geometry of a single-layer patch antenna shown in Figure 1(a), the length of the patch L is 51.22 mm, the width is W, thickness of 35μm, and a substrate height h of 0.062 inches. The coaxial line feed point is located at x_r and y_r. A finite ground plane (dimensions u and v) is assumed. The dimensions and parameters of this design were chosen to obtain a patch antenna radiator in the 1895-1910 MHz band [2]. The specific parameter values are L= 51.22 mm, W=

60 mm, h=1.5748 mm, $\varepsilon_2 = 2.2(1 - i0.0004)$, x_r=0.35L, and y_r=W/2. The transmission line parameters are Length=2cm, r_0=0.635mm, r_1=2.0574mm, ε_1=2.07, and a ground plane size=(L+40h)*(W+40h) mm^2.

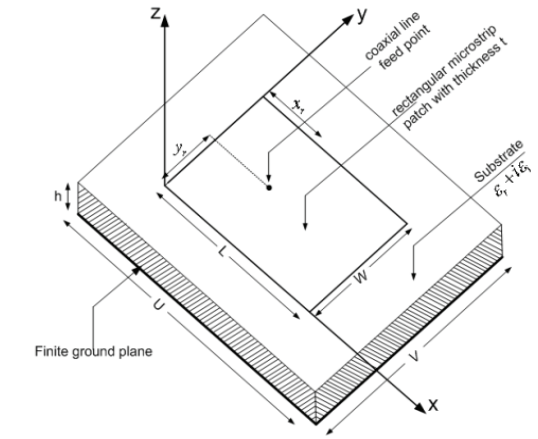

(a)

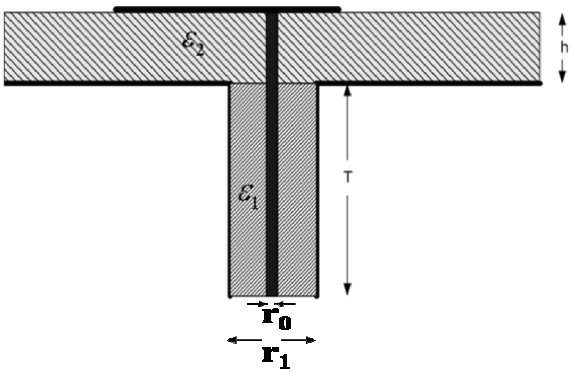

(b)

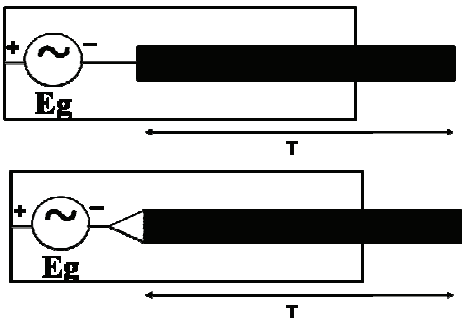

(c)

Fig. 1. Rectangular microstrip patch antenna (a), cut through the coax feed (b), and auxiliary feed structures (c).

II. CALCULATIONS OF RETURN LOSS WITH WIPL-D FOR DIFFERENT LENGTHS OF TRANSMISSION FEED LINE

In the following we present results of return loss calculations for the patch antenna in Fig. 1 for the cone and edge excitation options in WIPL-D described in the preceding.

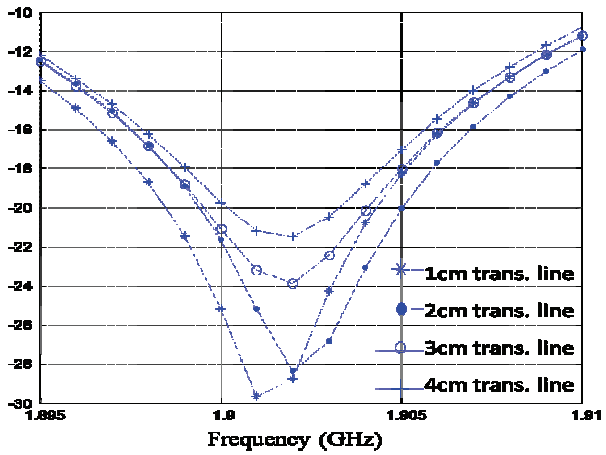

(a)

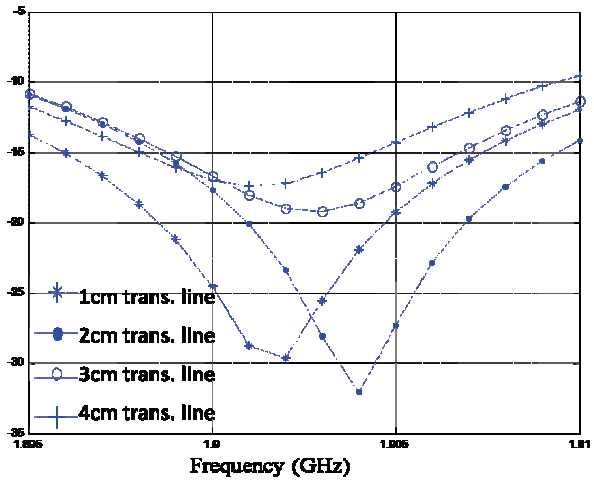

(b)

Fig. 2. Return loss (dB) of patch antenna for different transmission line lengths using cone-excitation (a), edge excitation (b).

Figure 2(a) shows plots of the magnitude of the input reflection coefficient as a function of frequency for the cone excitation for four different lengths of the input feed line. These large differences among the return loss response curves and changes of the effective resonance frequency are incompatible with the model of a transmission

line excited by an ideal voltage source, since in such a model different lengths of lossless feed lines can affect only the phase of the input reflection coefficient and not its magnitude. Similar effects are observed when an edge excitation is employed, as shown in Fig. 2(b). The reason for the variation of the return loss with the length of the feed line can be traced to the discontinuity susceptance introduced by the change of the inner conductor of the coax at the feed point, as discussed in following section.

III. SUBTRACTION OF DISCONTINUITY SUSCEPTANCE FOR WIPL SOURCE MODELING

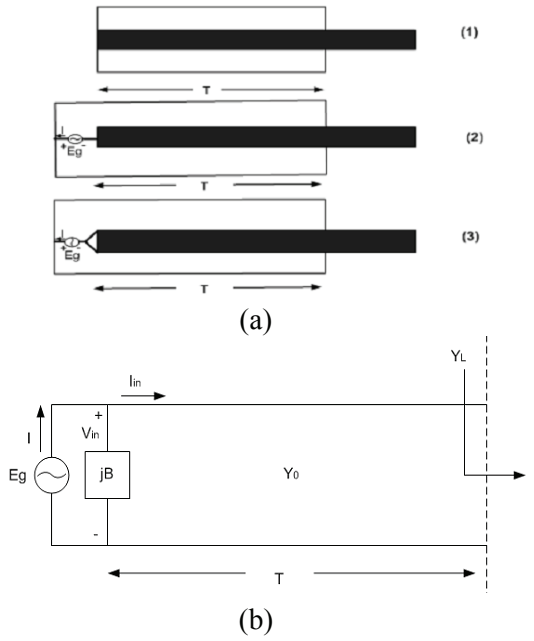

Fig. 3. The coaxial line feed models (a), equivalent circuit of a coaxial line feed in WIPL (b).

Despite the imperfection in modeling the coaxial line feed in WIPL-D, it is possible to correct the calculated input reflection coefficient by taking into account the effect of the shunt susceptance introduced by the wire excitation at the end of the coaxial line. Indeed, as discussed in the sequel, the correction technique generalizes to the S matrix of an array of patch antennas. Figure 3(a) shows three sketches of a coaxial line. The top is the ideal coaxial line that we would like to simulate, wherein an ideal voltage generator could be modeled exactly by a sheet of magnetic current inserted between the inner and outer conductor, representing the E field of the coaxial TEM mode. The two lower configurations represent excitations used in WIPL-D: the edge excitation, and the cone excitation. Because of the change in the diameter of the inner conductor both WIPL-D excitations deviate from an ideal voltage source. To a first approximation, the effect of the change in the diameter can be modeled as a capacitive shunt susceptance in which case the circuit representation of the coaxial transmission line feed assumes the form shown in Fig. 3(b). Although the magnitude of this susceptance could be obtained from a separate numerical calculation, it is simpler and of greater utility to be able to infer it directly from WIPL-D. Thus the input admittance Y computed by WIPL-D is the ratio

$$Y = \frac{I}{E_g} \tag{1}$$

with I the E_g defined in Figure 3, whereas the actual input admittance is given by

$$Y_{in} = \frac{I_{in}}{E_g} \tag{2}$$

or, equivalently, by

$$Y_{in} = Y - jB \tag{3}$$

The parasitic discontinuity susceptance B can be determined by running WIPL-D for two or more transmission line lengths as shown in the following development.

Using normalized quantities y_{in}, b, y, and y_L with Y_0 the characteristic impedance of the coax,

$$y_{in} = \frac{Y_{in}}{Y_0}, \quad y = \frac{Y}{Y_0}, \quad y_L = \frac{Y_L}{Y_0}, \quad b = \frac{B}{Y_0}, \tag{4}$$

$$y_{in} = y - jb \tag{5}$$

the normalized input admittance y_{inq} to the coaxial line with electrical length θ_q becomes

$$y_{inq} = \frac{y_L + j\tan\theta_q}{1 + jy_L\tan\theta_q} \tag{6}$$

where y_L is the normalized input admittance at a fixed reference plane, and $q = 1, 2, \ldots N$ refers to different choices of the length the coaxial line. For example, with $N = 2$

$$y_{in1} = \frac{y_L + j\tan\theta_1}{1 + jy_L\tan\theta_1} \tag{7}$$

$$y_{in2} = \frac{y_L + j\tan\theta_2}{1 + jy_L\tan\theta_2} \tag{8}$$

where

$$\theta_1 = \frac{2\pi f\sqrt{\varepsilon_r}}{c}T_1, \quad \theta_2 = \frac{\theta_1}{T_1}T_2 \tag{9}$$

Using the corresponding admittance calculated by WIPL-D y_1 and y_2 the input admittances (7) and (8) are

$$y_{in1} = y_1 - jb \tag{10a}$$

$$y_{in2} = y_2 - jb \tag{10b}$$

Subtracting, one obtains

$$\Delta y = y_{in1} - y_{in2} \quad = y_1 - y_2 \tag{11}$$

so that Δy is fixed from two WIPL-D calculations. Thus subtracting (7) and (8) and using (11) yields the following quadratic equation for y_L:

$$\alpha y_L^2 + \beta y_L + \gamma = 0 \tag{12}$$

where

$$\alpha = \tan\theta_2 - \tan\theta_1 - j\Delta y\tan\theta_1\tan\theta_2$$

$$\beta = -\Delta y(\tan\theta_1 + \tan\theta_2) \tag{13}$$

$$\gamma = \tan\theta_1 - \tan\theta_2 + i\Delta y$$

Only the root with the positive real part corresponds to the correct solution, which, upon substitution in (5), yields the susceptance *b*. Ideally, this should yield a purely real positive number since the susceptance is capacitive. However numerical errors will generally cause the answer to be complex. If the real part is positive and much larger than the imaginary part the imaginary part may be discarded. The accuracy can be improved by using $N > 2$ and solving an overdetermined system using least squares.

IV. RETURN LOSS FOR THE CORRECTED EDGE AND CONE EXCITATIONS

The preceding correction procedure was applied to both cone and sharp-edge excitations. Figure 4 shows plots of the return loss for three different lengths of the feed line. Comparing these plots with Fig. 2 we see that variation of return loss with changes in lengths has been reduced to less than 2dB. Note that the correction gives essentially the same results for the sharp-edge and cone excitations. Hence, the cone excitation offers no advantages over the sharp edge excitation.

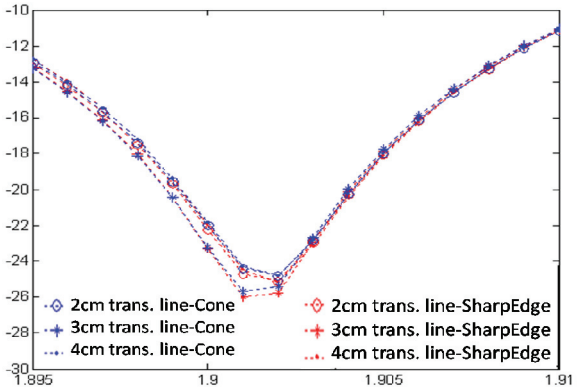

Fig. 4. Corrected return loss for both edge and cone excitations.

V. CONCLUSIONS

The WIPL-D source model for coaxial line feeds for patch antennas introduces a spurious discontinuity susceptance which can give rise to significant errors in the return loss calculations of narrow band patch antennas. A technique for subtracting this susceptance has been presented and illustrated by numerical examples.

REFERENCES

[1] B. Kolundzija, J. S. Ognjanovic, and T. K. Sakar, *WIPL-D: Electromagnetic Modeling of Composite Metallic and Dielectric Structures - Software and User's Manual*, Artech House, 2000.

[2] H. Abdallah, W. Wasylkiwskyj, K. Parikh, and A. Zaghloul, "Comparison of return loss calculations with measurements of narrow-band microstrip patch antennas," *The Annual Review of Progress in Applied Computational Electromagnetics Conference,* April 2004.

Hossam A. Abdallah was born in Alexandria, Egypt, in 1973. He received his PhD in Electrical Engineering in 2005 from the Dept. of Electrical and Computer Engineering, The George Washington University, Washington DC. His dissertation work and research activities are computational electromagnetics and array signal processing. Mr. Abdallah received his Bachelor of Science degree in computer science in 1995 from Alexandria University, Alexandria, Egypt. In 2001 he received his MSc degree in Engineering Mathematics from Twente University, Enschede, The Netherlands. Dr. Abdallah is currently working as resolution enhancement techniques design engineer at Intel.

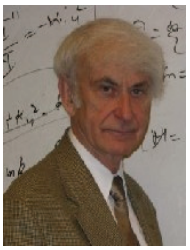

Wasyl Wasylkiwskyj (F'97) received his BEE degree from the City University of New York in 1957 and the MS and Ph.D. degrees in electrical engineering from the Polytechnic University in 1965 and 1968, respectively. His past research and industrial experience covers a broad spectrum of electromagnetics, including microwave components and techniques, phased array antennas, propagation and scattering, radar cross-section modeling as well as modeling of geophysical and oceanographic electromagnetic phenomena. In addition, he has extensive experience in ocean and structural acoustics with applications to active SONAR. Since 1985 Dr. Wasylkiwskyj has held the position of Professor of Engineering and Applied Science at the George Washington University, Washington, DC. His current research activities are primarily in numerical electromagnetics and array antennas for direction –of- arrival estimation.

Design of a Meander-Shaped MIMO Antenna Using IWO Algorithm for Wireless Applications

Batol Bahreini[1], Alireza Mallahzadeh[2], Mohammad Soleimani[1]

[1] Department of Electrical Engineering
Iran University of Science and Technology, Tehran, Iran.
bbahreini@ee.iust.ac.ir, soleimani@iust.ac.ir

[2] Department of Electrical Engineering
Shahed University, Tehran, Iran
mallahzadeh@shahed.ac.ir

Abstract ─ Using a MIMO antenna system is a well-known technique to enhance the performance of wireless communication systems. In order to create a MIMO antenna system on a wireless device, two or more antenna elements could be placed in a very small space. Thus, the mutual coupling including radiation pattern coupling between closely arrayed antenna elements causes the decrease of a MIMO antenna performance. It means that we must consider not only the antenna size but also the suitable antenna array method to design the MIMO antenna system. The aim of this research was to design an antenna for a four-channel multiple input multiple output (MIMO) system that works at 5.8 GHz with consideration of the mutual coupling. The geometry of the antenna is optimized by using Invasive Weed Optimization algorithm to accomplish high degree of isolation. The measurement and simulation results of reflection coefficient, mutual coupling and radiation pattern are presented and discussed.

Index Terms ─ Antenna, IWO algorithm, MIMO systems.

I. INTRODUCTION

Over the past few years, there has been an increasing worldwide research interest in multiple-input-multiple-output (MIMO) systems, also known as multiple-element antenna (MEA) systems, as they have been shown to have the potential for improved capacity, spectral efficiency and reliability as compared to single-antenna communication systems [1]. MIMO technology is a breakthrough in the field of modern wireless communications, and is poised to play a significant role in the implementation of next generation's wireless products and networks.

In order to study the performance of the MIMO antenna, some parameters need to be considered. Mutual coupling is one of the important factors because higher mutual coupling means lower antenna efficiency [3].

The correlation coefficient between the two antennas is another important parameter since it is associated with the loss of spectral efficiency and degradation of performance of a MIMO system [3]. Correlation of the signals at the different antenna elements can considerably decrease the capacity of a MIMO system [3]. Such correlation occurs particularly for compact MIMO systems, where the separation between the antennas is small; this effect has been investigated extensively. In addition, with a small separation, the effect of mutual coupling between the antennas becomes important. Refs [4]-[8] investigated the impact of this effect on antenna correlation and MIMO capacity.

Total active reflection coefficient (TARC) must also be considered. We use TARC rather than the traditional scattering matrix because the scattering matrix does not accurately characterize the radiation efficiency and bandwidth of an antenna array [9].

This paper, based on spatial diversity, investigates a new low profile four channel MIMO antenna with good isolation and simple fabrication. The antenna element has a meander

shape and its dimensions are obtained through the Invasive Weed Optimization, IWO algorithm, [10, 11].

The outline of this paper is as follows. First, is the overview of IWO algorithm, next using this algorithm to optimize the geometry of a meander-shaped patch antenna. After this, four configurations of two element meander-shaped patch MIMO antennas are proposed and the IWO algorithm is applied to each antenna design. In order to study the performance of the MIMO antennas, mutual coupling and total active reflection coefficient are considered. The results of the optimal antenna are presented and discussed. Based on the results, the best type is selected and used to construct a MIMO antenna with four elements.

This four channel MIMO antenna is optimized using the IWO algorithm to achieve acceptable values for the reflection coefficient and isolation. The proposed optimized antenna was fabricated. Measurement results have been compared with simulated results, thus confirming the proposed design methodology.

II. INVASIVE WEED OPTIMIZATION (IWO) ALGORITHM

Invasive Weed Optimization (IWO) is one of the novel numerical stochastic optimization algorithms inspired from colonizing weeds that was first deigned and developed in [10].

Weeds are plants whose vigorous, invasive habits of growth pose serious threats to desirable plants. There are some interesting characteristics in natural behaviors of weeds which have been used in this optimization algorithm, among of those are fast reproduction and distribution, robustness and adaptation to the changes in the environment.

The algorithm can be summarized in the following four steps [10, 12]:

A. Initializing a population

A finite number of seeds composing the initial population are being dispread randomly over the problem space.

B. Reproduction

Every seed that has grown to a new plant is allowed to produce other seeds depending on its fitness. In the simple case, the number of seeds which are produced by each plant increases linearly from the minimum possible number of seeds, corresponding to minimum fitness, to the maximum possible number of seeds, corresponding to maximum fitness in the population as illustrated in Fig. 1.

C. Spatial dispersal

The produced seeds in the previous step are being distributed randomly in the problem space by normal distribution with a mean equal to zero and a variance parameter decreasing over time. By setting the mean parameter equal to zero, the seeds are distributed randomly such that they locate near to the parent plant. As the variance decreases over time, the fitter plants are grouped together and inappropriate plants are eliminated over time. The standard deviation (SD) that is the root square of the variance of this distribution is calculated in every step as shown in equation (1):

$$\sigma_{iter} = \frac{(iter_{\max} - iter)^n}{iter_{\max}^n}\left(\sigma_{initial} - \sigma_{final}\right) + \sigma_{final}, \quad (1)$$

where σ_{init} and σ_{final} are the initial and final values of SD for the normal distribution respectively. $iter_{max}$ is the maximum number of iterations before stopping the algorithm, σ_{iter} is the SD at the present step and, n is the nonlinear modulation index usually set to 3.

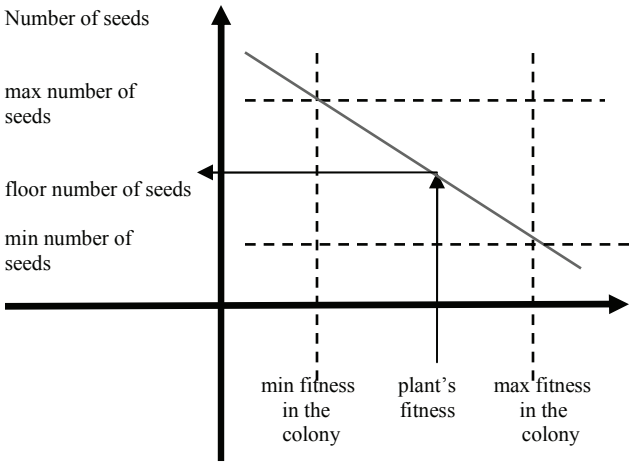

Fig. 1. Seed production procedure in a colony [10] (lower fitness means better situation).

D. Competitive exclusion

After some iteration, the number of plants in a colony will reach its maximum (p_{max}) by fast reproduction. However, it is expected that the fitter plants to have been reported to be more than the undesirable ones. Thus, the final step is to eliminate the inappropriate and weaker plants in a competitive manner for limiting the maximum number of plants in a colony. The process continues until the maximum number of iterations is reached and the plant with the best fitness is selected as the optimal solution.

III. IWO OPTIMIZATION OF THE SINGLE MEANDER-SHAPED PATCH ANTENNA

The structure of the antenna is described in Fig. 2. The antenna is fed by a 50Ω coaxial probe through an SMA connector. The meander-shaped patch antenna is etched on a 3.2-mm-thick Rogers RT/duroid5880 and mounted over a 25 mm × 25 mm metal ground plane. The IWO algorithm is then applied to optimize the meander-shaped antenna in order to have the best impedance matching at resonant frequency of 5.8 GHz.

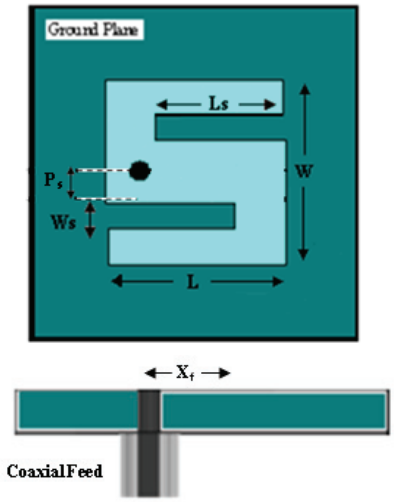

Fig. 2. Configuration of a meander-shaped patch antenna.

At the first step we should choose the parameters which need to be optimized. Through processing these parameters, by modifying and changing them within a reasonable range, we search for the optimal solution. To have these done, minimum and maximum values for each dimension in a 6-dimensional optimization should be determined. This is referred to as L_{ini}. Then a good function must be selected that accurately represents, in a single number, the goodness of the solution. In this problem, the shape of the meander-patch is the solution and as shown in Fig. 2, the geometrical parameters to be optimized include: the patch length L, the patch width W, the slots length Ls, the slots width Ws, the position of feed point X_f, and the position of slots P_s.

As such, the dimension of the solution space is six. For the single meander-shaped patch antenna, the return loss at the desired frequencies is optimized using f = max ($|S_{11}|$, at f = 5.8 GHz).

Table 1 specifies the IWO algorithm setup for minimization of this function. To maintain the meander-shaped structure, the following conditions must also be held as the additional geometrical restrictions:

$L_s < L$ The slots cannot go beyond the patch.
$W_s + P_s < W/2$ The top and bottom stubs must exit.
$X_f < L / 2$ The feed cannot cross the patch.

Table 1: IWO parameters values for the meander-shaped patch antenna.

Symbol	Quantity	Value
NO	number of the initial population	10
I*tmax*	maximum number of iterations	300
Dim	problem dimension	6
P_{max}	maximum number of plant population	15
S_{max}	maximum number of seeds	5
S_{min}	minimum number of seeds	1
n	nonlinear modulation index	3
σ_{initil}	initial value of the standard deviation	3
σ_{final}	final value of the standard deviation	.001

Table 2: Geometrical parameters of the optimized meander-patch antenna (Unit: Millimeters).

Parameter	L	W	Ls	Ws	ps	xf
Value	13.45	14.21	9.55	1.81	2.35	3.33

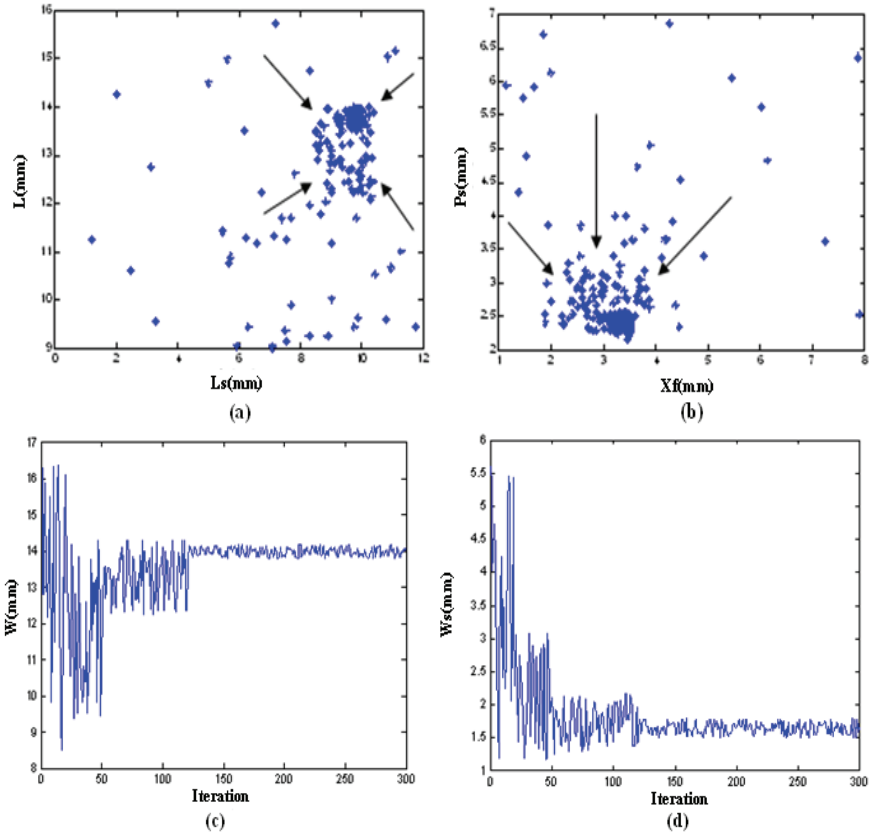

Fig. 3. Convergence results of the meander -shaped patch antenna designs. (a) Conversion of length and length of slots of the patch. (b) Conversion of position of the slots and the feed point(c) Variations of the width of the patch versus iteration number (d) Variations of the width of the slots versus iteration number.

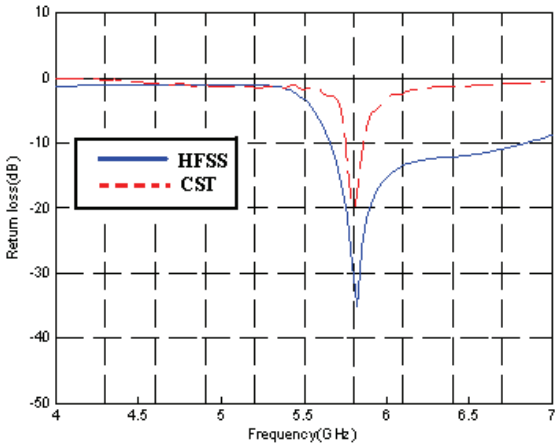

Fig. 4. Simulated S_{11} curves of the optimized meander-shaped antenna.

The optimized results of the single meander shape antenna are presented in Table 2. Figure 3 illustrate the convergence results of the optimization. Figure 4 shows the simulated return loss (S_{11}) curve, using CST and HFSS software's. As can be seen from this figure, the antenna resonates at 5.8 GHz, so the goal of optimization has been satisfied. Radiation pattern of the optimized meander-shaped patch antenna is plotted in Fig. 5.

The total time of the design process is about 12 hours on a Pentium IV (2.8 GHz) machine.

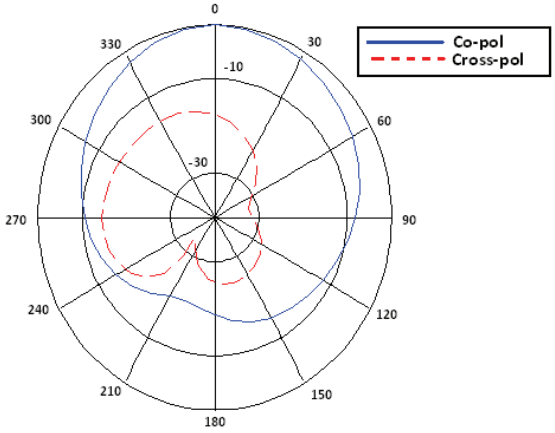

Fig. 5. Radiation pattern of the optimized meander-shaped patch antenna.

IV. TWO-ELEMENT MEANDER-SHAPED PATCH ANTENNA

Since the meander-shaped patch antenna is not influenced by another nearby meander antenna, it is an ideal candidate for use in compact array designs. In this research, four different antenna array configurations, as shown in Fig. 6, each using two antenna elements of Fig. 1 are proposed. The meander antenna array elements are separated by 7mm (0.13 λ).

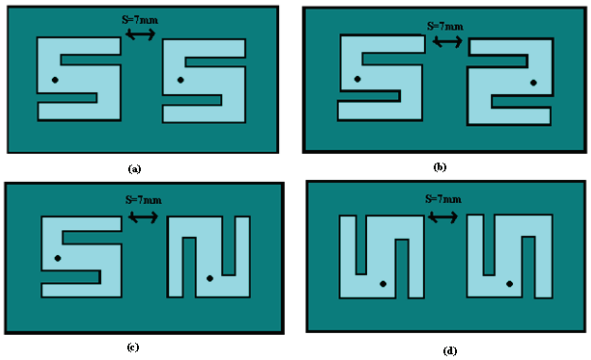

Fig. 6. Four different configurations of dual antenna arrays. Type: (a) 1, (b) 2, (c) 3, (d) 4.

Now the IWO algorithm is used to optimize the geometry of the antenna in order to improve the isolation between antenna ports, the fitness function for this optimization should contain mutual coupling between array elements.

The mutual coupling between the antennas is obtained from S_{ij} of the scattering matrix. As the scattering matrix does not accurately characterize the radiation efficiency and bandwidth of a MIMO antenna [13], the array's Total Active Reflection coefficient (TARC) is used to account for both coupling and random signal combination.

TARC is defined as the ratio of the square root of total reflected power divided by the square root of total incident power [14]. The TARC for a lossless N port antenna can be described as:

$$\Gamma_a^t = \sqrt{\sum_{i=1}^{N} |b_i|^2} \Big/ \sqrt{\sum_{i=1}^{N} |a_i|^2} \quad , \qquad (2)$$

where a_i is the incident signal vector with randomly phased elements and b_i is the reflected signal vector. By applying different combinations of excitation signals to each port the array's TARC is calculated. The simulated scattering matrix of the two element arrays is presented in Fig .7. The resonant frequencies of these arrays are at 5.8 GHz with a -10 dB bandwidths of 900 MHz. As can be seen from this figure, the return loss of all the four types are good but the isolation is high only for type 1, therefore antenna types 2,3 and 4 aren't suitable for MIMO application. Figure 8 shows the simulated co-polarization and cross-polarization far-field patterns of a MIMO array.

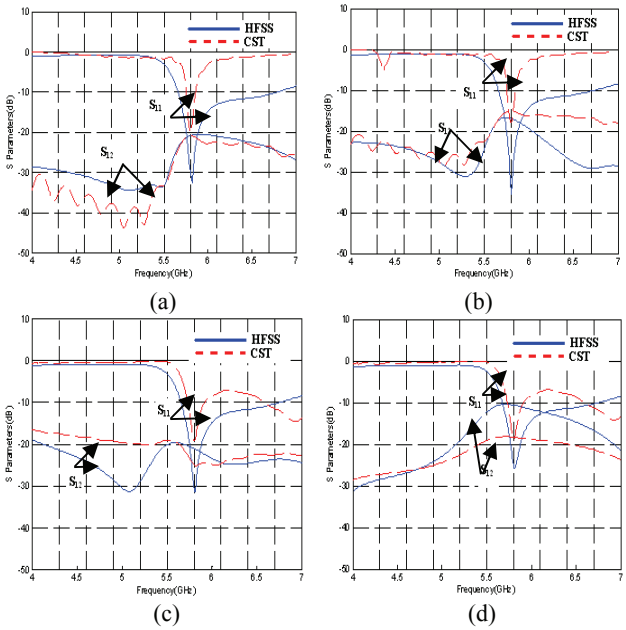

Fig. 7. Simulated scattering parameters for the two-element meander-shaped patch antenna array, Type: (a) 1, (b) 2, (c) 3, (d) 4.

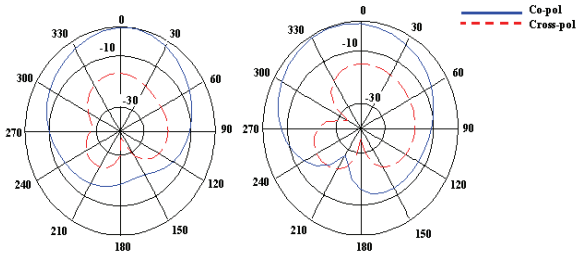

Fig. 8. Radiation patterns of the optimized two-element meander-shaped antenna array. (a) Port1 is excited. (b) Port2 is excited.

V. FOUR-ELEMENT MIMO ANTENNA

In this section a four-element MIMO antenna, using the type (1) 2-element meander-shaped patch antenna array, is discussed (Fig. 9). A prototype antenna (Fig. 10) has been made and

measured. The edge to edge element spacing is 7 mm. Table 3 shows the optimized geometric parameters for this array.

Figure 11 depicts the first row of the scattering matrix of the four element array. As can be seen in this figure coupling between each two elements is below -20dB. Figure 12 shows the simulated

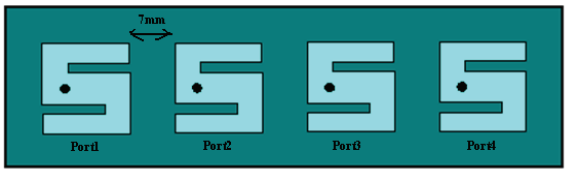

Fig. 9. the proposed four channel MIMO antenna.

Table 3: Geometrical parameters of the optimized four channel MIMO antenna (Unit: Millimeters).

Parameter	L	W	Ls	Ws	ps	xf
value	13.78	13.98	9.81	1.64	2.41	3.39

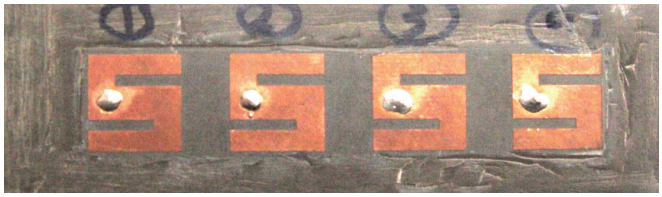

Fig.10. Photograph of the fabricated compact four element MIMO antenna.

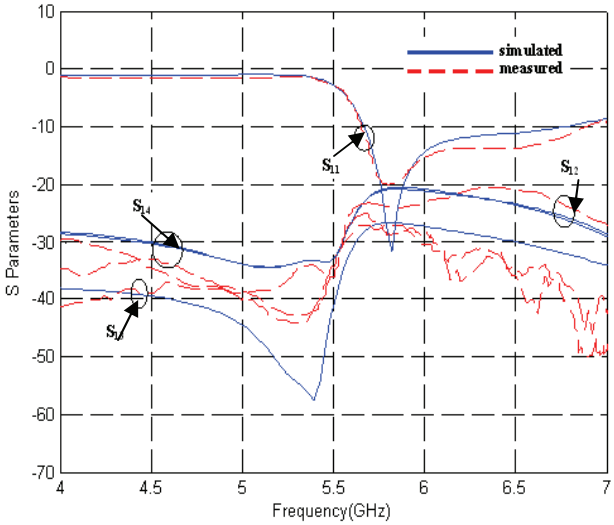

Fig. 11. Simulated and measured scattering parameters for the four-element meander-shaped patch antenna array.

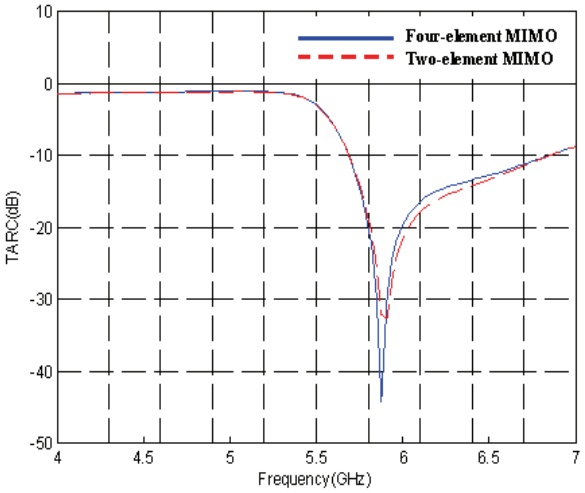

Fig. 12. Simulated TARC of two and four-element meander-shaped patch antenna arrays.

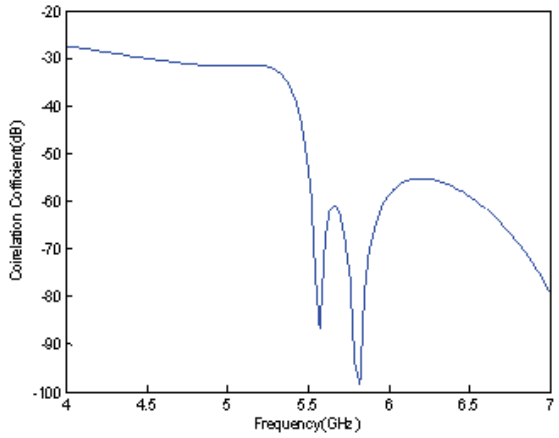

Fig. 13. Simulated correlation coefficient of four-element meander-shaped patch antenna array.

TARC for the two and four element antenna arrays and one can see from this figure that the value of this parameter is lower than -30dB at the 5.8GHz frequency.

As shown in [16] in cases such as a uniform random field case the correlation coefficient can be calculated by S-parameters instead of using 3-dimensional radiation patterns [15].

$$\rho_c = \frac{\left|S_{11}^{*}S_{12} + S_{21}^{*}S_{22}\right|^2}{\left(1-\left|S_{11}\right|^2-\left|S_{21}\right|^2\right)\left(1-\left|S_{22}\right|^2-\left|S_{12}\right|^2\right)}. \quad (3)$$

Simulated correlation coefficient of two ports of the four-element meander-shaped patch antenna array is presented in Fig. 13.

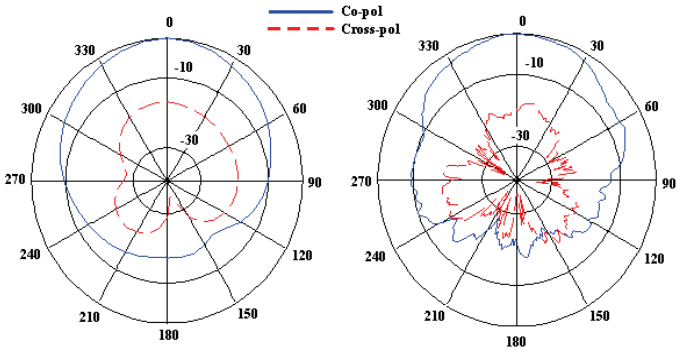

(a) (b)

Fig. 14. (a) Simulated and (b) measured radiation pattern of the optimized four-element Meander-shaped patch antenna array (port1 excited).

The measured and simulated co- and cross-polarization far-field patterns of the optimized MIMO antenna at a resonant frequency of 5.8 GHz in the x-z plane are plotted in Fig. 14. The measured pattern is in good agreement with the simulated pattern.

VI. CONCLUSION

In this paper, Invasive Weed Optimization algorithm is applied to meander-shaped patch antenna designs. The mentioned algorithm was used to optimize meander-shaped patch antennas, considering return loss and bandwidth as design criteria. The procedure and results of this technique show that the weed optimizer is able to achieve the optimum design for a specified antenna performance in an effective manner. Subsequently the algorithm was utilized to design two-element meander-shaped patch antenna arrays. The measured results of the optimized four-port meander-shaped MIMO antenna agree well with the simulation results. The proposed antenna has low profile, good radiation characteristics and sufficiently wide bandwidth to cover 20MHz which is required for the WLAN system. This MIMO antennas show about 20 dB mutual coupling in arrays with 0.13 λ separation.

ACKNOWLEDGMENT

We greatly acknowledge the help and financial support from Iran Telecommunication research centre.

REFERENCES

[1] G. J. Foschini and M. J. Gans, "On limits of wireless communications in a fading environment when using multiple antennas," *Wireless Personal Commun.*, vol. 6, no. 3, pp. 311-335, 1998.

[2] M. A. Jensen and J. W. Wallace, "A review of antennas and propagation for MIMO wireless communications," *IEEE Trans. Antennas Propag.*, vol. 52, no. 11, Nov. 2004.

[3] D. S. Shiu, G. J. Foschini, and M. J. Kahn, "Fading correlation and its effect on the capacity of multi element antenna systems," *IEEE Trans. Commun.*, vol. 48, pp. 502–513, Mar. 2000.

[4] B. Clerckx, D. Vanhoenacker-Janvier, C. Oestges, and L.Vanderdorpe, "Mutual coupling effects on the channel capacity and the space-time processing of MIMO communication systems," *Proc. IEEE ICC.,* vol. 4, pp. 2638-2642, pp. 11-15, May 2003.

[5] J. W. Wallace and M. A. Jensen, "Mutual coupling in MIMO wireless systems: A Rigorous Network Theory Analysis," *IEEE Trans. on Wireless Commun.*, vol. 3, no. 4, pp. 1317-1325, Jul. 2004.

[6] V. Jungnickel, V. Pohl, and C. von Helmolt, "Capacity of MIMO systems with closely spaced antennas," *IEEE Commun. Lett.*, vol. 7, no. 8, pp. 361-363, Aug. 2003.

[7] B. Lindmark, "Capacity of a 2 x 2 MIMO antenna system with mutual coupling losses," *Proc. IEEE Antennas and Propagation Society International Symposium*, vol. 2, pp. 1720-1723, pp. 20-25, Jun. 2004.

[8] C. Waldschmidt, S. Schulteis, and W. Wiesbeck, "Complete RF system model for analysis of compact MIMO arrays," *IEEE*

Trans Vehic. Technol., vol. 53, no. 3, pp. 579-586, May 2004.

[9] S. H. Chae, S.-K. Oh, and S.-O. Park, "Analysis of mutual coupling, correlations, and TARC in WiBro MIMO array antenna," *IEEE Antennas and Wireless Propagation Letters*, vol. 6, pp. 122-125, 2007.

[10] A. R. Mehrabian and C. Lucas, "A novel numerical optimization algorithm inspired from weed colonization," Ecological Informatics, vol. 1, pp. 355-366, 2006.

[11] A. R. Mallahzadeh, S. Es'haghi, and A. Alipour, "Design of an E-shaped MIMO antenna using IWO algorithm for wireless application at 5.8 GHz," Progress In Electromagnetics Research., vol. 90, pp. 187-203, 2009.

[12] A. R. Mallahzadeh, H. Oraizi, and Z. Davoodi-Rad, "Application of the invasive weed optimization technique for antenna configurations," Progress In Electromagnetics Research, vol. 52, pp. 225-254, 2008.

[13] Y. Rahmat-Samii and E. M. Hielssen, Optimization by Genetic Algorithms, Wiley, 1999.

[14] K. C. Lee and J. Y. Jhang, "Application of particle swarm algorithm to the optimization of unequally spaced antenna arrays," Journal of Electromagnetic Waves and Applications, vol. 20, no. 14, pp. 2001-2012, 2006.

[15] M. A. Jensen and Y. Rahmat-Samii, "FDTD analysis of PIFA diversity antennas on a hand-held transceiver unit," IEEE Antennas Propagation, Symposium Dig., vol. 81, June 1993.

[16] S. Blanch, J. Romeu, and I. Corbella, "Exact representation of antenna system diversity performance from input parameter description," IEE Electronics Letters, vol. 39, pp. 705-707, May 2003.

Batol Bahreini received the B.S. degree in electronics engineering from Shiraz University, Shiraz, Iran, in 2007 and the M.S. degree in electronics engineering from the Iran University of Science and Technology, Tehran, Iran, in 2010. Her research interests are image processing, antennas and MIMO systems.

Alireza Mallahzadeh received the B.S. degree in electrical engineering from Isfahan University of Technology, Isfahan, Iran, in 1999 and the M.S. degree in electrical engineering from Iran University of Science and Technology, Tehran, in 2001, and the Ph.D. degree in electrical engineering from Iran University of Science and Technology, Tehran, in 2006. He is a member of academic staff, Faculty of Engineering, Shahed University, Tehran. He has participated in many projects relative to antenna design, which resulted in fabricating different types of antennas for various companies. Also, he is interested in numerical modeling, and microwaves.

Mohammad Soleimani received the B.S. degree in electrical engineering from University of Shiraz, Shiraz, Iran, in 1978 and the M.S. and Ph.D. degrees from Pierre and Marie Curie University, Paris, France, in 1981 and 1983, respectively. He is working as professor in the Iran University of Sciences and Technology, Tehran, Iran. His research interests are in antennas, small satellites, building RF switches and radar. He has served in many executive and research positions including: Student Deputy of Culture and Higher Education Ministry (Currently known as Ministry of Science, Research and Technology), Head of Iran Research Organization for Science and Technology, Head of Iran University of Science and Technology, Head of Center for Advanced Electronics Research Center (in Iran Electronics Industries); and Technology Director for Space Systems in Iran Telecommunication Industries.

Iterative Solution of Electromagnetic Scattering by Arbitrary Shaped Cylinders

Jamila Selmi[1], Rachida Bedira[1], Ali Gharsallah[1], Abdelhafidh Gharbi [1], Henri Baudrand[2]

[1]Laboratoire de physique de la Matière Molle et Modélisation Electromagnetique,
Faculté des Sciences de Tunis, 2092 ElManar, Tunisia
Selmi_jamila@yahoo.com, Rachida.Bedira@fst.rnu.tn, ali.gharsallah@gmail.com,
Abdel.Gharbi@fst.rnu.tn

[2]Laboratoire LAPLACE, 2 Rue Camichel 31071 Toulouse, France
henri.baudrand@yahoo.fr

Abstract ─ The electromagnetic scattering analysis of geometrically complex structure has played an important role in electromagnetic field theory and practicable applications. The fast and rigorous methods to solve such problem are in great demand. In this work, the Wave Concept Iterative Process (WCIP) combined with a coordinate transformation has been extended to the scattering problems of electromagnetic conducting square cylinder, conducting super-ellipsoid and conducting super-ellipsoid coated with thin dielectric materials. Numerical results illustrate the efficiency of our approach. The radar cross section (RCS) is then reached and compared with the literature.

Index Terms ─ Electromagnetic scattering, radar cross section, coordinate transformation, super-ellipsoid, wave concept iterative process (WCIP).

I. INTRODUCTION

The problems of electromagnetic wave scattering by objects of arbitrary shape placed in free space is very important in many applications, namely, antennas design, remote control and especially in defence applications.

The growing interest in better understanding the electromagnetic scattering of conducting objects and coated conducting objects has been reported in many investigations. As a consequence, many different techniques have been used to resolve these electromagnetic problems, such as the Moment Method (MOM) [1], the Finite Element Method (FEM) [2] and Pattern Equation Method (PEM) [3]. Here another technique is adopted called Wave Concept Iterative Process (WCIP) which takes advantage of the other methods. This method was firstly presented in [4-5], applied to analyse microwave circuits [6-7] and was later successfully applied to a number of diffraction and scattering problems [8-10].The concept of waves has been developed for the evaluation of the electromagnetic scattering by conductor objects and coated conductor cylinders [7-9].

In this paper, the formulation of the scattering problems of arbitrarily shaped cylinders is developed. The first step, called coordinate transformation consists of dividing the scattering surface in the small cells. Theses cells can be placed in a fictitious circular cylinder constituted by different materials. In the second step, to study electromagnetic scattering in the cylindrical coordinate system a WCIP is then applied.

To validate the new iterative formulation, the Radar Cross Section (RCS) for a square perfect electric conductor, metallic super-ellipsoid and a super-ellipsoid coated with dielectric materials are calculated. In the last case, the thickness of the dielectric is supposed very weak, so that iterations are considered identical to those obtained by the consideration of laminated flat coats (layers) [9].

The principle of the WCIP is the expression of boundary and closing conditions in term of waves, (incident $\vec{A}$ and reflected $\vec{B}$), a system of equations relate the incident and reflect waves is deduced from these conditions. This system is resolved by an iterative process. The resolution is

stopped when a good precision reached on the required value [6-8].

II. FORMULATION

A. Coordinate transformation

Let us consider an arbitrary shaped object bonded by surface S, Fig. 1. The structure is meshed into elementary cells, and these cells can be placed on a fictitious circular cylinder. In this case, the Cartesian coordinate system becomes inefficient; which is why the cylindrical coordinate formulation is used. To pass to the cylindrical coordinate a common normal at all cells, Fig. 1, is found. The study of electromagnetic interaction between two cells is equivalent to the modelling of the wave scattering on one or more coaxial fictitious circular cylinders, which have a common axis (O_z). This common centre is constructed geometrically by the intersection between the right bisectors of the two cells [9].

These cylinders are composed of two materials: metallic parts defined on the scattering surface and an isolator part (dielectric parts). In order to calculate the electromagnetic scattering by the metallic parts, it is necessary to define the cylindrical basis function $\{|f_n\rangle\}_{n\in IN}$ and the impedance of the n^{th} mode (Z_n) [11]. These parameters depend on the radium ($r_{1/2}$) of the cylinders and the position of the metallic cells. So, the incident waves $\vec{A}$ on the metallic cells are reflected. The reflected waves $\vec{B}$ are reflected by the free space and generate the next incident waves via a reflection operator $\hat{\Gamma}$ [11].

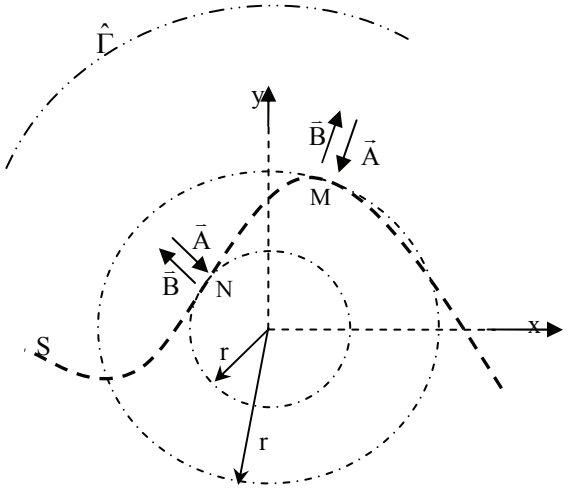

Fig. 1. Meshed surface and coordinate transformation.

B. The wave formulation

The incident $\vec{A}$ and reflected $\vec{B}$ waves are defined by a linear combination of electric field and magnetic one [4-5-8]

$$\vec{A} = \frac{1}{2\sqrt{Z_0}}(\vec{E} + Z_0\vec{J}) \quad (1a)$$

$$\vec{B} = \frac{1}{2\sqrt{Z_0}}(\vec{E} - Z_0\vec{J}), \quad (1b)$$

with, Z_o is an arbitrary impedance. In the following, we shall consider the free space impedance as:

$$Z_o = \sqrt{\frac{\mu_0}{\varepsilon_0}} = 120\pi \quad \Omega. \quad (2)$$

And the current $\vec{J}$, deduced from the tangential magnetic field $\vec{H}$, is used:

$$\vec{J} = \vec{H} \times \vec{n}, \quad (3)$$

where $\vec{n}$ denoted the normal vector to the surface S defined in each cells.

The Wave Concept Iterative Process is based on the expression of boundary condition, in the case of the scattering by an obstacle, the relationship between $\vec{A}$ and $\vec{B}$ is expressed as:

$$\vec{B} = \hat{\Gamma}\vec{A} \quad (4)$$

$$\vec{A} = R\vec{B} \quad , \quad (5)$$

where $\hat{\Gamma}$ designates the scattering operator associated to the geometry of the target [10] and R is a reflected coefficient defined on the surface;

$$\hat{\Gamma} = \sum_n |f_n\rangle \frac{Z_n - Z_o}{Z_n + Z_o} \langle f_n| \quad . \quad (6)$$

$\{|f_n\rangle\}_{n\in IN}$ is a complete modal basis function, expressed as a solution of the Helmholtz equation in the cylindrical coordinates illustrated by the following equation:

$$\frac{1}{\rho}\frac{\partial}{\partial\rho}\left(\rho\frac{\partial f_{nm}}{\partial\rho}\right) + \frac{1}{\rho^2}\frac{\partial^2 f_{nm}}{\partial\theta^2} + \frac{\partial^2 f_{nm}}{\partial z^2} - k^2 f_{nm} = 0. \quad (7)$$

The separation variable method is used and the solution of this equation is given by:

$$\langle \rho, \theta, z | f_{nm} \rangle = \alpha_{nm} B_n(k_\rho \rho) e^{jn\theta} e^{jk_m z}. \quad (8)$$

In this work, the independence on z coordinate is taken, so the expression of the basis function is reduced:

$$\left|f_n\right\rangle = \frac{1}{\sqrt{2\pi r}} e^{jn\theta}. \quad (9)$$

Z_n is the impedance of the n^{th} target mode [11] and Z_0 is the parameter introduced in equation (2).

C. The iterative process

The primary electromagnetic fields $(\vec{E}_0, \vec{H}_0)$ are introduced in the spatial domain, the relation ship between the incident and reflected is expressed by the previous equations (4) and (5). These equations are defined in two different domains. The Fourier Transform (TF) and its inverse (TF^{-1}) insure the links between these domains [12].

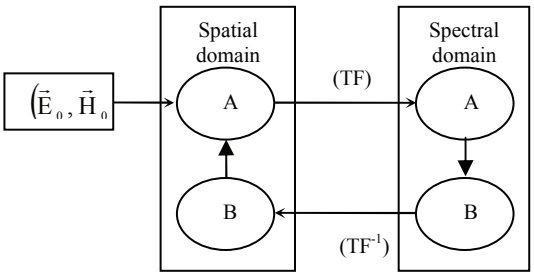

Fig. 2. The iterative scheme.

D. The wave formulation of a dielectric coated layer

By taking into account of the scattering problems of an obstacle coated by a thin dielectric layer, an arbitrary shaped conducting object bonded by surface S_2 coated with a dielectric covering with external surface S_1 , Fig. 3.

The dielectric covering S_1 are homogenous with electrical permittivity ε and magnetic permeability μ. Their expressions are $\varepsilon = \varepsilon_r \varepsilon_0$ and $\mu = \mu_r \mu_0$, where ε_r and μ_r are respectively the relative permittivity and permeability one.

To describe the WCIP and to reach the unknown electric and magnetic fields the interface condition in term of waves at (S_1, S_2) are reviewed and the boundary condition on the environment of the scattering target are written.

Figure 4 shows the multiple transmissions, reflection process for the electromagnetic waves. The theory of the WCIP to analyse electromagnetic

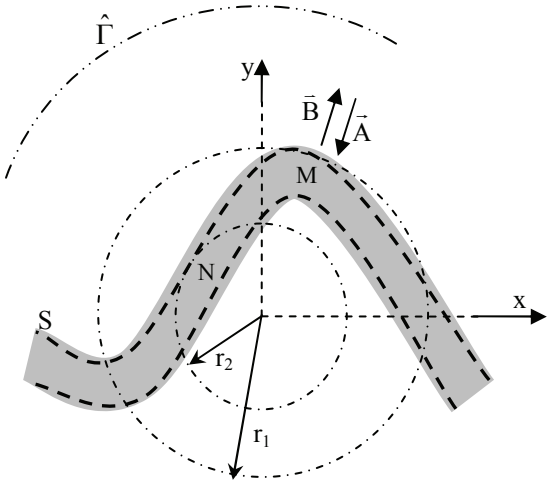

Fig. 3. Dielectric layer coating metallic object.

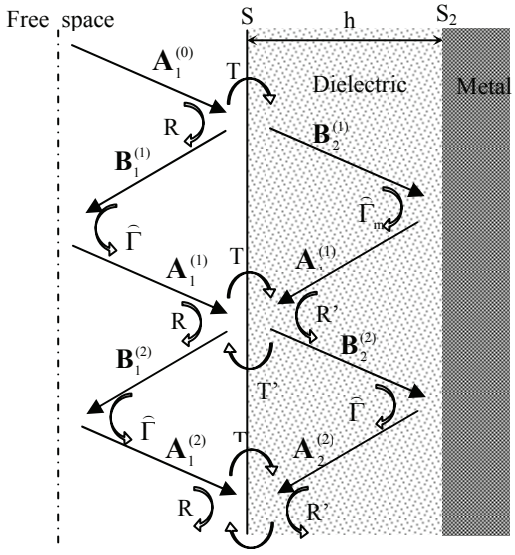

Fig. 4. Dielectric layer coating metallic object.

scattering problems by a treated metallic object is developed previously works [8-9]. Referring to this theory the iterative process explained in different media can be expressed as:

$$\begin{pmatrix} B_1 \\ B_2 \end{pmatrix}^{(P)} = \begin{pmatrix} R & T' \\ T & R' \end{pmatrix} \begin{pmatrix} \hat{\Gamma} & 0 \\ 0 & \Gamma_m \exp(-2jk_2h) \end{pmatrix} \begin{pmatrix} B_1 \\ B_2 \end{pmatrix}^{(P-1)} + \begin{pmatrix} R & R \\ T & T \end{pmatrix} \begin{pmatrix} A_0 \\ B_0 \end{pmatrix} \quad (10)$$

$A^{(p)}$ respectively $B^{(p)}$ are the incident and the reflected waves respectively at the p^{th} iteration (p=1,2,3……) with R and R' (respectively T and T') the reflection (respectively the transmission) coefficient defined as [13-14].

$$R = \frac{Z_2 - Z_1}{Z_2 + Z_1} \quad (11)$$

$$R' = \frac{Z_1 - Z_2}{Z_2 + Z_1} \quad (12)$$

$$T = \frac{2Z_2}{Z_2 + Z_1} \quad (13)$$

$$T' = \frac{2Z_1}{Z_2 + Z_1} \quad , \quad (14)$$

where Z_1 and Z_2 are the intrinsic impedances of the free space and the dielectric layer, Γ_m=-1 is the reflection coefficient on the metallic surface, exp(-$2jk_2h$) is the attenuation term in the dielectric layer which is thickens h and $\hat{\Gamma}$ is the reflection operator expressed on equation (6) and defined by Harrington [11].

III. APPLICATIONS AND RESULTS

A. Metallic square cylinder

In order to test the efficiency of the coordinate transformation and the ability of the wave concept with an arbitrary shape, a perfect conductor cylinder with a square section is analysed. The structure is shown in Fig. 5, using TM wave. The dimensions of the square are a=2λ and the frequency is *f*=1GHz; this geometrical parameters are chosen to be the same as in reference [14].

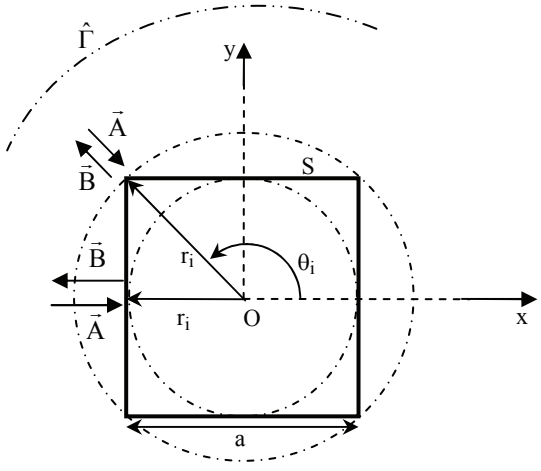

Fig. 5. Conducting square section.

The WCIP leads to the scattering tangential electric field value and the current density at the surface in the side of the out space. The Radar Cross Section is calculated using the far-field transformation, defined by equation (15) [14]:

$$RCS = \lim_{\rho \to \infty} \left(2\pi\rho \frac{|E^s|^2}{|E^i|^2} \right), \quad (15)$$

where ρ is the distance from the target to observation point, E^s and E^i are the scattering and the incident electric fields respectively. To evaluate the scattering operator of the square geometry, the coordinate transformation has been firstly used. Second, the surface current density using the iterative process in the cylindrical coordinates system is then calculated. Finally, the radar cross section, and the numerical results are shown in the following figure.

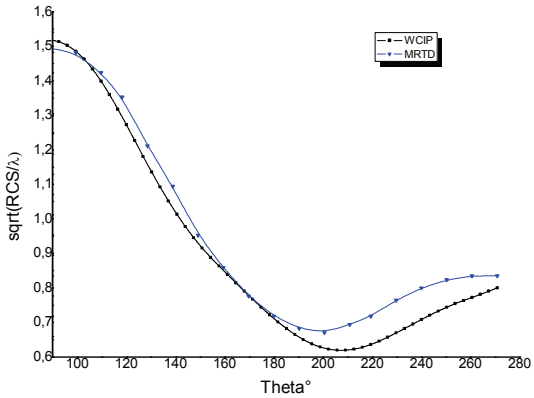

Fig. 6. The normalized RCS of a square geometry.

The results given by WCIP are closely with those found in a Multi Resolution Time Domain MRTD method [14], except in a few points between 210° and 260°. This difference can be explained by the use of some approximation used by the MRTD method and the coordinate transformation applied in the present theory.

A square cylinder is a simple structure to study, using the Waves Concept Iterative Process in case of the electromagnetic scattering some difficulties are founded; The WCIP is based on a definition of the normal at all points of the diffraction surface, and the normal is not defined at corners of the square. That why a regular structure has not any corner called a super-ellipsoid is carried out.

B. Electromagnetic scattering of a super-ellipsoid

In this section, the electromagnetic scattering field by a metallic super-ellipsoid and a super-ellipsoid coated with a dielectric layer are analysed. However, for practical application, general geometrical structures are covered by thin dielectric materials in order to protect the antennas or to find optimum radar cross section.

The super-ellipsoid surface is formed by rotation of a curve $\left(\frac{x}{a}\right)^{2n}+\left(\frac{y}{b}\right)^{2n}=1$, n=8. The structure is illustrated in the following figures. Referring to the theory, when $2n >> 1$, the super-ellipsoid can be approximated by a rectangle [15]. In this case, the previous coordinate transformation and the iterative method are combined and applied to analyse scattering by surface treated targets [9].

The scattering parameter calculated here is the radar cross section illustrated by equation (15) which is obtained by evaluating the scattered fields.

It is be noted that the length of the inner conducting super-ellipsoid and the thickness of the dielectric layer are expressed as a fraction of the wave length for a wave number, $ka = 7.4$, $kb = 12.6$, $h_1 = \frac{a}{100}$, $h_2 = \frac{b}{100}$ and the relative permittivity of the dielectric layer is $\varepsilon_r = 4$.

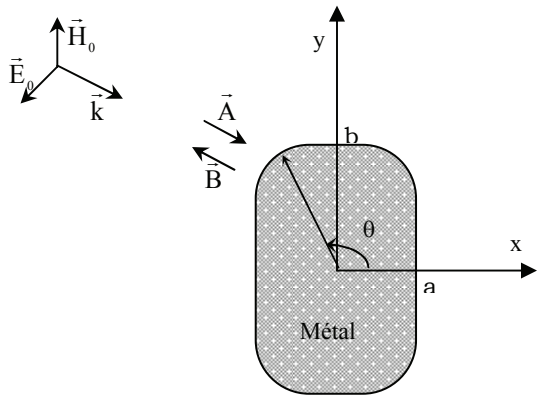

Fig. 7. Metallic super-ellipsoide.

In order to test the efficiency of present combined theory, a process has been implemented in Matlab. The numerical results reach the convergence when the difference between two consecutive iterations is about 10^{-10}. In this case, the convergence of the WCIP is achieved about 25 iterations. The following figure shows the evolution of the surface current density versus the iteration number.

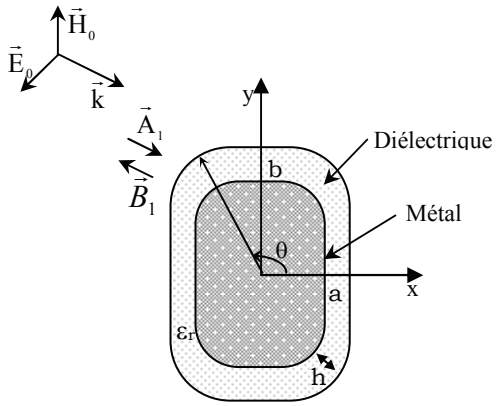

Fig. 8. Super-ellipsoid coated with dielectric material.

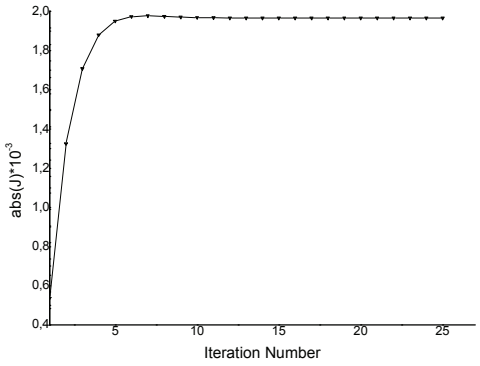

Fig. 9. The normalized current density versus the iteration number.

To illustrate the advantage of covered bodies with dielectric materials, the evolution of Radar Cross Section and the comparison between a metallic super-ellipsoid and the super-ellipsoid covered with dielectric materials are treated, Fig. 10.

It is clear that the effects of dielectric materials is diminution of magnitude of the Radar Cross Section, so diminution of current density distribution generated on the scattering surface which proves the efficiency of dielectric covering conductor bodies.

To illustrate the efficiency of the present iterative formulation, a simulated program is developed, all the calculation up to the Radar Cross

Section. So, the scattering operator of the super-ellipsoid coated with dielectric layer is evaluated. Then, the surface current density and the tangential electric fields are calculated using the iterative process. Finally, the radar cross section is found. The numerical results giving by the WCIP are compared with reference [3], as showing in the following Fig. 11.

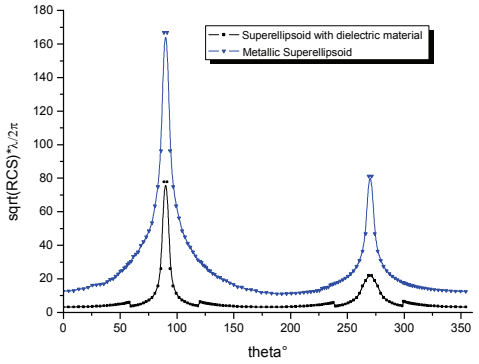

Fig. 10. The RCS of a metallic super-ellipsoid and a super-ellipsoid coated with a dielectric materials.

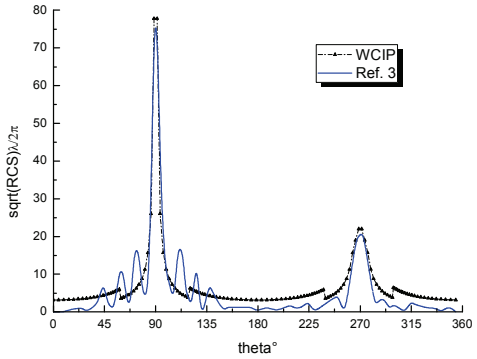

Fig. 11. The RCS of a metallic super-ellipsoid coated with a dielectric materials.

Figure 11 represents the evolution of the radar cross section of a super-ellipsoid coated by a dielectric layer. As expected, the results given by WCIP are in good agreement with those previously published in reference [3], especially at peaks located at 90° and 270° respectively, except that no oscillations have been found in the present work on both sides of these peaks as reported by Pattern Equation Method PEM. To explain this phenomenon, it is assumed that the attenuation term in the dielectric layer as if it was in transmission lines; that is to say the present approach neglect the effect of curvature on the attenuation term. The present study proves that the WCIP takes the advantage of simplicity; it consists of computing a simple recurrent relationship. Furthermore, the iterative method has only small memory requirements. So, all these results have been computed in a personnel computer.

V. CONCLUSION

The WCIP combined with geometry transformation has been extended to the solution of the electromagnetic wave scattering problems by conducting bodies and other conducting bodies coated with thin dielectric layer.

In this research, the coordinate transformation and the presented iterative method are used to calculate the Radar Cross Section of conductor square cylinder, conductor super-ellipsoid and super-ellipsoid coated with a dielectric material. A good agreement in comparison to the MRTD results for the metallic square example and the PEM results for the covered super-ellipsoid are found. The comparison of the scattering characteristics of conductor super-ellipsoid and super-ellipsoid coated with dielectric materials has been done and proved the effect of the dielectric.

The numerical results obtained here show the power of the giving theory. Other works are in progress to extend the iterative method using the geometry transformation to resolve more complicated shapes of electromagnetic waves scattering.

REFERENCES

[1] R. F. Harrington, *Field Computation By Moment Methods*, MacMillan, 1968.

[2] P. P. Silvester and R. L. Ferrari, *Finite Elements For Engineering*, Cambridge University Press, 1990.

[3] A. G. Kyurkchan, D. B. Demin, and N. I. Orlova, "Solution based on the pattern equation method for scattering of electromagnetic waves by objects coated with dielectric materials," *Journal of Quantitative Spectroscopy & Radiative Transfer,* pp. 192-202 , 2007.

[4] R. Bedira, A. Gharsallah, A. Gharbi, and H. Baudrand, "An iterative process based on the concept of waves for electromagnetic scattering problems," *Electromagnetics*, vol. 22, pp. 129-140, 2002.

[5] C. C. H. Tang, "Back-scattering from dielectric coated infinite cylindrical obstacles," Journal of Applied Physics, vol. 28, no. 5, pp. 628–633, 1957.
[6] A. Gharsallah, A. Gharbi, and H. Baudrand, "Efficient analysis of multiport passive circuits using the iterative technique" Electromagnetics, pp. 73-84, 2001.
[7] M. Azizi, H. Aubert, and H. Baudrand, "A new iterative method for scattering problems," Proc of the Euro Microwave Conference, vol. 1, pp. 255-258, 1995.
[8] R. Bedira, A. Gharsallah, L. Desclos, A. Gharbi, and H. Baudrand, "The wave concept iterative process: scattering of a conducting target coated by thin dielectric layer," IEEE Antennas and Propagation Society International Symposium, vol. 2, pp. 98-101, 2002.
[9] A. Mami, R. Bedira, A. Gharsallah, A. Gharbi, and H. Baudrand, "Iterative solution of scattering by surface-treated targets," Int. J RF and Microwave CAE, vol. 13, no. 3, pp. 206-214, 2003.
[10] N. Raveu, O. Pigaglio, G.Prigent and H. Baudrand, "Improvement in the wave concept iterative procedure through spectral connection," IEEE EuMW, October 2007.
[11] R. F. Harrington, Time-Harmonic Electromagnetic Fields, McGraw-Hill, New York, 1961.
[12] M. Yeddes, A. Gharsallah, A. Gharbi, and H. Baudrand, "Characterization of microstrip ring with a narrow gap by an iterative method," International Journal of Microwave Science and Technology, 2008.
[13] S. -G. Pan and I. Wolff. "Scalarization of dyadic spectral Green's function and network formalism for three dimensional full-wave analysis of planar lines and antennas," IEEE Trans MTT, vol. 42, pp. 2118-2127, 1994.
[14] C. A. Balanis, Advanced Engineering Electromagnetics, Wiley 1989.
[15] Q. Cao, Ylnchaochan and P. K. A. Wal, "MRTD electromagnetic scattering analysis," Microwave and Optical Technology Letters, vol. 28, no. 3, pp. 189-195, February 2001.
[16] http://www.mathopenref.com/ellipse.html.

Jamila Selmi was born in Kairouan, Tunisia. She received a master's degree in solid state physics from the Faculty of Sciences of Tunis, Tunisia, in 2004. She is currently working toward the Ph.D. degree in electromagnetics at the Faculty of Sciences of Tunis.

Rachida Bedira was born in Téboulba, Tunisia, in 1975. She received the Ph.D degree in 2006 from the Faculty of Sciences of Tunis, Tunisia. Since 2001, she has been with the Department of Physics at the Faculty of Sciences of Tunis, Tunisia. Dr. Bedira's current research interests include modeling of electromagnetic scattering problems, antennas and microwaves components using liquid crystal material.

Ali Gharsallah is a Professor of electrical engineering. Since 1991 he has been with the Faculty of Sciences of Tunis. His current research interests include antennas, multilayered structures and microwave integrated circuits.

Abdelhafidh Gharbi is a professor with the Faculty of Sciences of Tunis. He is the Director of Research Laboratory of Liquid crystal. His current research interests include microwave components using liquid crystal material.

Henry Baudrand is a Professor at the Ecole Superieure d'Electronique ectrotechnique, Informatique, ENSEEIHT, of Toulouse, France. His current research interests are the modeling of passive and active circuits and antennas. He co-signed over 100 publications in journals and 250 communications in international conferences. He is Fellow Member of IEEE Society, Member of ''Electromagnetism Academy'' and Senior Member of IEE society. He was President of URSI France commission B for 6 years (1993–1999), and President of IEEEMTT-ED French chapter. He is awarded Officier des Palmes académiques, and Director Honoris causa of lasi University.

A Microwave Technique for Detecting Water Deposits in an Air Flow Pipelines

Sharif I. Sheikh[1], Hassan A. Ragheb[1], Khaled Y. Alqurashi[1], and Ibrahim Babelli[2]

[1] Department of Electrical Engineering,
King Fahd University of Petroleum & Minerals (KFUPM), Dhahran-31261, Saudi Arabia
sheikhsi@kfupm.edu.sa

[2] Schlumberger Dhahran Center for Carbonate Research,
KFUPM - King Abdullah Science Park, Dhahran, Saudi Arabia

Abstract **-** A simple microwave method is used to determine thin layers of water inside the air or compressed-air carrying pipes of pneumatic systems. The technique proposed here is based on the shift in the resonant frequency with the changing air-water ratio within the pipe. A calibration chart relating the resonant frequency and thickness of water layer is presented and experimentally verified. Experimental results agreed well with the simulated response, particularly for thin water layers, which are difficult to detect accurately using existing methods.

Index Terms **-** Microwave, reflection, multiphase flow, water deposit.

I. INTRODUCTION

Measuring the liquid to air ratio is important in maintaining presssure and determining the flow rate and liquid buildup within a compressed-air transporting pipe, commonly employed in pneumatic systems. Popular methods of measuring the water level include mechanical, electrical, ultrasonic and optical techniques [1-3]. The most common electrical method excites the two-phase fluid with a low frequency signal and measures the electrical parameters between two electrodes. The measured parameters include capacitance, resistance and inductance, which can determine the dielectric properties (permittivity and conductivity) of the mixture. In the capacitance measurements, the fluids enter into the coaxial capacitor from one end and exit from other end. The dielectric constant (permittivity) of the fluids inside the capacitor is a function of the capacitance, which in turn helps in determining the resonance of an RC circuit [4]. The resistance measurements method mounts two electrodes in the pipe to monitor the conductance of the passing liquids, where the resistivity is a function of the liquid effective length between the electrodes and the electrodes cross sectional area [5].

Ultrasonic sensors, used in the water level determination, also suffer from highly undesirable fluctuation in the measurements due to multiple reflections of sound beams [6, 7]. Electrical two-phase level detectors that use high frequency signals include radio frequency radars and microwave sensors. Different types of RF radars are reported for two-phase level determination, such as multiple-frequency continuous wave (MFCW) radar [8, 9] and frequency step continuous wave (FSCW) radar [10]. But radar applications in level monitoring are subject to strong fluctuations caused by multiple reflections from surroundings. Another common disadvantage of all the methods listed above is their inability to accurately measure small water layer deposits in the pipeline. Measuring the effective dielectric constant of the air-water mixture, on the other hand, can correctly predict the contents of the pipeline.

Microwave signals are often used to distinguish between materials with different dielectric constants. Although the development of microwave sensors began in the 1950s [11], until recently these sensors have had limited application due to their high price and large component size. These sensors are mostly based on the interaction (refraction, scattering, absorption, etc.) between microwave signals and the composite dielectric

media [12]. Thus, for a known structure containing a two phase mixture, simple microwave technique can be adopted to measure the content ratio of the mixture. But in multiphase scenarios, microwave multi-parameter measurements are required. Although free-space microwave transmission sensors employ complicated phase measurements to identify the content ratio of a two-phase mixture, the effects of guiding structure are ignored and averaging of multi-frequency responses is required [13, 14].

In this paper, waveguide modes are excited in the pipeline using a coaxial probe and the related reflection response is measured to calibrate of the air-water ratio, particularly for very thin layer of water deposits in the pipeline. This technique also allowed improved impedance matching compared to that of free space microwave sensors.

II. METHOD OF ANALYSIS

The propagation of electromagnetic waves in a pipeline is governed by the geometrical and electrical properties of the pipe and its contents. For a two-phase pipeline, the gas and liquid mixture constitute a composite dielectric material, where changing the percentage of any component modifies the effective dielectric constant of the mixture and influences its resonant response. This principle is adopted here to determine the water ($\bullet_r$=81) and air ($\bullet_r$=1) level within the pipeline.

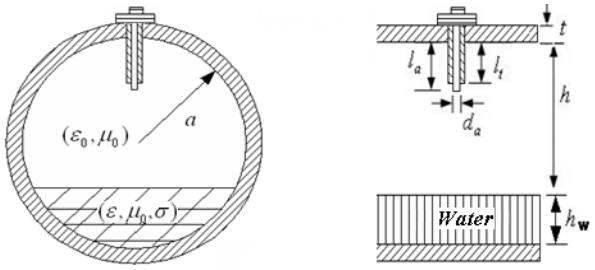

Fig. 1. (a) Cross section and (b) side view of the measurement unit. (a=21.89mm, l_a=14.68 mm, l_t=11.9 mm, d_a=1.3 mm).

The measurement unit used is illustrated in Fig. 1, where the pipe is represented by a circular aluminium waveguide with a diameter of 4.378 cm, length of 43 cm and terminated by matched loads. The length of the pipeline is selected to be long enough to minimize the affects of the reflected waves from the terminations. It is assumed that the micro-machined pipeline unit had no discontinuities (valves/bends) with minimal surface losses. The position and depth of the coaxial probes are selected to optimally monitor the cut-off behaviour of the mixture through measuring the reflection responses. The probe normally excites E-fields of the dominant TE_{11} mode and depending on its diameter and length, the impedance of the waveguide is matched to the desired coaxial prove impedance of 50 Ω. In this work, simulated S-parameter responses are monitored to find the optimal position of the excitation probe. For a homogenously loaded pipeline/waveguide, the cut-off frequency (f_c) and the wave impedance (Z_0) of the TE mode can be expressed as

$$f_c = \frac{S}{\pi D\sqrt{\varepsilon\,\mu}} \qquad (1)$$

and

$$Z_0 = Z_{fs}\frac{\lambda_g}{\lambda_0}\ , \qquad (2)$$

where, ‘D’ is the pipeline diameter, ‘S’ is the Bessel function constant, ‘ε’ and ‘μ’ are permittivity and permeability of the pipeline contents, Z_{fs} is the wave impedance in free space, λ_g and λ_0 are the guide and free-space wave lengths, respectively. The two phase (air-water) mixture within the pipe resembles an in-homogenously loaded waveguide, where cut-off frequency ranges between equivalent modes of the guide resulting from individual loading of the dielectrics [3]. Thus, limiting values of the modal characteristics, such as fc,TE_{11}(water only)=0.45 GHz and fc,TE_{11}(air only)=4.05 GHz, calculated using equation (1) are used to govern the simulation process.

III. RESULTS

A finite element solver is used to simulate the two-phase mixture within the pipe for various combinations of air and water contents. The simulated reflection responses (S11) of the pipe with various water levels are plotted in Fig. 2a. The air-water mixture demonstrated a cut-off response at 4.01 GHz, 3.9875 GHz, 3.977 GHz and 3.9575 GHz for water levels of 1 mm (2.28% of the pipe), 2 mm (4.57%), 3 mm (6.85%) and 4 mm (9.14%), respectively.

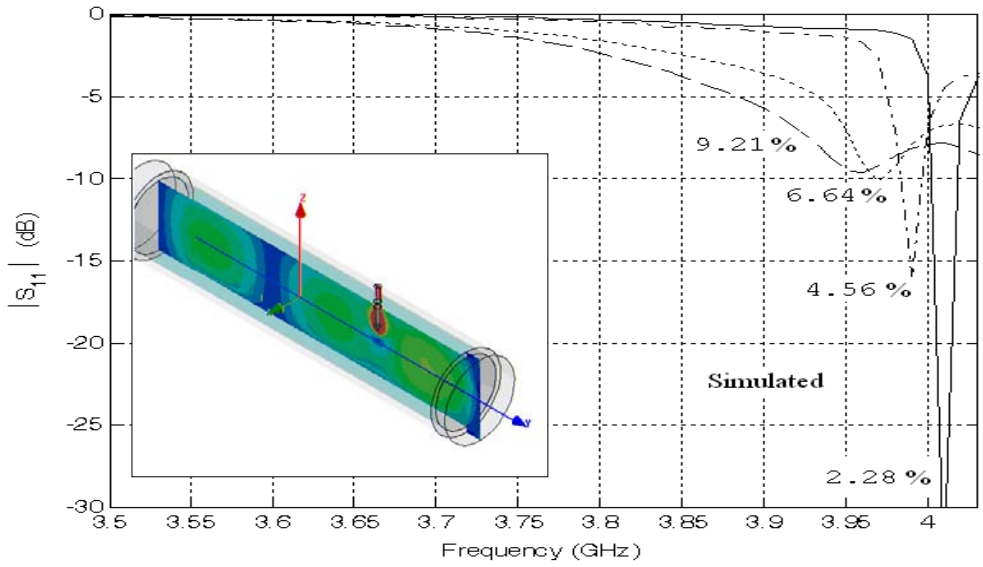

(a)

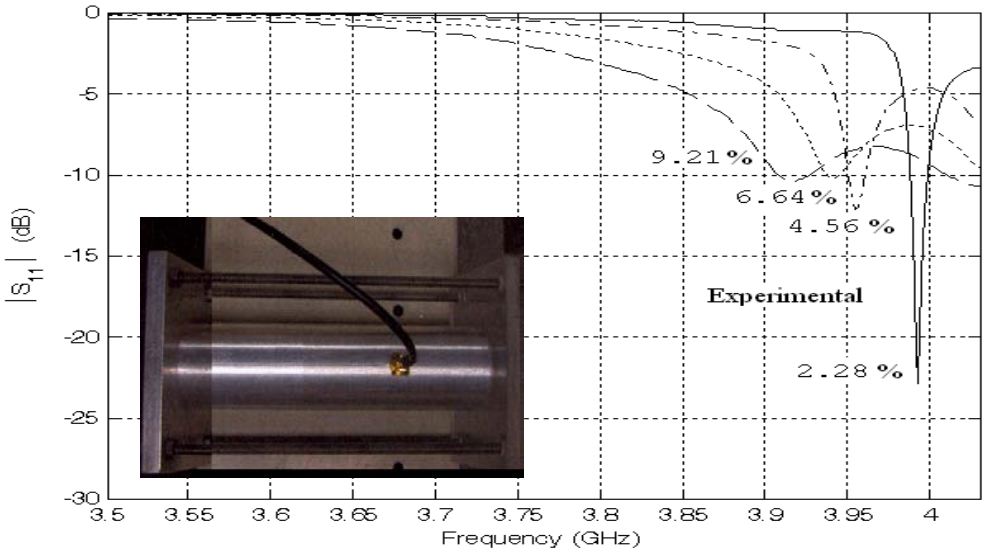

(b)

Fig. 2. Reflection response of the two-phase mixture (depth/diameter) within the pipe, for four different levels of water: (a) simulated response, (b) experimental response. The inset pictures show simulation and experimental process.

The percentage data is calculated here in terms of "depth-diameter" rather than a "filling by volume". Note that increasing water level increased the effective dielectric constant of the two-phase mixture and consequently reduced the cut-off frequency of the pipeline. The conductivity of the pipe metal is observed to affect the cut-off frequency in an inverse manner, although it has little effect on the changes in S11 response with changing water–air ratio.

The measured reflection responses are shown in Fig. 2b. The position, size, inset and alignment of the SMA probe are carefully selected to achieve best excitation. Reflections from side terminations

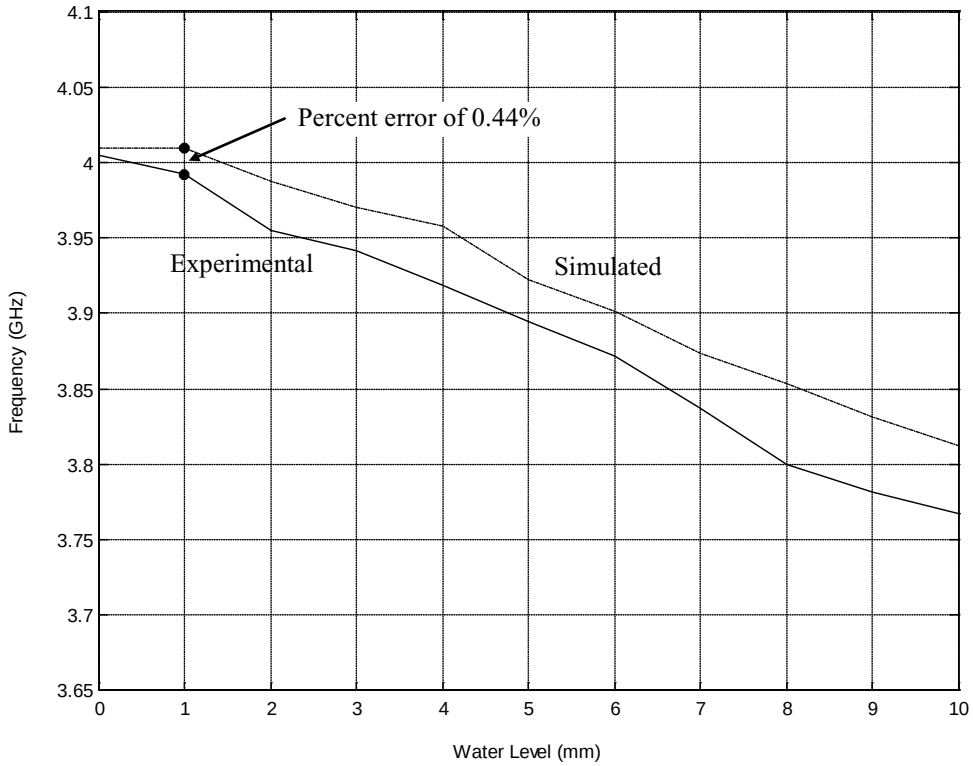

Fig 3. Measured and simulated responses to calibrate water level against the cut-off property of the two-phase mixture within the pipe.

are minimized by selecting absorbing terminators. The experimental results from the network analyzer exhibited similar trends of S11 response with cut-off frequencies of 3.99250 GHz, 3.95500 GHz, 3.94125 GHz and 3.91875 GHz for water levels of 1 mm (2.28%), 2 mm (4.57%), 3 mm (6.85%) and 4 mm (9.14%), respectively. Thus, this technique exhibited an error of 0.44%, 0.82%, 0.90% and 0.99% for water layers of 1 mm, 2 mm, 3 mm and 4 mm, respectively.

Figure 3 superimposes the simulated and experimental cut-off frequency response with respect to the water level in the pipe. Note that for small layers of water the normalized percentage error between the experimental and simulated results are very small (0.44% for 1 mm) with a maximum error of 1.9% occurring for a water layer of 12.9mm or 29.6%. In multiphase flow measurements, an error of 10% is common when one to the parameter is near its low values, i.e., layer of water or flow-rate etc. Therefore, the reproducible measurements results of this simple technique can be attractive for detecting a very thin film of water.

IV. CONCLUSION

A simple microwave technique for water level measurements in a compressed-air transporting pipe is demonstrated. The advantage of this method is its ability to accurately measure very small layers of water, which are often the reason for corrosion in pneumatic systems. The predicted calibration chart relating the water level with the cut-off frequencies of the two-phase pipe is experimentally verified.

ACKNOWLEDGMENT

The authors are grateful for the support of King Fahd University of Petroleum & Minerals (KFUPM) and Schlumberger Dhahran Center for Carbonate Research, Dhahran, Saudi Arabia.

REFERENCES

[1] M. Bérard and I. Babelli, "System and method for measuring flow in a pipeline", WO 2006/072274, July 2006.

[2] H. Yeung and A. Ibrahim, "Multiphase flows sensor response database", *Flow Measurement and Instrumentation,* vol. 14, pp. 219-223, 2003.

[3] H. V. Santen, Z. I. Kolar, and A. M. Scheers, "Photon energy selection for dual energy • and/or x-ray absorption composition measurements in oil–water–gas mixtures", *Nucl. Geophys.,* vol. 9, pp. 193–202, 1995.

[4] D. Marioli, E. Sardini, and A. Taroni, "Measurement of small capacitance variations", *IEEE Trans. Instrum. Meas.,* vol. 40, no. 2, pp. 426-428, April 1991.

[5] E. Dykesteen, A. Hallanger, E. A. Hammer, E. Samnoy, and R. Thorn, "Non-intrusive three-component ration measurement using an impedance sensor", *J. Phys. E: Sci. Instrum.,* vol. 18, pp. 540–54, 1985.

[6] R. Knochel and M.Weiss, "Novel methods of measuring impurity levels in liquid tanks", *Microwave Symposium Digest, IEEE MTT-S International,* vol. 3, no. 8-13, pp. 1651-1654, June 1997.

[7] I. Satoshi, H. Satoshi, O. Masayuki, and T. Shogo, "Measurement of water level in a monitoring system of a bathroom", *SICE Annual Conf.,* pp. 1730-1734, August 2004.

[8] S. A. Sovlukov and V. I. Tereshin, "Measurement of liquefied petroleum gas quantity in a tank by radio-frequency techniques", *IEEE Trans. on Instrumentation and Measurement,* vol. 53, no. 4, pp. 1255-1261, Aug. 2004.

[9] C. Boyer, A. Duquenne, and G. Wild, "Measuring techniques in gas-liquid and gas-liquid-solid reactors", *Chemical Engineering Science,* vol. 57, pp. 3185-3215, 2002.

[10] S. S. Novikov, A. S. Maidanovskii, A. P. Restov, and Yu. M. Andreev, "Microwave level meter with wire line", *KORUS '99,* vol. 2, pp. 661-662, June 1999.

[11] A. R. Von Hippel, *Dielectric Materials and Applications,* MIT Press, 1954.

[12] E. Nyfors, "Industrial microwave sensors – A Review", *Subsurface Sensing Technology and Application,* vol. 1, no. 1, pp. 23-43, 2000.

[13] E. Nyfors and P. V. Vainikainen, *Industrial Microwave Sensors,* Artech House, 1989.

[14] A. Klein, "Microwave determination of moisture in coal: Comparison of attenuation and phase measurement", *Jour. Microwave Power,* vol. 16, no. 3-4, pp. 289-304, 1981.

2010 INSTITUTIONAL MEMBERS

DTIC-OCP LIBRARY
8725 John J. Kingman Rd, Ste 0944
Fort Belvoir, VA 22060-6218

AUSTRALIAN DEFENCE LIBRARY
Northcott Drive
Canberra, A.C.T. 2600 Australia

BEIJING BOOK CO, INC
701 E Linden Avenue
Linden, NJ 07036-2495

BUCKNELL UNIVERSITY
69 Coleman Hall Road
Lewisburg, PA 17837

ROBERT J. BURKHOLDER
OHIO STATE UNIVERSITY
1320 Kinnear Road
Columbus, OH 43212

DARTMOUTH COLLEGE
6025 Baker/Berry Library
Hanover, NH 03755-3560

DSTO EDINBURGH
AU/33851-AP, PO Box 830470
Birmingham, AL 35283

SIMEON J. EARL – BAE SYSTEMS
W432A, Warton Aerodome
Preston, Lancs., UK PR4 1AX

ELLEDIEMME
Libri Dal Mondo
PO Box 69/Poste S. Silvestro
Rome, Italy 00187

ENGINEERING INFORMATION, INC
PO Box 543
Amsterdam, Netherlands 1000 Am

ETSE TELECOMUNICACION
Biblioteca, Campus Lagoas
Vigo, 36200 Spain

OLA FORSLUND
SAAB MICROWAVE SYSTEMS
Nettovagen 6
Jarfalla, Sweden SE-17588

GEORGIA TECH LIBRARY
225 North Avenue, NW
Atlanta, GA 30332-0001

HRL LABS, RESEARCH LIBRARY
3011 Malibu Canyon
Malibu, CA 90265

IEE INSPEC
Michael Faraday House
6 Hills Way
Stevenage, Herts UK SG1 2AY

IND CANTABRIA
PO Box 830470
Birmingham, AL 35283

INSTITUTE FOR SCIENTIFIC INFO.
Publication Processing Dept.
3501 Market St.
Philadelphia, PA 19104-3302

KUWAIT UNIVERSITY
Postfach/po box 432
Basel, Switzerland 4900

LIBRARY – DRDC OTTAWA
3701 Carling Avenue
Ottawa, Ontario, Canada K1A OZ4

LIBRARY of CONGRESS
Reg. Of Copyrights
Attn: 407 Deposits
Washington DC, 20559

LINDA HALL LIBRARY
5109 Cherry Street
Kansas City, MO 64110-2498

RAY MCKENZIE – TELESTRA
13/242 Exhibition Street
Melbourne, Vic, Australia 3000

MISSISSIPPI STATE UNIV LIBRARY
PO Box 9570
Mississippi State, MS 39762

MISSOURI S&T
400 W 14th Street
Rolla, MO 56409

MIT LINCOLN LABORATORY
Periodicals Library
244 Wood Street
Lexington, MA 02420

OSAMA MOHAMMED
FLORIDA INTERNATIONAL UNIV
10555 W Flagler Street
Miami, FL 33174

NAVAL POSTGRADUATE SCHOOL
Attn:J. Rozdal/411 Dyer Rd./ Rm 111
Monterey, CA 93943-5101

NDL KAGAKU
C/0 KWE-ACCESS
PO Box 300613 (JFK A/P)
Jamaica, NY 11430-0613

OVIEDO LIBRARY
PO BOX 830679
Birmingham, AL 35283

PENN STATE UNIVERSITY
126 Paterno Library
University Park, PA 16802-1808

DAVID J. PINION
1122 E PIKE STREET #1217
SEATTLE, WA 98122

KATHERINE SIAKAVARA-
ARISTOTLE UNIV OF
THESSALONIKI
Gymnasiou 8
Thessaloniki, Greece 55236

SWETS INFORMATION SERVICES
160 Ninth Avenue, Suite A
Runnemede, NJ 08078

TIB & UNIV. BIB. HANNOVER
DE/5100/G1/0001
Welfengarten 1B
Hannover, Germany 30167

UNIV OF CENTRAL FLORIDA
4000 Central Florida Boulevard
Orlando, FL 32816-8005

UNIVERSITY OF COLORADO
1720 Pleasant Street, 184 UCB
Boulder, CO 80309-0184

UNIVERSITY OF KANSAS –
WATSON
1425 Jayhawk Blvd 210S
Lawrence, KS 66045-7594

UNIVERSITY OF MISSISSIPPI
JD Williams Library
University, MS 38677-1848

UNIVERSITY LIBRARY/HKUST
CLEAR WATER BAY ROAD
KOWLOON, HONG KONG

UNIV POLIT CARTAGENA
Serv Btca Univ,
Paseo Alfonso XIII, 48
Cartagena, Spain 30203

THOMAS WEILAND
TU DARMSTADT
Schlossgartenstrasse 8
Darmstadt, Hessen, Germany 64289

STEVEN WEISS
US ARMY RESEARCH LAB
2800 Powder Mill Road
Adelphi, MD 20783

YOSHIHIDE YAMADA
NATIONAL DEFENSE ACADEMY
1-10-20 Hashirimizu
Yokosuka, Kanagawa,
Japan 239-8686

ACES COPYRIGHT FORM

This form is intended for original, previously unpublished manuscripts submitted to ACES periodicals and conference publications. The signed form, appropriately completed, MUST ACCOMPANY any paper in order to be published by ACES. PLEASE READ REVERSE SIDE OF THIS FORM FOR FURTHER DETAILS.

TITLE OF PAPER:

AUTHORS(S)

PUBLICATION TITLE/DATE:

RETURN FORM TO:

Dr. Atef Z. Elsherbeni
University of Mississippi
Dept. of Electrical Engineering
Anderson Hall Box 13
University, MS 38677 USA

PART A - COPYRIGHT TRANSFER FORM

(NOTE: Company or other forms may not be substituted for this form. U.S. Government employees whose work is not subject to copyright may so certify by signing Part B below. Authors whose work is subject to Crown Copyright may sign Part C overleaf).

The undersigned, desiring to publish the above paper in a publication of ACES, hereby transfer their copyrights in the above paper to The Applied Computational Electromagnetics Society (ACES). The undersigned hereby represents and warrants that the paper is original and that he/she is the author of the paper or otherwise has the power and authority to make and execute this assignment.

Returned Rights: In return for these rights, ACES hereby grants to the above authors, and the employers for whom the work was performed, royalty-free permission to:

1. Retain all proprietary rights other than copyright, such as patent rights.
2. Reuse all or portions of the above paper in other works.
3. Reproduce, or have reproduced, the above paper for the author's personal use or for internal company use provided that (a) the source and ACES copyright are indicated, (b) the copies are not used in a way that implies ACES endorsement of a product or service of an employer, and (c) the copies per se are not offered for sale.
4. Make limited distribution of all or portions of the above paper prior to publication.
5. In the case of work performed under U.S. Government contract, ACES grants the U.S. Government royalty-free permission to reproduce all or portions of the above paper, and to authorize others to do so, for U.S. Government purposes only.

ACES Obligations: In exercising its rights under copyright, ACES will make all reasonable efforts to act in the interests of the authors and employers as well as in its own interest. In particular, ACES REQUIRES that:

1. The consent of the first-named author be sought as a condition in granting re-publication permission to others.
2. The consent of the undersigned employer be obtained as a condition in granting permission to others to reuse all or portions of the paper for promotion or marketing purposes.

In the event the above paper is not accepted and published by ACES or is withdrawn by the author(s) before acceptance by ACES, this agreement becomes null and void.

AUTHORIZED SIGNATURE — TITLE (IF NOT AUTHOR)

EMPLOYER FOR WHOM WORK WAS PERFORMED — DATE FORM SIGNED

Part B - U.S. GOVERNMENT EMPLOYEE CERTIFICATION

(NOTE: if your work was performed under Government contract but you are not a Government employee, sign transfer form above and see item 5 under Returned Rights).

This certifies that all authors of the above paper are employees of the U.S. Government and performed this work as part of their employment and that the paper is therefor not subject to U.S. copyright protection.

AUTHORIZED SIGNATURE — TITLE (IF NOT AUTHOR)

NAME OF GOVERNMENT ORGANIZATION — DATE FORM SIGNED

PART C - CROWN COPYRIGHT

(NOTE: ACES recognizes and will honor Crown Copyright as it does U.S. Copyright. It is understood that, in asserting Crown Copyright, ACES in no way diminishes its rights as publisher. Sign only if *ALL* authors are subject to Crown Copyright).

This certifies that all authors of the above Paper are subject to Crown Copyright. (Appropriate documentation and instructions regarding form of Crown Copyright notice may be attached).

AUTHORIZED SIGNATURE TITLE OF SIGNEE

NAME OF GOVERNMENT BRANCH DATE FORM SIGNED

Information to Authors

ACES POLICY

ACES distributes its technical publications throughout the world, and it may be necessary to translate and abstract its publications, and articles contained therein, for inclusion in various compendiums and similar publications, etc. When an article is submitted for publication by ACES, acceptance of the article implies that ACES has the rights to do all of the things it normally does with such an article.

In connection with its publishing activities, it is the policy of ACES to own the copyrights in its technical publications, and to the contributions contained therein, in order to protect the interests of ACES, its authors and their employers, and at the same time to facilitate the appropriate re-use of this material by others.

The new United States copyright law requires that the transfer of copyrights in each contribution from the author to ACES be confirmed in writing. It is therefore necessary that you execute either Part A-Copyright Transfer Form or Part B-U.S. Government Employee Certification or Part C-Crown Copyright on this sheet and return it to the Managing Editor (or person who supplied this sheet) as promptly as possible.

CLEARANCE OF PAPERS

ACES must of necessity assume that materials presented at its meetings or submitted to its publications is properly available for general dissemination to the audiences these activities are organized to serve. It is the responsibility of the authors, not ACES, to determine whether disclosure of their material requires the prior consent of other parties and if so, to obtain it. Furthermore, ACES must assume that, if an author uses within his/her article previously published and/or copyrighted material that permission has been obtained for such use and that any required credit lines, copyright notices, etc. are duly noted.

AUTHOR/COMPANY RIGHTS

If you are employed and you prepared your paper as a part of your job, the rights to your paper initially rest with your employer. In that case, when you sign the copyright form, we assume you are authorized to do so by your employer and that your employer has consented to all of the terms and conditions of this form. If not, it should be signed by someone so authorized.

NOTE RE RETURNED RIGHTS: Just as ACES now requires a signed copyright transfer form in order to do "business as usual", it is the intent of this form to return rights to the author and employer so that they too may do "business as usual". If further clarification is required, please contact: The Managing Editor, R. W. Adler, Naval Postgraduate School, Code EC/AB, Monterey, CA, 93943, USA (408)656-2352.

Please note that, although authors are permitted to re-use all or portions of their ACES copyrighted material in other works, this does not include granting third party requests for reprinting, republishing, or other types of re-use.

JOINT AUTHORSHIP

For jointly authored papers, only one signature is required, but we assume all authors have been advised and have consented to the terms of this form.

U.S. GOVERNMENT EMPLOYEES

Authors who are U.S. Government employees are not required to sign the Copyright Transfer Form (Part A), but any co-authors outside the Government are.

Part B of the form is to be used instead of Part A only if all authors are U.S. Government employees and prepared the paper as part of their job.

NOTE RE GOVERNMENT CONTRACT WORK: Authors whose work was performed under a U.S. Government contract but who are not Government employees are required so sign Part A-Copyright Transfer Form. However, item 5 of the form returns reproduction rights to the U. S. Government when required, even though ACES copyright policy is in effect with respect to the reuse of material by the general public.

APPLIED COMPUTATIONAL ELECTROMAGNETICS SOCIETY JOURNAL
http://aces.ee.olemiss.edu

INFORMATION FOR AUTHORS

PUBLICATION CRITERIA

Each paper is required to manifest some relation to applied computational electromagnetics. **Papers may address general issues in applied computational electromagnetics, or they may focus on specific applications, techniques, codes, or computational issues.** While the following list is not exhaustive, each paper will generally relate to at least one of these areas:

1. **Code validation.** This is done using internal checks or experimental, analytical or other computational data. Measured data of potential utility to code validation efforts will also be considered for publication.

2. **Code performance analysis.** This usually involves identification of numerical accuracy or other limitations, solution convergence, numerical and physical modeling error, and parameter tradeoffs. However, it is also permissible to address issues such as ease-of-use, set-up time, run time, special outputs, or other special features.

3. **Computational studies of basic physics.** This involves using a code, algorithm, or computational technique to simulate reality in such a way that better, or new physical insight or understanding, is achieved.

4. **New computational techniques** or new applications for existing computational techniques or codes.

5. **"Tricks of the trade"** in selecting and applying codes and techniques.

6. **New codes, algorithms, code enhancement, and code fixes.** This category is self-explanatory, but includes significant changes to existing codes, such as applicability extensions, algorithm optimization, problem correction, limitation removal, or other performance improvement. **Note: Code (or algorithm) capability descriptions are not acceptable, unless they contain sufficient technical material to justify consideration.**

7. **Code input/output issues.** This normally involves innovations in input (such as input geometry standardization, automatic mesh generation, or computer-aided design) or in output (whether it be tabular, graphical, statistical, Fourier-transformed, or otherwise signal-processed). Material dealing with input/output database management, output interpretation, or other input/output issues will also be considered for publication.

8. **Computer hardware issues.** This is the category for analysis of hardware capabilities and limitations of various types of electromagnetics computational requirements. Vector and parallel computational techniques and implementation are of particular interest.

Applications of interest include, but are not limited to, antennas (and their electromagnetic environments), networks, static fields, radar cross section, inverse scattering, shielding, radiation hazards, biological effects, biomedical applications, electromagnetic pulse (EMP), electromagnetic interference (EMI), electromagnetic compatibility (EMC), power transmission, charge transport, dielectric, magnetic and nonlinear materials, microwave components, MEMS, RFID, and MMIC technologies, remote sensing and geometrical and physical optics, radar and communications systems, sensors, fiber optics, plasmas, particle accelerators, generators and motors, electromagnetic wave propagation, non-destructive evaluation, eddy currents, and inverse scattering.

Techniques of interest include but not limited to frequency-domain and time-domain techniques, integral equation and differential equation techniques, diffraction theories, physical and geometrical optics, method of moments, finite differences and finite element techniques, transmission line method, modal expansions, perturbation methods, and hybrid methods.

Where possible and appropriate, authors are required to provide statements of quantitative accuracy for measured and/or computed data. This issue is discussed in "Accuracy & Publication: Requiring, quantitative accuracy statements to accompany data," by E. K. Miller, *ACES Newsletter,* Vol. 9, No. 3, pp. 23-29, 1994, ISBN 1056-9170.

SUBMITTAL PROCEDURE

All submissions should be uploaded to ACES server through ACES web site (http://aces.ee.olemiss.edu) by using the upload button, journal section. Only pdf files are accepted for submission. The file size should not be larger than 5MB, otherwise permission from the Editor-in-Chief should be obtained first. Automated acknowledgment of the electronic submission, after the upload process is successfully completed, will be sent to the corresponding author only. It is the responsibility of the corresponding author to keep the remaining authors, if applicable, informed. Email submission is not accepted and will not be processed.

PAPER FORMAT (INITIAL SUBMISSION)

The preferred format for initial submission manuscripts is 12 point Times Roman font, single line spacing and single column format, with 1 inch for top, bottom, left, and right margins. Manuscripts should be prepared for standard 8.5x11 inch paper.

EDITORIAL REVIEW

In order to ensure an appropriate level of quality control, papers are peer reviewed. They are reviewed both for

technical correctness and for adherence to the listed guidelines regarding information content and format.

PAPER FORMAT (FINAL SUBMISSION)

Only camera-ready electronic files are accepted for publication. The term **"camera-ready" means that the material is neat, legible, reproducible, and in accordance with the final version format listed below.**

The following requirements are in effect for the final version of an ACES Journal paper:

1. The paper title should not be placed on a separate page. The title, author(s), abstract, and (space permitting) beginning of the paper itself should all be on the first page. The title, author(s), and author affiliations should be centered (center-justified) on the first page. The title should be of font size 16 and bolded, the author names should be of font size 12 and bolded, and the author affiliation should be of font size 12 (regular font, neither italic nor bolded).

2. An abstract is required. The abstract should be a brief summary of the work described in the paper. It should state the computer codes, computational techniques, and applications discussed in the paper (as applicable) and should otherwise be usable by technical abstracting and indexing services. The word "Abstract" has to be placed at the left margin of the paper, and should be bolded and italic. It also should be followed by a hyphen (—) with the main text of the abstract starting on the same line.

3. All section titles have to be centered and all the title letters should be written in caps. The section titles need to be numbered using roman numbering (I. II. ….)

4. Either British English or American English spellings may be used, provided that each word is spelled consistently throughout the paper.

5. Internal consistency of references format should be maintained. As a guideline for authors, we recommend that references be given using numerical numbering in the body of the paper (with numerical listing of all references at the end of the paper). The first letter of the authors' first name should be listed followed by a period, which in turn, followed by the authors' complete last name. Use a coma (,) to separate between the authors' names. Titles of papers or articles should be in quotation marks (" "), followed by the title of journal, which should be in italic font. The journal volume (vol.), issue number (no.), page numbering (pp.), month and year of publication should come after the journal title in the sequence listed here.

6. Internal consistency shall also be maintained for other elements of style, such as equation numbering. As a guideline for authors who have no other preference, we suggest that equation numbers be placed in parentheses at the right column margin.

7. The intent and meaning of all text must be clear. For authors who are not masters of the English language, the ACES Editorial Staff will provide assistance with grammar (subject to clarity of intent and meaning). However, this may delay the scheduled publication date.

8. Unused space should be minimized. Sections and subsections should not normally begin on a new page.

ACES reserves the right to edit any uploaded material, however, this is not generally done. It is the author(s) responsibility to provide acceptable camera-ready pdf files. Incompatible or incomplete pdf files will not be processed for publication, and authors will be requested to re-upload a revised acceptable version.

COPYRIGHTS AND RELEASES

Each primary author must sign a copyright form and obtain a release from his/her organization vesting the copyright with ACES. Copyright forms are available at ACES, web site (http://aces.ee.olemiss.edu). To shorten the review process time, the executed copyright form should be forwarded to the Editor-in-Chief immediately after the completion of the upload (electronic submission) process. Both the author and his/her organization are allowed to use the copyrighted material freely for their own private purposes.

Permission is granted to quote short passages and reproduce figures and tables from and ACES Journal issue provided the source is cited. Copies of ACES Journal articles may be made in accordance with usage permitted by Sections 107 or 108 of the U.S. Copyright Law. This consent does not extend to other kinds of copying, such as for general distribution, for advertising or promotional purposes, for creating new collective works, or for resale. The reproduction of multiple copies and the use of articles or extracts for commercial purposes require the consent of the author and specific permission from ACES. Institutional members are allowed to copy any ACES Journal issue for their internal distribution only.

PUBLICATION CHARGES

All authors are allowed for 8 printed pages per paper without charge. Mandatory page charges of $75 a page apply to all pages in excess of 8 printed pages. Authors are entitled to one, free of charge, copy of the journal issue in which their paper was published. Additional reprints are available for a nominal fee by submitting a request to the managing editor or ACES Secretary.

Authors are subject to fill out a one page over-page charge form and submit it online along with the copyright form before publication of their manuscript.

ACES Journal is abstracted in INSPEC, in Engineering Index, DTIC, Science Citation Index Expanded, the Research Alert, and to Current Contents/Engineering, Computing & Technology.